Modelling pyrite oxidation in refractory gold-bearing stockpiles to evaluate gold recovery by direct cyanide leaching

HANG WANG

Under the supervision of

Professor **Peter A. Dowd**

Associate Professor **Chaoshui Xu**

Thesis submitted for the degree of

Doctor of Philosophy

School of Civil, Environmental and Mining Engineering
The University of Adelaide, Australia

September 2021

THE UNIVERSITY
of ADELAIDE

Table of Contents

Abstract

The recovery of sulphuric refractory gold requires pre-treatment of the material for the liberation of gold particles from sulphide-bearing minerals (mainly pyrite). This pre-treatment is expensive and can increase significantly the total processing cost. However, for low-grade materials stockpiled for a long period of time, this cost can be reduced if the material naturally oxidised. When exposed to air and water, the pyrite in the stockpiles can be oxidised spontaneously. Over a prolonged period of time, this process may result in partial or complete oxidation of the contained pyrites, which may enable gold extraction by direct cyanide leaching and reduce the need for pre-treatment, hence increase the profitability of reclaiming the gold from the stockpiled material. The aim of this research is to investigate the possibility that the natural oxidation of pyrites in stockpiles of refractory gold-bearing materials may facilitate gold recovery without pre-treatment.

To solve this problem, pyrite oxidation under stockpile conditions was studied and two models were developed to predict the level of pyrite oxidation in stockpiles. The first model describes the oxidation rate of pyrite grains under unsaturated conditions and/or circum-neutral to alkaline pH environments, in which a diffusion barrier develops on the fresh pyrite surface during the reaction. This reaction rate model was derived using the shrinking core model and it incorporates the effects of oxygen concentration, temperature and degree of water saturation on the reaction. The second model is a coupled multi-component numerical model that can simulate the pyrite oxidation in three-dimensional stockpiles together with related processes such as oxygen transport and heat transfer. This numerical model includes the reaction rate model as one of its components and the simulation incorporates the above-mentioned factors as well as other stockpile properties such as size distributions of rock fragments and pyrite grains. The outputs from the numerical model include oxygen concentration, temperature distribution, air velocity field, pyrite oxidation level and, more importantly, the oxidation profile of pyrite grains, which is an essential input for the estimation of gold recovery without pre-treatment. The application of these models was demonstrated in this research using a case study of the Kapit Flat stockpile on Lihir Island in Papua New Guinea. The simulation results were compared with those measured for samples taken from the stockpile and an acceptable estimation of the level of pyrite oxidation was obtained after calibrating the model. The models developed in this research have been demonstrated to provide a practical solution framework for estimating the level of pyrite oxidation in refractory gold-bearing stockpiles so that the recovery of gold without pre-treatment can be evaluated.

Publications

[1] Wang, H., Dowd, P.A. and Xu, C. 2021 'Modelling pyrite oxidation in a refractory gold ore stockpile to estimate the gold recovery via direct cyanide leaching – a case study', submitted to *Minerals Engineering*.

[2] Wang, H., Xu, C. and Dowd, P.A. 2021 'Modelling the pyrite oxidation level in a refractory gold-bearing stockpile to assess its potential for gold recovery by direct cyanide leaching', *Minerals Engineering,* vol. 171, 2021/09/01/, p. 107089.

[3] Wang, H, Dowd, PA & Xu, C 2019, 'A reaction rate model for pyrite oxidation considering the influence of water content and temperature', *Minerals Engineering*, vol. 134, 2019/04/01/, pp. 345-355.

List of Figures

List of Tables

This page is blank

Declaration

I certify that this work contains no material which has been accepted for the award of any other degree or diploma in my name, in any university or other tertiary institution and, to the best of my knowledge and belief, contains no material previously published or written by another person, except where due reference has been made in the text. In addition, I certify that no part of this work will, in the future, be used in a submission in my name, for any other degree or diploma in any university or other tertiary institution without the prior approval of the University of Adelaide and where applicable, any partner institution responsible for the joint-award of this degree.

I acknowledge that copyright of published works contained within this thesis resides with the copyright holder(s) of those works. I also give permission for the digital version of my thesis to be made available on the web, via the University's digital research repository, the Library Search and also through web search engines, unless permission has been granted by the University to restrict access for a period of time.

I acknowledge the support I have received for my research through the provision of an Australian Government Research Training Program Scholarship.

This page is blank

Acknowledgements

I gratefully acknowledge Newcrest Mining Limited for the sponsorship of my PhD stipend. I would like to acknowledge Minerals Council Australia for awarding a research scholarship.

Undertaking this PhD has been a challenging and life-changing experience for me and I could not make it this far without the support I received from many people.

I wish to express great gratitude to my supervisors, Professor Peter A. Dowd and Associate Professor Chaoshui Xu, for inspiring me pursuing a PhD degree and providing me with massive support during my study. I am grateful for their guidance and encouragement that have inspired me to self-challenge. It was such a wonderful journey working with them and I have gained a lot from it.

I also want to thank Ms Karyn Gardner, the principal geologist of Newcrest Mining Limited at the time, for providing data and arranging my visit to the mine site. I thank my lovely colleagues; they make my time at the school so enjoyable.

I wish to thank my group members and friends, Dr Zhihe Wang, Miss Yusha Li and Dr Changtai Zhou, not only for inspiring me in technical discussions/research collaborations, but also for their lovely company at my leisure time. I also thank a dear friend, Miss Wanjun Qiu, for her lovely company during these years of study and work in Adelaide.

I wish to thank my parents for their love and support that enable me to pursue what I want.

Finally, a big thank to my fiancé Mr Long Tan, who always backs me up in whatever I do and supports me getting through the challenging and self-growing years of my life.

This page is blank

Chapter 1

Introduction

This section provides a brief description of the research background, a review of the literature related to the research problem, the research objectives and a summary of the research conducted to address the problem.

1.1 Research background

This project was initiated and funded by Newcrest Mining Limited. The company owns 100% the Lihir gold mine located on Aniolam Island, Papua New Guinea. Lihir is a refractory pyrite gold deposit and ore processing requires pre-treatment to oxidise the pyrite in order to release the gold particles encapsulated within the pyrite crystal, after which gold can be extracted by conventional cyanide leaching. The pre-treatment method at Lihir is pressure oxidation, with four parallel autoclaves installed, providing currently an ore processing capacity of 15 Mt per year (Newcrest Mining Limited, 2020). At the Lihir mine, the processing of high-grade and medium-grade ores are prioritised while low-grade ores have been sent to long-term stockpiles for later processing. The stockpiled material is classified as a measured mineral resource with a total tonnage of about 83 Mt at an average grade of 1.9 g/t (Newcrest Mining Limited, 2020). From laboratory tests on samples taken from the stockpiles, it was found that the pyrite had naturally oxidised to varying degrees due to long-term exposure to the atmosphere, and variable gold recoveries can be achieved from the partially oxidised materials via direct cyanide leaching. This has increased interest in understanding more about the level of pyrite oxidation within the stockpiles and investigating the value proposition of recovering gold without pre-treatment enabling the stockpiles to be reclaimed at a lower processing cost. The first step in assessing this potential is to estimate the distribution of the level of pyrite oxidation within the stockpiles, which is the aim of the research reported in this thesis. This estimation requires a detailed understanding of two components of the oxidation process. The first is the rate of pyrite oxidation under the various conditions that may exist within a stockpile, and the second is the quantification and simulation of the influences of physical and chemical processes that affect the pyrite oxidation. The following literature review focuses on these two particular components: the oxidation reaction of pyrite and the numerical modelling of pyrite oxidation in rock piles.

1.2 Pyrite oxidation: surface reaction and kinetics

Pyrite oxidation is of wide interest in many research fields including mineral metallurgy, environmental science and geochemistry. The conditions under which pyrite oxidation is induced or occurs vary significantly from one application to another. For example, in metallurgy, the oxidation of pyrite, as a part of the metal extraction process, is often set up under extreme chemical and physical conditions such as high pressure with high oxidant concentration in order to achieve a high reaction rate. However, in the environmental context, pyrite oxidation can occur spontaneously at a much lower rate under natural conditions, which often causes long-term environmental issues such as acid mine drainage (AMD) that require control and remediation. For these reasons, pyrite oxidation has been studied extensively under different conditions and in different contexts. In this thesis, the review of pyrite oxidation is confined to pyrite oxidation in stockpiles under natural environmental conditions.

1.2.1 Atmospheric oxidation of pyrite

In the natural environment, pyrite oxidation can occur spontaneously when exposed either to atmospheric water and oxygen or to aqueous water and dissolved oxygen (DO). In the long term, atmospheric oxidation of pyrite is a slower process than aqueous oxidation of pyrite. The pyrite surface is often passivated after a fresh pyrite surface is oxidised and an oxidation layer is formed (Chandra and Gerson, 2010).

Eggleston et al. (1996) used scanning tunnelling microscopy (STM) to observe the initial oxidation of a pyrite surface in air and the results show that oxidation proceeds by extending oxidized patches. They proposed a reaction mechanism in which oxidation proceeds via Fe^{2+}/Fe^{3+} cycling. The oxidation is initiated by electron transfer from pyrite-Fe^{2+} to O_2, leading to the formation of ferrous oxide (Fe^{2+}), which is further oxidised to Fe^{3+}. As electron transfer from oxide-Fe^{2+} to O_2 is more energetically favourable than from pyrite-Fe^{2+} to O_2, pyrite-Fe^{2+} is preferentially oxidized by Fe^{3+} in the oxidation product, which causes the extension of the oxidized area to adjacent unreacted areas. In Eggleston et al. (1996), this process was modelled using a Monte Carlo approach based on the assumption that the probability of Fe^{2+} oxidation is positively proportional to the number of nearest-neighbour oxidized sites (Fe^{3+}), which successfully reproduced the surface image observed using scanning tunnelling microscopy (STM). Similar mechanisms were also proposed in Schaufuß et al. (1998) and de Donato et al. (1993).

Studies have shown that sulphate is the major oxidation product formed on the pyrite surface after prolonged exposure to the atmosphere (Buckley and Woods, 1987; Schaufuß et al., 1998; Todd et al., 2003) and the product is largely identified as iron sulphate $Fe_2(SO_4)_3$ (de Donato et al., 1993; Todd et al., 2003). Iron-containing oxidation products also include iron oxy-hydroxide FeOOH, iron hydroxide $Fe(OH)_3$ and ferrous iron oxide FeO as identified in these studies, although opinions differ on which is the most prolific. Based on the evidence given in de Donato et al. (1993), elemental sulphur S^0 and polysulphide may also be present on the oxidized pyrite surface.

Jerz and Rimstidt (2004) studied the rate of pyrite oxidation in moist air (96.7% fixed relative humidity) at 25°C under different oxygen partial pressures. The rate of oxidation was determined by taking the time derivative of the oxygen consumption (in moles) which was found to be approximately linearly proportional to the square root of time. The rate of oxygen consumption ($\frac{dn}{dt}$ in mol.m^{-2}.sec^{-1}) was determined as:

$$\frac{dn}{dt} = 10^{-6.6} P^{0.5} t^{-0.5} \tag{1-1}$$

where p is the partial pressure of oxygen (atm) and t is the reacting time (sec).

This relationship was derived from data measured over a period of about 30 days. The authors compared the experimental results with those of aqueous oxidation and found that the rate of pyrite oxidation in moist air is slightly faster at the beginning of the reaction and then slows

significantly, approaching the aqueous oxidation rates reported by humidity cell studies. Jerz and Rimstidt (2004) attributed the slowing of the oxidation rate to the development of a solution film around the pyrite surface due to hygroscopic oxidation products absorbing water from the surrounding vapour as this solution film slows down oxygen diffusion from the air interface to the pyrite surface and hence limits the oxidation reaction. Based on this mechanism, they derived a theoretical rate formula which is of the same form as the empirical rate formula of Eq. (1-1). However, the coefficient in their theoretical rate formula, given the oxygen solubility and diffusivity in solutions, is about four orders of magnitude larger than that given in Eq. (1-1). Jerz and Rimstidt (2004) attributed this discrepancy in coefficients to the possibility that oxygen diffusion in the thin solution film can be much slower than that in bulk solution. Nevertheless, the empirical rate formula of Eq. (1-1) provides a good fit to the experimental data and captures the rate decreasing trend for pyrite oxidation during the initial 30 days.

The initial rate of pyrite oxidation in air has been measured in previous works. A comparison of the measured rates published in the literature can be found in Jerz and Rimstidt (2004), which showed a range from $10^{-8.7}$ to $10^{-6.5}$ O_2-mol/m^2/s (or $10^{-9.2}$ to $10^{-7.0}$ FeS_2-mol/m^2/s). León et al. (2004) measured the rate of pyrite oxidation in the atmosphere in a desiccator at 20°C and a rate of $10^{-9.3}$ FeS_2-mol/m^2/s at day three was determined using sulphate as the reaction progress variable. The reaction rate after 84 days was measured to be $10^{-10.4}$ FeS_2-mol/m^2/s, twelve times less than the initial reaction rate.

1.2.2 Aqueous oxidation of pyrite

The aqueous oxidation of pyrite can be described by the reaction sequence from Eq.(1-2) to Eq.(1-5) which were proposed by Singer and Stumm (1970) in the context of acid mine drainage. According to Singer and Stumm (1970), Eq.(1-2) is the initiator reaction for pyrite oxidation, where pyrite is oxidized by oxygen and ferrous ion is released. Eq.(1-3) shows that ferrous iron released from the reaction of Eq.(1-2) is oxidized to ferric ion by oxygen and the generated ferric ion can further oxidize pyrite and thus produce more ferrous ion (Eq.(1-4)). Hence, reactions described in Eq. (1-3) and Eq.(1-4) form the propagation process in acid mine drainage. In the reaction of Eq.(1-5), ferric ion hydrolyses and precipitates as ferric hydroxide when the pH is greater than about 3.

$$2\mathrm{Fe}S_2 + 7O_2 + 2H_2O \rightarrow 2Fe^{2+} + 4{SO_4}^{2-} + 4H^+ \quad (1\text{-}2)$$

$$4Fe^{2+} + O_2 + 4H^+ \rightarrow 4Fe^{3+} + 2H_2O \quad (1\text{-}3)$$

$$\mathrm{Fe}S_2 + 14Fe^{3+} + 8H_2O \rightarrow 15Fe^{2+} + 2{SO_4}^{2-} + 16H^+ \quad (1\text{-}4)$$

$$Fe^{3+} + 3H_2O \rightarrow Fe(OH)_3 + 3H^+ \quad (1\text{-}5)$$

This reaction sequence accounts for the observed aqueous oxidation products including ferrous ion, ferric ion and sulphate. However, other oxidation products have also been identified during the oxidation process. Lowson (1982) reported thiosulphate ($S_2O_3^{2-}$),

sulphite (SO_3^{2-}) and elemental sulphur (S^0) in the aqueous oxidation of pyrite. Hiskey and Shlitt (1982) pointed out that, depending on the exact reaction conditions, intermediates such as thiosulphate, sulphite, dithionate and dithionite may also be formed in the overall reaction of pyrite decomposition. On a pyrite surface, Nicholson et al. (1990) identified a ferric oxide layer after oxidation in a carbonate-buffered solution. Mycroft et al. (1990) conducted experiments for electrochemical oxidation of pyrite, where polysulphide and elemental sulphur were detected. Karthe et al. (1993) investigated the pyrite surface after 30 minutes of oxidation in solution over a pH range of 4 to 10 and found that iron hydroxy-oxide was formed on the pyrite surface. Bonnissel-Gissinger et al. (1998) and Todd et al. (2003) also studied pyrite surface oxidation in solution over a wide pH range of 2.5 - 12 and 2-10 respectively. The former found that when pH<4, O-H group, iron-deficient composition and Fe (hydr)oxide presented on the pyrite surface with ferrous ion and sulphate released in solution, while at higher pH, ferrous ion disappeared and the surface was covered by Fe (hydr)oxide. However, Todd et al. (2003) found that ferric (hydroxy) sulphate is the main product on the pyrite surface under acidic and neutral conditions and, when pH>4, Fe oxy-hydroxide starts to occur. Under the most alkaline conditions, goethite and FeOOH were formed which completely covered the pyrite surface.

Bailey and Peters (1976) suggested an overall stoichiometry for pyrite oxidation that includes the formation of both sulphate and elemental sulphur, shown in Eq.(1-6), where the amount of produced ferric iron and sulphate are represented by the undetermined parameters x and y respectively.

$$\mathrm{Fe}S_2 + (0.5 + 1.5y + 0.25x)O_2 + (y - 1 - 0.5x)H_2O \rightarrow (1-x)Fe^{2+} + xFe^{3+} + y{SO_4}^{2-} + (2-y)S + (2y - x - 2)H^+ \quad (1\text{-}6)$$

In their analysis of the reaction mechanism of aqueous pyrite oxidation, Rimstidt and Vaughan (2003) suggested that the formation of the final S-product depends on pH with nearly 100% sulphate formation in low pH environments and substantial amounts of thiosulphate and other S-products in high pH environments. Nevertheless, for simplification, the stoichiometry of Eq. (1-2) for pyrite oxidation with oxygen and water as the primary reactants has often been used in calculations and modelling of the reaction kinetics of pyrite oxidation.

The reaction sequence shown in Eq.(1-2) to Eq.(1-4) also suggests that both oxygen and ferric ion are oxidants in pyrite oxidation. Assuming that ferric ion can only be produced via oxygenation of Fe^{2+} (Eq.(1-3)), which is mostly true in natural systems, pyrite oxidation by Fe^{3+} (Eq.(1-3) and Eq.(1-4)) is stoichiometrically equivalent to pyrite oxidation by O_2 (Eq.(1-2)). In other words, pyrite oxidation always corresponds to the consumption of oxygen, irrespective of whether pyrite is directly oxidised by oxygen or by ferric ion. Considering oxygen as the ultimate oxidant and ferric ion as an intermediate one, the reactions in Eq.(1-2) to Eq.(1-4) represent two reaction pathways for pyrite dissolution. The first is a direct pathway where pyrite is directly oxidised by molecular oxygen as shown in Eq.(1-2) and the other is an indirect pathway where pyrite is indirectly oxidised by oxygen via Fe^{2+}/ Fe^{3+} cycle (Eq.(1-3) and

Eq.(1-4)). For the indirect pathway, the intermediate ferric ion is subject to loss due to hydrolysis (Eq.(1-5)) when the pH is greater than about 3. The hydrolysis of ferric ion corresponds to extra consumption of oxygen in the overall system in addition to pyrite oxidation.

For the prediction of the level of pyrite oxidation, it is important to understand the overall kinetics of pyrite oxidation under natural conditions, which depends on the kinetics of each reaction pathway and their relative roles during the reaction. The roles of oxygen and ferric ion in pyrite oxidation have been discussed in many studies. Singer and Stumm (1970) and Moses et al. (1987) suggested that ferric ion, not oxygen, is the dominant oxidant that oxidises pyrite directly. This was inferred from their findings that the oxidation by ferric ion alone (Eq.(1-4)) is much faster than the oxidation by molecular oxygen (Eq.(1-2)). Moses and Herman (1991) observed dramatic loss of ferrous ion in solution that cannot be explained only by the oxidation of ferrous ion. They attributed this significant loss to the adsorption of ferrous ion on the pyrite surface and noted that the adsorption of ferrous ion is preferred to that of ferric ion. This adsorption of ferrous ion blocks the direct attack of both dissolved oxygen (DO) and ferric ion on the pyrite surface. As a consequence, DO cannot oxidise pyrite directly and the rate of pyrite oxidation is limited by the rate at which the adsorbed ferrous ion can be oxidised by DO. Based on these findings, Moses and Herman (1991) suggested that the oxidation of pyrite is predominantly via the indirect pathway through the Fe^{2+}/Fe^{3+} cycle. This model was extended in Eggleston et al. (1996) as part of the reaction mechanism proposed for atmospheric oxidation of pyrite surfaces.

On the contrary, Williamson and Rimstidt (1994) argued that the oxidation by ferric ion produced from the oxygenation of ferrous iron is not significant at pH = 2. This was based on the observation in Smith (1970) that the oxidation rate with ferrous ion removed (using an externally cycled batch reactor where amberlite cation exchange resins were placed in-line) was the same. In addition, McKibben and Barnes (1986), in their kinetic study of pyrite oxidation with oxygen, show that the oxidation rate does not depend on pH values when it is in the range of 2-4, indicating that the variation of ferric ion concentration in solution, due to solubility change with pH, does not affect the oxidation rate. Williamson et al. (2006) provided a quantitative comparison of iron transformation rates in these reactions in the context of AMD and concluded that the oxidation of pyrite (by either oxygen or ferric iron), rather than the oxidation of ferrous iron, is the rate-determining step in both the initiating stage and the propagation of AMD.

Under abiotic conditions, the rate of ferric ion regeneration is slow, hence the ferric ion concentration in solution is in a range that is insignificant for the surface oxidation of pyrite. In this case, as discussed in Williamson et al. (2006), the pyrite oxidation rate is predominantly determined by the DO concentration. However, under microbial conditions, the rate of ferric ion regeneration from ferrous ion oxygenation can be significantly boosted by bacteria catalysis. Hence, the overall rate of pyrite oxidation is controlled not only by oxygen concentration, but also by the microbial condition. Further discussion on the effect of bacteria can be found in Section 1.3.5.

1.2.3 Kinetics and reaction rate formula for pyrite oxidation with oxygen

Empirical reaction rate formulas for pyrite oxidation with dissolved oxygen have been derived by McKibben and Barnes (1986) and Williamson and Rimstidt (1994). In McKibben and Barnes (1986), the rate formula was derived for the aqueous oxidation of pyrite by dissolved oxygen at 30°C and low pH values of 2–4. Their regression analysis of the initial oxidation rates measured under two oxygen partial pressures (0.21 atm and 1 atm) showed that the reaction rate is of the order of 0.5 with respect to DO concentration. The pH dependency was also examined, and the results show that the oxidation rate is independent of pH over the range of 2 – 4. Eq.(1-7) was obtained based on their analysis in which the unit of the oxidation rate is in moles-pyrite cm^{-2} min^{-1}.

$$R_{sp,O_2} = -10^{-9.77} M_{O2}^{0.5} \tag{1-7}$$

Note: the original equation for the rate of oxidation with DO in McKibben and Barnes (1986) has a coefficient of $10^{-6.77}$, which does not match the reaction rate data or the stated rate unit of moles pyrite $cm^{-2}.min^{-1}$. The rate formula cited here is corrected according to the original rate data published in their paper.

Williamson and Rimstidt (1994) compiled the rate data in Smith (1970), McKibben and Barnes (1986), Nicholson et al. (1988) and Moses and Herman (1991), and derived a rate formula for pyrite oxidation with DO. Their derived rate formula is applicable over the pH range of 2–10 and DO concentration of 10^{-6} – 10^{-1} molar. The rate of pyrite destruction ($mol \cdot m^{-2} \cdot s^{-1}$) is determined as:

$$r = 10^{-8.19(\pm 0.1)} \frac{m_{DO}^{0.5(\pm 00.04)}}{M_{H^+}^{0.11(\pm 0.01)}} \tag{1-8}$$

Similar to the rate formula derived in McKibben and Barnes (1986), the rate of pyrite oxidation with DO was also found to be a half order with respect to DO concentration. But over the pH range of 2–10, the oxidation rate is pH-dependent with negative fractional order with respect to H^+ concentration.

In addition to the empirical rate formulas mentioned above, theoretical rate formulas have also been derived based on the proposed reaction mechanisms for pyrite oxidation in several published studies. Table 1-1 lists some of the theoretical rate formulas proposed for pyrite oxidation with DO. These theoretical rate equations were designed to capture the reaction mechanism rather than to capture the apparent reaction rate, hence the coefficients in these equations were rarely measured. Since the detailed reaction mechanisms of pyrite oxidation are of less concern for the research problem in this work, these studies are not reviewed in detail. Readers interested in this specific research topic are referred to the review papers by Murphy and Strongin (2009) and Chandra and Gerson (2010).

Table 1-1: Theoretical rate equations derived for pyrite oxidation with dissolved oxygen

Reference	Theoretical rate equation	Reaction mechanism/ rate-determining step
Mathews and Robins (1974)	$\frac{dFeS_2}{dt} = KA\frac{K_2[P_{O2}]^{0.5}}{1+K_2[P_{O2}]^{0.5}}$	Adsorption isotherm of oxygen on pyrite surface
Bailey and Peters (1976)	$log\left[\frac{dFeS_2}{dt}\right] = K_1 + \frac{b}{b_c+b_a} log\left[\frac{K_2P_{O2}}{1+K_3P_{O2}}\right]$	Electrochemical control
Holmes and Crundwell (2000)	$r_{FeS_2} = \frac{k_{FeS_2}[H^+]^{-0.18}}{14F}\left(\frac{k_{O_2}[O_2]}{k_{FeS_2}}\right)^{1/2}$	Electrochemical control

1.3 Effects of other factors on the pyrite reaction rate

1.3.1 Effect of temperature

The temperature dependence of the reaction rate can be generally described by the Arrhenius equation:

$$k = Ae^{-\frac{E_a}{RT}} \tag{1-9}$$

where k is the reaction rate constant, E_a is the activation energy of the reaction, R is the gas constant, T is the absolute temperature and A is the pre-exponential factor.

The measured activation energy E_a for pyrite oxidation published in the literature varies significantly. Smith (1970) measured the rate of aqueous pyrite oxidation under temperatures from 25°C to 45°C and an E_a of 64 KJ·mol^{-1} was obtained. In the experiment described in McKibben and Barnes (1986), the activation energy for the temperature range of 20°C to 40°C was determined to be 56.9 KJ·mol^{-1}. Nicholson et al. (1988) determined an activation energy of 88 KJ·mol^{-1} for the temperature range of 3°C to 25°C. At 60°C, however, the magnitude of the reaction rate is less than expected based on this activation energy, suggesting a much smaller activation energy near a temperature of 60°C. Schoonen et al. (2000) measured the activation energy of pyrite oxidation for the pH range of 2 to 6 by increasing the temperature in steps from 23°C to 46.3°C during reactions. They found that the activation energies depend on the pH value and can vary as much as 40 KJ·mol^{-1} with different reaction progress variables. The averaged activation energy over the pH range was found to be from 50 to 64 KJ·mol^{-1}, depending on the reaction progress variable, which is in good agreement with previous studies. In Chiriță and Schlegel (2017), the activation energy for pyrite oxidation was measured for the pH range of 1 to 5 with the temperature range of 25°C to 40°C and the reported E_a varied from 19.1 to 56.8 KJ·mol^{-1}.

Nicholson et al. (1988) suggested that the variation in the measured activation energy at different temperatures is due to a change of the relative controlling mechanism from surface reaction to oxygen diffusion as temperature increases. In their experiments of pyrite

oxidation in carbonate-buffered solution, an oxidised layer was formed on the pyrite surface and oxygen diffusion through the oxidised layer was a part of the reaction process. Both the surface reaction and the diffusion of O_2 through the oxidised layer can be affected by temperature. The apparent activation energy is more of a reflection of the controlling process which gradually changes from the surface reaction to the oxygen diffusion as temperature increases. As discussed in Nicholson et al. (1988), oxygen diffusion has a much smaller activation energy than that of the surface reaction, hence at the high temperature of 60°C, the apparent activation energy decreases. Lasaga (1984) suggested that the diffusion-controlled reaction would have an activation energy close to 20 $kJ \cdot mol^{-1}$.

1.3.2 Effect of water content

The rate of pyrite oxidation can be very different under different water conditions. Smith (1970) conducted a series of experiments to observe the rate of pyrite oxidation in both the liquid phase and the vapour phase at different relative humidity. It was found that the rate of pyrite oxidation in the vapour phase increases with relative humidity and this increase can be accelerated by raising the reaction temperature. A comparison of the overall rates under 100% relative humidity and under liquid conditions (100% water saturation) shows that the rate of pyrite oxidation is slightly faster in the latter condition. The same conclusion can be drawn by comparing the rate of pyrite oxidation in moist air (Jerz and Rimstidt (2004) with that in solution (e.g., Nicholson et al. (1990); Williamson and Rimstidt (1994)). However, rates measured in the initial reaction stage (a few minutes into the reaction) display the opposite trend as can be seen in Jerz and Rimstidt (2004).

León et al. (2004) studied the effect of water saturation on the rate of pyrite oxidation. The results show that the rate increases as water saturation decreases from 95% to 25%. The highest reaction rate is at 25% while the reaction rate is lowest at 0.1% (sample was placed in a desiccator). Field observations of pyritic mine tailings in Elberling et al. (2000) also show that the oxidation rate of pyrite is much faster in well-drained sites than that in wet sites.

Overall, the highest oxidation rate is achieved under partially saturated conditions followed by the reaction rate in the fully saturated condition. The reaction rate in moist air is slightly slower than that in the fully saturated condition and decreases further as air humidity decreases. The reaction rate in the dry state (e.g. in a desiccator) is the lowest.

1.3.3 Effect of impurities

Lehner et al. (2007) studied the effect of impurities on the rate of pyrite oxidation using an electrochemical approach. Natural arsenian pyrite and synthetic pyrite doped with As, Co or Ni and undoped pyrite were investigated in the study. It was found that pyrite with As is more reactive than pyrite with other impurity types while pyrite containing no impurities is least reactive. In addition, the electric current density increases when As concentration increases, indicating that the rate of pyrite oxidation increases with increasing As concentration. Blanchard et al. (2007) conducted a Density Functional Theory (DFT) study on arsenic incorporation into FeS_2 and suggested that the presence of arsenic accelerates pyrite dissolution.

Lehner and Savage (2008) conducted mixed flow and batch experiments to measure the oxidation rate of pyrite synthesized with different impurities at different concentrations. The results show that, statistically, pyrite with impurities has higher reactivity. However, Lehner and Savage (2008) suggested that, in environmental modelling applications, the effect of impurities on pyrite oxidation is probably less significant compared with the effects of other influencing factors.

1.3.4 Effect of specific surface area

Pyrite samples from various sources may have different morphologies and hence the specific surface area may vary significantly even for similar particle size distributions. Consequently, the reaction rate measured for various samples will differ from one to another. For example, Pugh et al. (1984) found that the reaction rate of framboidal pyrite is much faster than that of massive pyrite because the specific surface area of the former is approximately ten times larger than that of the latter. They also found that the relationship between the reaction rate of different samples and their specific surface area ($m^2.g^{-1}$) is approximately linear. Nicholson et al. (1990) studied the relationship between the rate of pyrite oxidation (per mass sample) and particle size, and suggested that, at early reaction times, the reaction rate is linearly proportional to the inverse grain diameter and, at later reaction times, is linearly proportional to the square of the inverse grain diameter.

In many published studies, the reaction rate was reported not as the reaction rate per mass sample, but as the reaction rate per surface area, referred to as the surface reaction rate. This is the rate used in this work when referring the pyrite oxidation rate as applied in the discussions and formulas listed in Section 1.2.1 and Section 1.2.3. For measurement, the surface reaction rate is obtained by dividing the reaction rate measured per mass sample by the specific surface area. Thus, discrepancies are expected among the surface reaction rates derived in different studies where the surface area was obtained using different methods.

In some studies, the surface area was measured using the BET (Brunauer, Emmett and Teller) method, which includes the pore size distribution and is based on the physical adsorption of gas molecules on solid surfaces. In other studies, the specific surface area was calculated from particle size, by multiplying the number of particles per gram of sample by the spherical area of a single particle, as shown in Eq. (1-10) (Nicholson et al., 1988):

$$A_s = \frac{6}{\rho d} \tag{1-10}$$

where A_s is the specific surface area per unit mass of sample, ρ is the mass density and d is the particle diameter. This method assumes that the spherical particles have smooth surfaces whereas the BET method takes the micro-morphology of the surface into consideration. These different approaches yield results that usually differ by a factor of two to four, and in some cases, the BET measured surface area can be up to 20 times larger than the calculated surface area for the same pyrite sample.

Table 2-2 (Wang et al., 2019) lists the specific surface area used in different studies compared with the calculated specific surface area based on the average particle size. When comparing the reaction rates from different studies, the reaction rates should be normalized by the specific surface area obtained using the same method.

Table 1-2: Specific surface area (SSA) obtained in different studies on pyrite oxidation rate (after Wang et al. (2019))

Reference	Grain size (μm)	SSA ($cm^{-2} \cdot g^{-1}$)	
		Calculated	Measured
McKibben and Barnes (1986)	187.5 (125 – 250)	64	251
Moses and Herman (1991)	41.5 (38 – 45)	289	660
Williamson and Rimstidt (1994)	200 (150 -250)	60	470
Kameia and Ohmotob (2000)	125.5 (74-177)	96	538
Jerz and Rimstidt (2004)	335 (250 – 420)	36	100
Gleisner et al. (2006)	156.5 (63 – 250)	77	1470
Nicholson et al. (1990)	108 (90 – 125)	110	--
León et al. (2004)	108 (90 – 125)	110	--
Tabelin et al. (2017)	605 (500-710)	20	240
Qiu et al. (2016)	<74	162	13000

1.3.5 Effect of bacteria

The presence of iron-oxidising and sulphur-oxidising bacteria can accelerate the rate of pyrite dissolution. Smith (1970) showed that rate of pyrite oxidation with bacteria of the *Ferrobacillus-Thiobacillus* group can be more than ten times faster than that without bacteria. Singer and Stumm (1970) found that the oxidation rate of ferrous ion inoculated with untreated natural mine water is 10^6 times larger than that with sterilized natural mine water. Olson (1991) also showed that the rate of pyrite oxidation with dissolved oxygen increased by a factor of 34 in the presence of *A. ferrooxidans* (Gleisner et al., 2006). The catalysis of bacteria on the oxidation of pyrite has been successfully applied on various bioleaching operations.

It is widely accepted that bacteria participate in pyrite oxidation through two mechanisms: a direct mechanism and an indirect mechanism (Evangelou and Zhang, 1995). According to Evangelou and Zhang (1995), the direct mechanism requires physical contact between bacteria and the pyrite surface, where the oxygenations of both surface disulphide and surface ferrous ion are catalysed by bacteria. Consequently, the rate of pyrite dissolution through Eq.(1-2) is boosted. The indirect mechanism of microbial pyrite oxidation does not require bacteria attachment on the pyrite surface. Bacteria in solution are able to catalyse the oxygenation of ferrous ion (Eq.(1-3)), hence increasing the production rate of ferric ion. The increased ferric ion concentration in solution facilitates pyrite dissolution by the reaction in Eq.(1-4) which has a much higher reaction rate than pyrite oxidation by DO.

Smith (1970) suggested that the indirect mechanism predominates in microbial oxidation of pyrite. He measured the O_2 uptake rate (mass per hour) with various pyrite masses and a constant solution volume for both abiotic and microbial pyrite oxidation (with constant cell concentration) and found that, while the chemical oxidation rate increases consistently with increasing pyrite mass, the O_2 uptake rate with bacteria reaches the maximum rate and levels off at a pyrite to water ratio of 15 $g \cdot l^{-1}$. The results indicated that, under microbial conditions, the reaction rate (O_2 uptake rate) is limited by bacteria concentration in solution. Increasing the total available surface area cannot increase the microbial oxidation rate further, which should not be the case if the direct mechanism of bacteria oxidation is dominant. The study in Gleisner et al. (2006) also supported the indirect mechanism of microbial pyrite oxidation. They measured the rate of pyrite oxidation at different DO levels and bacteria concentrations, and found that the reaction rate can be well predicted by the ferric ion concentration alone for the pH of 2 – 3, indicating a dominant reaction mechanism with ferric ion as the direct oxidant. Rodríguez et al. (2003) concluded that pyrite oxidation is initiated by the direct mechanism but subsequently, when the cells release to the solution, the indirect mechanism dominates.

The kinetics of microbial pyrite oxidation have been investigated by Smith (1970), Gleisner et al. (2006), Olson (1991) and Pesic et al. (1989). Smith (1970) found that for the initial 100 hours of microbial pyrite oxidation, during which bacteria concentration increased from 10^4 $cells \cdot ml^{-1}$ (inoculum size) to 10^6 $cells \cdot ml^{-1}$, the reaction rate was the same as that of an identical reaction without bacteria. Between 100 hours and 180 hours, the rate increased gradually as bacteria concentration increased from 10^6 $cells \cdot ml^{-1}$ to about 10^8 $cells \cdot ml^{-1}$. The reaction rate then levelled off after 180 hours while bacteria concentration levelled off at around 200 hours at a maximum concentration of 2×10^8 $cells \cdot ml^{-1}$. The results indicated that a minimum bacteria concentration is required to generate ferric ions at a sufficient rate such that a higher reaction rate than abiotic oxidation can be sustained. In Smith (1970), this minimum bacteria concentration is 10^6 $cells \cdot ml^{-1}$. After this minimum concentration, the reaction rate increases with the bacteria concentration until 10^8 $cells \cdot ml^{-1}$ and then it becomes independent of bacteria concentration. Olson (1991) reached a similar conclusion that the pyrite oxidation rate becomes independent of bacteria concentration if the initial bacteria concentration at inoculation is above 10^6 $cells \cdot ml^{-1}$ (which will then grow to a higher population at the time of rate measurement). The bacteria concentration at which the oxidation rate becomes constant may depend on the pH value due to the corresponding variations in ferric ion solubility.

Gleisner et al. (2006) measured the pyrite oxidation rate at five different DO levels, each with two different bacteria concentrations (nine runs in total with a failed run not counted). The pyrite oxidation rate was found to be positively correlated with bacteria concentration at all DO levels, although the magnitude of the rate increase with bacteria concentration varies with the DO level. The oxidation rate increases with the DO level at all bacteria concentrations (in the investigated range of 0.34 to 27.41 $\times 10^6$ $cells \cdot ml^{-1}$). Multiple linear regression analyses of the logarithm of the rate against DO level and bacteria concentration show that the reaction rate is of the order of 0.26 with respect to DO level and of the order of 0.739 with

respect to bacteria concentration. Compared with abiotic reaction kinetics, which are of the order of 0.5 with respect to oxygen concentration (Jerz and Rimstidt, 2004; McKibben and Barnes, 1986; Williamson and Rimstidt, 1994), microbial mediation decreases the order by about 50% with respect to oxygen concentration. For these reasons, neither the DO level nor bacteria concentration alone can be used to predict the oxidation rate. However, the regression analysis of reaction rate against ferric ion concentration (with R^2 = 0.951) shows that the ferric ion concentration is a good predictor for the reaction rate (Gleisner et al., 2006).

Pesic et al. (1989) investigated the kinetics of ferrous ion oxidation by DO with *T. ferrooxidans* using the electrochemical method. A reaction rate formula was proposed as Eq. (1-11) under atmospheric conditions and for Fe^{2+} < 0.001M, T < 25 ℃ and bacteria concentrations ranging from 6 to 24 mg dry cells per litter solution.

$$\begin{cases} -\dfrac{dFe^{2+}}{dt} = 1.62 \cdot 10^{11} C_{bact}[H^+][Fe^{2+}]P_{O_2} e^{-\left(\frac{58.77}{RT}\right)} & pH > 2.2 \\ -\dfrac{dFe^{2+}}{dt} = 1.62 \cdot 10^{11} C_{bact}[Fe^{2+}]P_{O_2} e^{-\left(\frac{58.77}{RT}\right)} & pH < 2.2 \end{cases} \quad (1\text{-}11)$$

The production rate of ferric ion from ferrous ion oxygenation with bacteria can also be obtained from Eq.(1-11) as each reacted ferrous ion produces a ferric ion. The rate formula for pyrite dissolution by ferric ion in the presence of dissolved oxygen was derived by Williamson and Rimstidt (1994) as:

$$R_{FeS_2} = -10^{-6.07(\pm 0.07)} \frac{[Fe^{3+}]^{0.93(\pm 0.07)}}{[Fe^{2+}]^{0.4(\pm 0.06)}} \quad [mol\ m^{-2} s^{-1}] \quad (1\text{-}12)$$

Despite the similarity in qualitative findings, the rates measured for microbial oxidation in different studies vary significantly, as can be seen in Table 1-3. Unlike abiotic oxidation, the deviation in the microbial oxidation rates cannot be explained by the differences in specific surface areas or pyrite reactivity as discussed in Section 1.3.3 and Section 1.3.4. It may, however, be explained by the mixed effects of pH, time of measurement and lag of bacteria activity. For example, the rate measured in Olson (1991) is about ten times faster than the rate measured in Gleisner et al. (2006) at a comparable oxygen level (DO = 273 μM) and bacteria concentration (26.6 × 10^6 cells·ml^{-1}). The difference may be due to the higher temperature, lower pH and earlier measuring time in Olson (1991). The rate measured in Smith (1970) under the bacteria concentration of 20 × 10^6 cells·ml^{-1} is only slightly lower than the rate measured in Gleisner et al. (2006) with 16.35 × 10^6 cells·ml^{-1} and the difference may be explained by the higher pH and lower temperature in the experiment in Smith (1970). The highest reaction rate was obtained in Smith (1970) when measured at the earliest time (nine days) with the highest bacteria concentration (10^8 cells·ml^{-1}).

Table 1-3: Comparison of measured microbial pyrite oxidation rates from the literature

Reference	Measurement time (days)	DO (μM)	Cells·ml^{-1} × 10^6	Conditions		Rate (mol-FeS_2·m^{-2}·s^{-1})
Gleisner et al. (2006)	31 to 75 days	273	16.35	pH	2.2	9.60E-09
		273	26.605	Temperature	22°C	1.71E-08
		129	3.745	PS (µm)	156.5	7.78E-09
		129	1.63	SSA_c (m^2.g^{-1})	0.0077	4.10E-09
		64.8	4.075	SSA_m (m^2.g^{-1})	0.147	4.26E-09
		64.8	4.095			5.58E-09
		13.2	1.58			3.68E-10
		<=0.006	0.375			3.68E-11
		<=0.006	1.745			3.41E-10
Olson (1991)	4.5	273	25	pH	2	1.43E-07
	3.5			Temperature	28°C	1.27E-07
	4.5			PS (µm)	74.5	2.76E-07
	13			SSA_c (m^2.g^{-1})	0.0153	1.63E-07
	16.5			SSA_m (m^2.g^{-1})	N/A	2.89E-07
	15					2.54E-07
Smith (1970)	19	273	20	pH	3	1.17E-10
	9	273	100	Temperature	20°C	1.28E-07

PSD: particle size

SSA_m: *measured* specific surface area

Note: the reaction rates listed here are corrected from measured specific surface area (SSA_m) to calculated specific surface area (SSA_c). The bacteria concentrations in Gleisner et al. (2006) are averaged values based on the bacteria concentration measured on day 51 and day 64.

1.4 Numerical modelling on pyrite oxidation in rock piles

Pyrite oxidation in rock piles or mine tailings often involves processes such as air transport, heat transfer, microbial activities, water flow and reactive transport. These processes determine the reaction conditions such as oxygen concentration, temperature, microbial condition and water content, which affect the pyrite oxidation rate as discussed in Section 1.3, hence also the effluent discharge. However, the pyrite oxidation in turn also affects these processes therefore it is a coupled system with interdependent components. For example, oxygen transport is affected by reaction consumption, water content and the possible heat-induced air flow, while heat transfer is also influenced by the heat generation from pyrite oxidation; microbial activity in rock piles relies heavily on the temperature and water environment. In order to quantify the influences of these processes on pyrite oxidation and the effluent discharge, numerical models have been developed to simulate these processes for the purpose of prediction of AMD generation. An overview of pyrite oxidation and air transport in sulfidic rock piles can be found in Ritchie (2003).

Studies have shown that for pyrite oxidation in rock piles or mine tailings, oxygen concentration is often the rate-limiting factor among all the influencing factors because of the relatively fast reaction consumption and limited resupply. The oxygen consumption rate depends on the pyrite oxidation rate based on mass conservation. The representation of the pyrite oxidation rate (and oxygen consumption rate) in numerical models is generally based

on either the apparent reaction kinetics or on the shrinking core model (SCM) (Gerke et al., 1998). The former approach often uses a fixed rate or first-order kinetics for the modelling of the pyrite oxidation process in rock piles, and thus ignores the change in the unreacted particle size and the microscale transport of the gaseous or aqueous reactants during the reaction, which may significantly affect the reaction rate. The shrinking core model is more often used in recent modelling work as it adequately describes the oxidative alternation/dissolution processes for gas-solid or liquid-solid reactions. The theory of the shrinking core model is described in Levenspiel (1972), which considers mainly two types of processes during the reaction. One is the diffusion of the gaseous/aqueous reactant from the bulk phase to the reacting surface through the gas/water film and the oxidized layer. The other is the chemical reaction at the particle surface of the solid reactant. Depending on the relative rates of the two processes, the overall apparent reaction rate can be limited purely by the diffusion processes (when the surface reaction is relatively fast), referred to as "diffusion control", or purely by the surface reaction (when the surface reaction rate is relatively slow), referred to as "surface reaction control", or simultaneously by both processes (when their rates are comparable).

Recent advances in numerical models in this area are presented in Lefebvre et al. (2001), Mayer et al. (2002), Pantelis et al. (2002), Molson et al. (2005) and da Silva et al. (2009). These models were derived based on, or evolved from, the previous works including Davis and Ritchie (1986), Pruess (1991), Pantelis (1993), Wunderly et al. (1996), and Gerke et al. (1998).

Davis and Ritchie (1986) developed a mathematical model that couples pyrite oxidation with oxygen bulk diffusion through the void spaces of the rock piles. Pyrite oxidation in rock fragments is modelled using the shrinking core model, where it was assumed that the contained pyrite in the rock particles is immediately reacted in the presence of oxygen and the reaction progress of the rock fragments is controlled by oxygen diffusion through the oxidised layer with pyrite being depleted. The reaction rate varies according to the oxygen concentration solved from the oxygen bulk diffusion. An analytical solution for the one-dimensional problem was derived. Based on their model, Wunderly et al. (1996) developed a one-dimensional numerical model for sulphide oxidation in the vadose zone of mine tailings, named PYROX. In their model, the bulk diffusion coefficient for oxygen varies spatially depending on moisture content, porosity and temperature. They further coupled the PYROX model with the existing MINTRAN reactive transport model developed by Walter et al. (1994), and the resulting model, MINTOX, can simulate sulphide oxidation as well as the geochemical equilibrium. Similarly, Gerke et al. (1998) coupled a two-dimensional sulphide oxidation model with MINTRAN to simulate AMD generation in unsaturated overburden mine spoils, focusing on the effect of system heterogeneity caused by mixing soil materials with different pre-oxidation levels. Molson et al. (2005) then presented POLYMIN, a 2D reactive mass transport and sulphide oxidation model, which was derived from the modified MINTRAN model after Gerke et al. (1998), to simulate acid mine drainage in unsaturated waste rock piles. They used the solution from the HYDRUS model (Simunek et al., 1999) for the water flow and hydraulic properties and investigated the effect of internal structure (layers of

different particle sizes) on the AMD generation and evolution using multiple scenario simulations.

A comparable model to POLYMIN is the MIN3P model presented in Mayer et al. (2002). MIN3P is a general reactive transport model that considers both intro-aqueous reactions and dissolution-precipitation reactions. The dissolution-precipitation module uses either a purely surface reaction control approach or a purely diffusion-control approach. The latter was used for pyrite oxidation in their simulation, which is the same as the shrinking core model used in POLYMIN. The major difference between the two programs for modelling pyrite oxidation is that POLYMIN uses the finite element method with triangular elements while the MIN3P model uses a block-centred finite difference method.

Lefebvre et al. (2001) presented TOUGH AMD to simulate the AMD generation in waste rock piles. The TOUGH AMD model evolved from a general non-isothermal multiphase flow and transport simulator, TOUGH2, developed by Pruess (1991). In TOUGH AMD, the pyrite oxidation rate was given as a volumetric reaction rate as a function of oxygen concentration and surface kinetic constant. The reaction progress was controlled by a geometric factor based on the proportion of remaining pyrite. In addition to the oxygen diffusion considered in the models mentioned above, Lefebvre et al. (2001) also simulated oxygen convection induced by the thermal gradient inside the waste rock pile. Other TOUGH-series simulation codes, TOUGHREACT and TOUGH2-CHEM were also used to simulate pyrite oxidation in variably saturated subsurface flow systems by Xu et al. (2000) where, similarly, the pyrite oxidation rate was based on first order kinetics with geometric factors controlling the reaction progress.

Brown et al. (1999) presented the SULFIDOX model (evolved from FIDHELM by Pantelis (1993)) to simulate sulphide oxidation in waste rock piles considering heat transfer, gas flow and transport of reaction products with water flow. The mathematical formulations are also described in Pantelis et al. (2002), where the pyrite oxidation was represented by the Monod model, the bilinear model or a combination of the two. Oxygen transport by both diffusion and convection were considered in their model and were set as complementary mechanisms depending on the degree of water saturation. When the water saturation is greater than 0.85, air velocity is set to zero and the oxygen transport is only via diffusion. A comparable model to SULFIDOX is the THERMOX model presented in da Silva et al. (2009), where pyrite oxidation, heat transfer, gas transport by diffusion and convection, and geochemical reactions can be simulated. In THERMOX, pyrite oxidation is modelled by the shrinking core model assuming diffusion-control, which is the same as the approach used in Davis and Ritchie (1986) and Molson et al. (2005).

To summarize, the processes involved in the oxidation of pyrite in rock piles include oxygen transport by diffusion and/or convection, heat transfer, pyrite oxidation, fluid flow and intro-aqueous equilibrium. Depending on the focus of the research, these processes are fully or selectively considered in the numerical models discussed above. A comparison of these models is summarized in Table 1-4, where the incorporation of the influencing factors for determining the pyrite oxidation rate are also shown.

Table 1-4: Comparison of different numerical models simulating natural oxidation of pyrite

Models/References	Modelling dimensions	Oxygen transport	Heat transport	Geochemical processes	Pyrite oxidation model	Incorporation of the influencing factors when determine pyrite oxidation rate				
						O2 conc.	T	pH	Water content	Bacteria
Davis and Ritchie (1986)	1D	Diffusion	No	No	SCM	Yes	No	No	No	No
PYROX, *Wunderly et al. (1996)*	1D/2D	Diffusion	No	Yes	SCM	Yes	No	No	No	No
Gerke et al. (1998)	1D/2D	Diffusion	No	Yes	SCM	Yes	No	No	No	No
TOUGH AMD, *Lefebvre et al. (2001)*	2D	Adv + diff	Yes	Yes	Kinetics	Yes	Yes	No	No	No
SULFIDOX, *Brown et al. (1999)*	2D	Adv + diff	Yes	Yes	Monod and/or bilinear model(s)	Yes	Yes	No	No	Yes
MIN3P, *Mayer et al. (2002)*	2D	Diffusion	No	Yes	SCM	Yes	No	No	No	No
POLYMIN, *Molson et al. (2005)*	2D	Diffusion	No	Yes	SCM	Yes	No	No	No	No
THERMOX, *da Silva et al. (2009)*	2D	Adv + diff	Yes	Yes	SCM	Yes	Yes	No	No	No

Note that some of the models in this table can be used for more general applications than just modelling pyrite oxidation. This table is not intended to summarize the general capability of the modelling programs, but to summarize the processes/factors incorporated in the models that are specifically for modelling pyrite oxidation based on the descriptions in these studies.

1.5 Research objectives

The purpose of this research is to formulate a framework for the evaluation of pyrite oxidation in refractory gold-bearing stockpiles so that the outputs can be used to estimate gold recovery from the stockpiles without pre-treatment. The framework developed in this research is applied to a real case study to demonstrate its application. In refractory gold-bearing rocks, gold particles are encapsulated in pyrite crystals and pyrite grains are spatially distributed within rock fragments. The recovery of gold through direct cyanide leaching depends on both the level and the profile of pyrite oxidation in the rock particles. For example, if the edge of a pyrite grain is oxidised but the core is not, the gold particles contained at the edge of the pyrite grain are readily recoverable but those contained in the core are still resistant to direct cyanide leaching. Therefore, to effectively evaluate the gold recovery by direct cyanide leaching, the estimation of both the level and the profile of pyrite oxidation in stockpiles should be incorporated into the evaluation framework.

While the oxidation of pyrite in stockpiles would be subject to the stockpile properties such as the formation and geometry of the stockpile as well as the distribution of pyrite therein, understanding the reaction rate of pyrite oxidation under different conditions in the stockpile is the key to quantifying the oxidation progress, especially when a numerical modelling approach is used. As can be seen in Section 1.2, the surface kinetics of pyrite oxidation are complex and can be affected by many factors including oxygen concentration, temperature, pH value, impurities, microbial activity and degree of water saturation. The prolonged reaction is subject not only to the surface reaction kinetics, but also to the transport of oxygen to the reacting site through a possibly developed diffusion barrier (a solution film and/or an oxidised layer, the development of the diffusion barrier also depends on pH and water content) during the reaction. Although several rate formulas have been developed for pyrite oxidation under different conditions, they do not consider some of the important influencing factors such as the degree of water saturation for prolonged pyrite oxidation. In addition, the rate formula derived in published research for pyrite oxidation are kinetic rate laws, which do not capture the geometric change of pyrite grains during the reaction and are thus not suitable for estimating the oxidation profile of pyrite grains, which is essential for the purpose of this research. Therefore, the first objective of this research is to derive a reaction rate formula for pyrite oxidation that incorporates the important influencing factors related to the stockpile conditions and captures the geometrical variation of pyrite grains during the reaction.

To understand the reaction conditions for pyrite oxidation in stockpiles, it is essential to simulate the dynamic and interdependent processes including pyrite oxidation, oxygen transport, heat transfer and variations of pH values. Spatially variable inputs such as the degree of water saturation, size distributions of pyrite grains and rock particles should also be incorporated in the simulation model. The numerical models discussed in Section 1.4 simulate these processes with an emphasis on the aspect of reactive transport for the purpose of AMD prediction. However, the modelling for pyrite oxidation in these models is, in general, simplified. As can be seen in Table 1-4, although these models are able to simulate the

multiple processes involved, they do not incorporate all of the important influencing factors when determining the rate of pyrite oxidation. They either use surface reaction kinetics or a shrinking core model assuming purely diffusional control to describe the rate of pyrite oxidation, both of which are inadequate to represent the oxidation rate of pyrite grains in rock particles under different conditions. The second objective of this research, therefore, is to derive a numerical modelling framework that can simulate pyrite oxidation in stockpiles, in which related dynamic processes such as oxygen transport and heat transfer are simulated, the reaction progress and oxidation profile of pyrite grains are modelled and important influencing factors for pyrite oxidation are incorporated. Finally, the third objective of this research is to apply the developed numerical method to the evaluation of pyrite oxidation and the recovery of gold by direct cyanide leaching in one of the stockpiles at the Lihir mine. The simulation results from the model are compared with the measured oxidation levels of samples taken from the stockpile for the calibration of the numerical model. Finally, based on the calibrated model, a more accurate estimation of the oxidation levels and the profiles of pyrite grains in different areas of the Lihir refractory gold-bearing stockpile are obtained, together with an evaluation of the potential for gold recovery through direct cyanide leaching.

1.6 Thesis outline

Chapter 2 addresses the first objective. In this chapter, a reaction rate model for pyrite oxidation that incorporates the influences of temperature, oxygen concentration and water saturation is derived based on reaction rate data available in the literature. This model uses the framework of the shrinking core model and considers both the surface reaction kinetics and the diffusion of oxygen through the oxidised layer and/or a thin solution film. The model also defines the shrinking rate of the unreacted core, from which the reaction progress of a pyrite grain can be evaluated. This reaction rate model is applicable for prolonged pyrite oxidation at circum-neutral to alkaline pH under different temperatures and degrees of water saturation.

In Chapter 3, the developed numerical modelling framework for the simulation of pyrite oxidation in stockpiles is presented. The model can simulate oxygen transport by both diffusion and heat-induced air convection, heat transfer and pyrite oxidation. The oxidation of pyrite within rock particles is modelled considering the coupled diffusion-reaction process inside rock particles, which, to the author's knowledge, is the first of its kind for modelling pyrite oxidation in rock particles in environmental modelling applications. Compared with the shrinking core model used for the oxidation of pyritic rock fragments in previously published work mentioned in Section 1.4, the proposed coupled diffusion-reaction process is more general and does not assume the unrealistic immediate complete reaction of pyrite in the presence of oxygen. The reaction of pyrite grains contained within rock particles uses the reaction rate model presented in Chapter 2, together with the rate model for cases without coating developed on fresh pyrite surface. The choice between these two models during simulations depends on the pH value, which is estimated from the current oxidation level and the acid neutralization capacity of the rock at each time step. The developed method is tested on a simplified synthetic stockpile, with simulation results including the oxygen concentration,

temperature, air velocity field, oxidation level as well as the oxidation profile of pyrite grains in different locations of the stockpile. A comparison among different simulation scenarios is also conducted in Chapter 3 to investigate the effects of stockpile properties such as the diffusion coefficient, porosity and geothermal heat on the prolonged pyrite oxidation in the stockpile.

Chapter 4 presents a case study of modelling the pyrite oxidation in a refractory gold-bearing stockpile using the numerical method presented in Chapter 3. The modelled stockpile in this case study is the Kapit Flat stockpile on Lihir island in Papua New Guinea. Characteristics of the stockpile incorporated in the simulation include geothermal heat, the degree of water saturation, rock porosity, rock particle size distribution, pyrite grain size distribution, pyrite reactivity enhanced by arsenic content and the acid neutralisation capacity. The model settings are calibrated using the measured oxidation level of samples taken from the stockpile so that an overall more accurate estimation of the stockpile oxidation level can be obtained. The potential gold recovery by direct cyanide leaching of the Lihir stockpile is also estimated using the simulated oxidation profile of pyrite grains and the results show some general agreement with measured values for the samples tested.

Finally, research outcomes and major findings of this research are summarized in Chapter 5. The limitations of this research are also discussed, which leads to recommendations for potential follow-up work in future research for the problem addressed.

References

Bailey, LK & Peters, E 1976, 'Decomposition of pyrite in acids by pressure leaching and anodization: the case for an electrochemical mechanism', *Canadian Metallurgical Quarterly*, vol. 15, no. 4, 1976/10/01, pp. 333-344.

Blanchard, M, Alfredsson, M, Brodholt, J, Wright, K & Catlow, CRA 2007, 'Arsenic incorporation into FeS2 pyrite and its influence on dissolution: A DFT study', *Geochimica et Cosmochimica Acta*, vol. 71, no. 3, 2/1/, pp. 624-630.

Bonnissel-Gissinger, P, Alnot, M, Ehrhardt, J-J & Behra, P 1998, 'Surface Oxidation of Pyrite as a Function of pH', *Environmental Science & Technology*, vol. 32, no. 19, 1998/10/01, pp. 2839-2845.

Brown, P, Luo, X-L, Mooney, J & Pantelis, G 1999, 'The modelling of flow and chemical reactions in waste piles', in *2nd Internat. Conf. CFD in the Minerals and Process Industries. CSIRO, Melbourne, Australia, December,* pp. 6-8.

Buckley, AN & Woods, R 1987, 'The surface oxidation of pyrite', *Applied Surface Science*, vol. 27, no. 4, 1987/01/01, pp. 437-452.

Chandra, AP & Gerson, AR 2010, 'The mechanisms of pyrite oxidation and leaching: A fundamental perspective', *Surface Science Reports*, vol. 65, no. 9, pp. 293-315.

Chiriță, P & Schlegel, ML 2017, 'Pyrite oxidation in air-equilibrated solutions: An electrochemical study', *Chemical Geology*, vol. 470, pp. 67-74.

da Silva, JC, do Amaral Vargas, E & Sracek, O 2009, 'Modeling Multiphase Reactive Transport in a Waste Rock Pile with Convective Oxygen Supply', *Vadose Zone Journal*, vol. 8, no. 4, pp. 1038-1050.

Davis, GB & Ritchie, AIM 1986, 'A model of oxidation in pyritic mine wastes: part 1 equations and approximate solution', *Applied Mathematical Modelling*, vol. 10, no. 5, pp. 314-322.

de Donato, P, Mustin, C, Benoit, R & Erre, R 1993, 'Spatial distribution of iron and sulphur species on the surface of pyrite', *Applied Surface Science*, vol. 68, no. 1, 1993/05/01, pp. 81-93.

Eggleston, CM, Ehrhardt, JJ & Stumm, W 1996, 'Surface structural controls on pyrite oxidation kinetics: An XPS-UPS, STM, and modeling study', *American Mineralogist*, vol. 81, no. 9-10, pp. 1036-1056.

Elberling, B, Schippers, A & Sand, W 2000, 'Bacterial and chemical oxidation of pyritic mine tailings at low temperatures', *Journal of Contaminant Hydrology*, vol. 41, no. 3–4, pp. 225-238.

Evangelou, VP & Zhang, YL 1995, 'A review: Pyrite oxidation mechanisms and acid mine drainage prevention', *Critical Reviews in Environmental Science and Technology*, vol. 25, no. 2, 1995/05/01, pp. 141-199.

Gerke, HH, Molson, JW & Frind, EO 1998, 'Modelling the effect of chemical heterogeneity on acidification and solute leaching in overburden mine spoils', *Journal of Hydrology*, vol. 209, no. 1, pp. 166-185.

Gleeson, K, Butt, S, O'Callaghan, J & Jones, C 2020, *Lihir Operations Aniolam Island Papua New Guinea NI 43-101 Technical Report*, Newcrest Mining Limited.

Gleisner, M, Herbert, RB & Kockum, PCF 2006, 'Pyrite oxidation by Acidithiobacillus ferrooxidans at various concentrations of dissolved oxygen', *Chemical Geology*, vol. 225, no. 1, pp. 16-29.

Hiskey, JB & Shlitt, WJ 1982, 'Aqueous Oxidation of Pyrite', in WJ Schlitt (ed.), *Interfacing Technologies in Solution Mining,* A.I.M.E., pp. 55-74.

Holmes, PR & Crundwell, FK 2000, 'The kinetics of the oxidation of pyrite by ferric ions and dissolved oxygen: an electrochemical study', *Geochimica et Cosmochimica Acta*, vol. 64, pp. 263-274.

Jerz, JK & Rimstidt, JD 2004, 'Pyrite oxidation in moist air1', *Geochimica et Cosmochimica Acta*, vol. 68, no. 4, 2/15/, pp. 701-714.

Kameia, G & Ohmotob, H 2000, 'The kinetics of reactions between pyrite and O2-bearing water revealed from in situ monitoring of DO, Eh and pH in a closed system', *Geochimica et Cosmochimica Acta*, vol. 64, pp. 2585-2601.

Karthe, S, Szargan, R & Suoninen, E 1993, 'Oxidation of pyrite surfaces: a photoelectron spectroscopic study', *Applied Surface Science*, vol. 72, no. 2, 1993/10/01, pp. 157-170.

Lasaga, AC 1984, 'Chemical kinetics of water-rock interactions', *Journal of Geophysical Research: Solid Earth*, vol. 89, pp. 4009-4025.

Lefebvre, R, Hockley, D, Smolensky, J & Lamontagne, A 2001, 'Multiphase transfer processes in waste rock piles producing acid mine drainage: 2. Applications of numerical simulation', *Journal of Contaminant Hydrology*, vol. 52, pp. 165-186.

Lehner, S & Savage, K 2008, 'The effect of As, Co, and Ni impurities on pyrite oxidation kinetics: Batch and flow-through reactor experiments with synthetic pyrite', *Geochimica et Cosmochimica Acta*, vol. 72, no. 7, 4/1/, pp. 1788-1800.

Lehner, S, Savage, K, Ciobanu, M & Cliffel, DE 2007, 'The effect of As, Co, and Ni impurities on pyrite oxidation kinetics: An electrochemical study of synthetic pyrite', *Geochimica et Cosmochimica Acta*, vol. 71, no. 10, 5/15/, pp. 2491-2509.

León, EA, Rate, A, Hinz, C & Campbell, G 2004, 'Weathering of sulphide minerals at circum-neutral-pH in semi-arid/arid environments: Influence of water content', in *Proc., SuperSoil 2004: 3rd Australian New Zealand Soils Conf*.

Levenspiel, O 1972, 'Chemical reaction engineering', Wiley Eastern Limited.

Lowson, RT 1982, 'Aqueous oxidation of pyrite by molecular oxygen', *Chemical Reviews*, vol. 82, no. 5, pp. 461-497.

Mathews, C & Robins, R 1974, 'Aqueous oxidation of iron disulfide by molecular oxygen', *Australian Chem. Eng*, vol. 15, pp. 19-24.

Mayer, KU, Frind, EO & Blowes, DW 2002, 'Multicomponent reactive transport modeling in variably saturated porous media using a generalized formulation for kinetically controlled reactions', *Water Resources Research*, vol. 38, no. 9, pp. 13-11-13-21.

McKibben, MA & Barnes, HL 1986, 'Oxidation of pyrite in low temperature acidic solutions: Rate laws and surface textures', *Geochimica et Cosmochimica Acta*, vol. 50, no. 7, pp. 1509-1520.

Molson, JW, Fala, O, Aubertin, M & Bussière, B 2005, 'Numerical simulations of pyrite oxidation and acid mine drainage in unsaturated waste rock piles', *Journal of Contaminant Hydrology*, vol. 78, no. 4, pp. 343-371.

Moses, CO & Herman, JS 1991, 'Pyrite oxidation at circumneutral pH', *Geochimica et Cosmochimica Acta*, vol. 55, no. 2, 1991/02/01, pp. 471-482.

Moses, CO, Kirk Nordstrom, D, Herman, JS & Mills, AL 1987, 'Aqueous pyrite oxidation by dissolved oxygen and by ferric iron', *Geochimica et Cosmochimica Acta*, vol. 51, no. 6, 1987/06/01, pp. 1561-1571.

Murphy, R & Strongin, DR 2009, 'Surface reactivity of pyrite and related sulfides', *Surface Science Reports*, vol. 64, no. 1, 1/1/, pp. 1-45.

Mycroft, JR, Bancroft, GM, McIntyre, NS, Lorimer, JW & Hill, IR 1990, 'Detection of sulphur and polysulphides on electrochemically oxidized pyrite surfaces by X-ray photoelectron spectroscopy and Raman spectroscopy', *Journal of Electroanalytical Chemistry and Interfacial Electrochemistry*, vol. 292, no. 1, 1990/10/10, pp. 139-152.

Nicholson, RV, Gillham, RW & Reardon, EJ 1988, 'Pyrite oxidation in carbonate-buffered solution: 1. Experimental kinetics', *Geochimica et Cosmochimica Acta*, vol. 52, no. 5, 1988/05/01, pp. 1077-1085.

Nicholson, RV, Gillham, RW & Reardon, EJ 1990, 'Pyrite oxidation in carbonate-buffered solution: 2. Rate control by oxide coatings', *Geochimica et Cosmochimica Acta*, vol. 54, pp. 395-402.

Olson, GJ 1991, 'Rate of pyrite bioleaching by Thiobacillus ferrooxidans: results of an interlaboratory comparison', *Applied and environmental microbiology*, vol. 57, pp. 642-644.

Pantelis, G 1993, 'FIDHELM: Description of model and users guide', *Australian Nuclear Science and Technology Organisation Report ANSTO M*, vol. 123.

Pantelis, G, Ritchie, A & Stepanyants, Y 2002, 'A conceptual model for the description of oxidation and transport processes in sulphidic waste rock dumps', *Applied Mathematical Modelling*, vol. 26, no. 7, pp. 751-770.

Pesic, B, Oliver, DJ & Wichlacz, P 1989, 'An electrochemical method of measuring the oxidation rate of ferrous to ferric iron with oxygen in the presence of Thiobacillus ferrooxidans', *Biotechnology and Bioengineering*, vol. 33, pp. 428-439.

Pruess, K 1991, *TOUGH2: A general-purpose numerical simulator for multiphase nonisothermal flows*, Lawrence Berkeley Lab., CA (United States).

Pugh, C, Hossner, L & Dixon, J 1984, 'Oxidation rate of iron sulfides as affected by surface area, morphology, oxygen concentration, and autotrophic bacteria', *Soil Science*, vol. 137, no. 5, pp. 309-314.

Qiu, G, Luo, Y, Chen, C, Lv, Q, Tan, W, Liu, F & Liu, C 2016, 'Influence factors for the oxidation of pyrite by oxygen and birnessite in aqueous systems', *Journal of Environmental Sciences*, vol. 45, pp. 164-176.

Rimstidt, JD & Vaughan, DJ 2003, 'Pyrite oxidation: a state-of-the-art assessment of the reaction mechanism', *Geochimica et Cosmochimica Acta*, vol. 67, no. 5, pp. 873-880.

Ritchie, A 2003, 'Oxidation and gas transport in piles of sulfidic material', *Environmental Aspects of Mine Wastes, Short Course*, vol. 31, pp. 73-94.

Rodríguez, Y, Ballester, A, Blázquez, ML, González, F & Muñoz, JA 2003, 'New information on the pyrite bioleaching mechanism at low and high temperature', *Hydrometallurgy*, vol. 71, no. 1, 2003/10/01/, pp. 37-46.

Schaufuß, AG, Nesbitt, HW, Kartio, I, Laajalehto, K, Bancroft, GM & Szargan, R 1998, 'Incipient oxidation of fractured pyrite surfaces in air', *Journal of Electron Spectroscopy and Related Phenomena*, vol. 96, no. 1–3, 11//, pp. 69-82.

Schoonen, M, Elsetinow, A, Borda, M & Strongin, D 2000, 'Effect of temperature and illumination on pyrite oxidation between pH 2 and 6', *Geochemical Transactions*, vol. 1, no. 4, p. 23.

Simunek, J, Sejna, M & Van Genuchten, MT 1999, 'The HYDRUS-2D Software Package', *International Ground Water Modeling Center*.

Singer, PC & Stumm, W 1970, 'Acidic mine drainage: the rate-determining step', *Science*, vol. 167, no. 3921, pp. 1121-1123.

Smith, EE 1970, 'Sulfide to sulfate reaction mechanism : a study of the sulfide to sulfate reaction mechanism as it relates to the formation of acid mine waters'.

Tabelin, CB, Veerawattananun, S, Ito, M, Hiroyoshi, N & Igarashi, T 2017, 'Pyrite oxidation in the presence of hematite and alumina: I. Batch leaching experiments and kinetic modeling calculations', *Science of The Total Environment*, vol. 580, pp. 687-698.

Todd, E, Sherman, D & Purton, J 2003, 'Surface oxidation of pyrite under ambient atmospheric and aqueous (pH= 2 to 10) conditions: electronic structure and mineralogy from X-ray absorption spectroscopy', *Geochimica et Cosmochimica Acta*, vol. 67, no. 5, pp. 881-893.

Walter, A, Frind, E, Blowes, D, Ptacek, C & Molson, J 1994, 'Modeling of multicomponent reactive transport in groundwater: 1. model development and evaluation', *Water Resources Research*, vol. 30, no. 11, pp. 3137-3148.

Wang, H, Dowd, PA & Xu, C 2019, 'A reaction rate model for pyrite oxidation considering the influence of water content and temperature', *Minerals Engineering*, vol. 134, 2019/04/01/, pp. 345-355.

Williamson, MA, Kirby, CS & Rimstidt, JD 2006, 'Iron dynamics in acid mine drainage', in RI Barnhisel (ed.), *International Conference on Acid Rock Drainage (ICARD)*, American Society of Mining and Reclamation (ASMR), St. Louis MO, DOI: 10.21000/JASMR06022411.

Williamson, MA & Rimstidt, JD 1994, 'The kinetics and electrochemical rate-determining step of aqueous pyrite oxidation', *Geochimica et Cosmochimica Acta*, vol. 58, no. 24, pp. 5443-5454.

Wunderly, M, Blowes, D, Frind, E & Ptacek, C 1996, 'Sulfide mineral oxidation and subsequent reactive transport of oxidation products in mine tailings impoundments: A numerical model', *Water Resources Research*, vol. 32, no. 10, pp. 3173-3187.

Xu, T, White, S, Pruess, K & Brimhall, G 2000, 'Modeling of Pyrite Oxidation in Saturated and Unsaturated Subsurface Flow Systems', *Transport in Porous Media*, vol. 39, pp. 25-56.

Chapter 2

A reaction rate model for pyrite oxidation considering the influence of water content and temperature

Statement of Authorship

Title of Paper	A reaction rate model for pyrite oxidation considering the influence of water content and temperature
Publication Status	☑ Published ☐ Accepted for Publication ☐ Submitted for Publication ☐ Unpublished and Unsubmitted work written in manuscript style
Publication Details	Wang, H., Dowd, P.A. and Xu, C. (2019) 'A reaction rate model for pyrite oxidation considering the influence of water content and temperature', *Minerals Engineering*, 134, 345-355, available at: http://dx.doi.org/https://doi.org/10.1016/j.mineng.2019.02.002.

Principal Author

Name of Principal Author (Candidate)	Hang Wang
Contribution to the Paper	Method development, data analysis and manuscript drafting.
Overall percentage (%)	70%
Certification:	This paper reports on original research I conducted during the period of my Higher Degree by Research candidature and is not subject to any obligations or contractual agreements with a third party that would constrain its inclusion in this thesis. I am the primary author of this paper.
Signature	Date 7/04/2021

Co-Author Contributions

By signing the Statement of Authorship, each author certifies that:

i. the candidate's stated contribution to the publication is accurate (as detailed above);

ii. permission is granted for the candidate in include the publication in the thesis; and

iii. the sum of all co-author contributions is equal to 100% less the candidate's stated contribution.

Name of Co-Author	Peter A. Dowd
Contribution to the Paper	Supervision, design of the work and reviewing the manuscript.
Signature	Date 09/04/2021

Name of Co-Author	Chaoshui Xu
Contribution to the Paper	Supervision, design of the work and reviewing the manuscript.
Signature	Date 8-4-2021

Please cut and paste additional co-author panels here as required.

Abstract

Natural oxidation of pyrite in refractory gold bearing rock stockpiles may facilitate the recovery of gold contained in mined low-grade material that was originally sub-economic due to the cost of pre-treatment to oxidise fresh pyrite. The evaluation of this potential requires the oxidation level of pyrite under various conditions. This paper proposes a reaction rate model for prolonged natural oxidation of pyrite under various water saturation conditions and temperatures and a circum-neutral to alkaline pH. The application is to a natural pre-treatment process for refractory gold ore to liberate the gold content encapsulated in pyrite crystals and allow effective cyanidation for gold extraction. The proposed model is based on the shrinking core model with half-order surface reaction on the pyrite surface. It assumes that, in unsaturated water conditions and at circum-neutral to alkaline pH, a diffusion barrier forms on the fresh pyrite surface during the reaction, which prohibits the diffusion of oxygen to the reacting sites and lowers the reaction rate over time. The diffusion barrier may consist of a thin solution film, some precipitations of soluble oxidation products and/or insoluble oxidation products depending on the water saturation and pH. The diffusivity of this diffusion barrier for oxygen is determined as a function of water saturation and temperature. In this model, the concept of effective oxygen concentration is also proposed to represent the change in oxygen concentration at the particle surface due to water; an exponential relationship is found to be appropriate. Based on the reaction rate data reported in the literature, the reaction rate constant in the model for the surface reaction is determined as 5×10^{-8} $mol^{0.5} \cdot m^{-0.5} \cdot s^{-1}$ while the diffusion coefficient is 1.2×10^{-15} $m^2 \cdot s^{-1}$ for water saturation of 25% and above and 4.7×10^{-19} $m^2 \cdot s^{-1}$ for 0.1% water saturation. This rate model can be used for predicting and modelling the level of pyrite oxidation in rock piles or mine tailings where various unsaturated water conditions and circum-neutral to alkaline pH apply.

2.1 Introduction

Pre-treatment, such as pressure oxidation (POX), bio-oxidation, roasting or ultrafine grinding, is required for effective cyanidation of refractory gold ore (La Brooy et al., 1994), which increases the processing cost. Some *in situ* low-grade refractory gold-bearing material, although containing potentially economic amounts of gold, is uneconomic to mine and process due to the relatively high processing cost of current processing technology. In many gold deposits, this low-grade material must be mined for access purposes but is then stored either for later disposal or for potential processing after active mining ceases (Ketcham et al., 1993) . However, over long periods of time (e.g., twenty years), natural oxidation of pyrite can occur within stockpiles when the pyrite is exposed either to atmospheric water and oxygen or to aqueous water with dissolved oxygen and the material becomes partially oxidised. This may reduce or eliminate the need for pre-treatment of the material and render its processing economically viable. An example is the Lihir orebody on Aniolam Island in the New Ireland Province of Papua New Guinea where a small, low-grade oxide resource yielded gold recoveries of 90% or higher in direct cyanide leaching (Ketcham et al., 1993). The extent of these stockpiles and the discovery of more low-grade refractory gold deposits has stimulated an interest in studying the potential of natural oxidation as a possible alternative to hydrometallurgy, which could improve gold recovery and contribute to the profitability of mining operations. The initial requirement to evaluate this potential is knowledge of the oxidation level and its distribution over the stockpile. To this end, it is essential to understand the reaction rate for prolonged pyrite oxidation under different possible reaction conditions in the stockpiles. The possible reaction conditions that would affect the rate of pyrite oxidation include various pH environments (acidic, neutral or alkaline), levels of water saturation, temperature and microbial activity.

The oxidation of pyrite and its reaction rate have been studied extensively in the context of acid mine drainage (AMD), which is often associated with low pH and intro-aqueous conditions. It is widely accepted that pyrite oxidation under subaqueous conditions mainly involves four reactions: (1) pyrite is oxidised by oxygen (Eq. (2-1)), which initiates the oxidation process; (2) the ferrous ion produced in Eq. (2-1) is oxidised to ferric ion by oxygen (Eq. (2-2)); (3) the ferric ion oxidises the pyrite (Eq. (2-3)) and (4) ferric ion hydrolyses when the pH value is above 3 (Eq. (2-4)).

$$2\mathrm{Fe}S_2 + 7O_2 + 2H_2O \rightarrow 2Fe^{2+} + 4{SO_4}^{2-} + 4H^+ \quad (2\text{-}1)$$

$$4Fe^{2+} + O_2 + 4H^+ \rightarrow 4Fe^{3+} + 2H_2O \quad (2\text{-}2)$$

$$\mathrm{Fe}S_2 + 14Fe^{3+} + 8H_2O \rightarrow 15Fe^{2+} + 2{SO_4}^{2-} + 16H^+ \quad (2\text{-}3)$$

$$Fe^{3+} + 3H_2O \rightarrow Fe(OH)_3 + 3H^+ \quad (2\text{-}4)$$

Table 2-1: The rate laws of the key reactions for pyrite oxidation

Reference	Rate law	Unit	pH
McKibben and Barnes (1986)	$R_{py,O_2} = -10^{-9.77} M_{DO}^{0.5}$	mol·cm^{-2}·min^{-1}	2 - 4
	$R_{py,Fe^{3+}} = -10^{-9.74} M_{Fe^{3+}}^{0.5} M_{H^+}^{-0.5}$	mol·cm^{-2}·min^{-1}	2 - 4
Williamson and Rimstidt (1994)	$R_{py,O_2} = 10^{-8.19(\pm 0.1)} M_{DO}^{0.5(\pm 00.04)} M_{H^+}^{-0.11(\pm 0.01)}$	mol·m^{-2}·s^{-1}	2 - 10
	$R_{py,Fe^{3+}} = 10^{-6.07(\pm 0.57)} M_{Fe^{3+}}^{0.93(\pm 0.07)} M_{Fe^{2+}}^{-0.4(\pm 0.06)}$	mol·m^{-2}·s^{-1}	2 - 10
Pesic et al. (1989)	$R_{Fe^{2+},O_2} = k[Fe^{2+}]^2[H^+]^{1/4} P_{O_2}$		Acidic
	$R_{Fe^{2+},O_2} = k[Fe^{2+}][OH^-]^2 P_{O_2}$		Neutral/ alkaline
	$R_{Fe^{2+},O_2} = 1.62 \times 10^{11} C_{bact}[Fe^{2+}] P_{O_2} e^{-\left(\frac{58.77}{RT}\right)}$		< 2.2
	$R_{Fe^{2+},O_2} = 1.62 \times 10^{11} C_{bact}[H^+][Fe^{2+}] P_{O_2} e^{-\left(\frac{58.77}{RT}\right)}$		> 2.2
Holmes and Crundwell (2000)	$R_{py,O_2} = k[H^+]^{-0.18}[O_2]^{0.5}$		1.5 – 3.5
Kameia and Ohmotob (2000)	$R_{py,O_2} = -10^{-5.3 \pm 0.5} M_{DO}$	mol·m^{-2}·s^{-1}	5.7 ± 0.3
Huminicki and Rimstidt (2009)	$R_{py,O_2} = \frac{1}{2}\left(\sqrt{\frac{2000 m_{(sol)} DA(1-\varphi)}{\nu_i f_{ppt} V_m}}\right) t^{-0.5}$		Alkaline
Moses and Herman (1991)	$R_{py,O_2} = 10^{-3.23}\left(\frac{A}{V}\right)$	µmol·s^{-1}	6 - 7
Nicholson et al. (1990)	$R_{py,O_2} = \alpha R^2 / (\frac{R(R-r)}{r D_s} + \frac{R^2}{r^2 k''})$		6.7 - 8.5
Jerz and Rimstidt (2004)	$R_{py,O_2} = 10^{-6.6} P^{0.5} t^{-0.5}$	mol·m^{-2}·s^{-1}	Neutral

$R_{a,b}$: the oxidation rate of a by b.

Both oxygen and ferric ion can oxidise pyrite and often these two reactions (Eq. (2-1) and Eq. (2-3)) occur simultaneously in acidic solution. Previous studies (Holmes and Crundwell, 2000; Kameia and Ohmotob, 2000; McKibben and Barnes, 1986; Williamson and Rimstidt, 1994) have determined the rate laws for the aqueous oxidation of pyrite by dissolved oxygen within a given pH range (see Table 2-1). Williamson and Rimstidt (1994) also proposed a rate law for pyrite oxidation by ferric ion. The reaction rate of the former is much higher than that of the latter (Singer and Stumm, 1970). However, the oxidation of pyrite by ferric ion is subject to the availability of ferric ion in solution. Hence, Singer and Stumm (1970) suggested that the abiotic oxidation of ferrous ion by oxygen (Eq.(2-2)) is the rate-determining step in the overall process of pyrite oxidation in AMD. Pesic et al. (1989) summarised the rate laws for this reaction step in acidic media at neutral or higher pH values (see Table 2-1). The rate of the abiotic oxygenation of ferrous ion was found to be strongly dependent on the pH value: the rate increases rapidly with pH when its value is above 4 (Williamson et al., 2006). In cases where there is microbial activity, especially at low pH values, the oxidation of ferrous ion by oxygen is catalysed by bacteria such as *Thiobacillus sp*. and *Leptospirillium sp*. (Evangelou and Zhang, 1995; Singer and Stumm, 1970; Williamson et al., 2006). Pesic et al. (1989) found that the microbial oxidation rate of ferrous ion increases with the concentration of bacteria and

oxygen; they derived the rate law shown in Table 2-1 for the microbial oxidation of ferrous ion. The microbial oxidation rate of pyrite was measured in Olson (1991) and Gleisner et al. (2006) and was found to be significantly higher than the abiotic oxidation rate if the pH value is less than 2. Yu et al. (2001) found a lag phase of about 400 hours before bacteria accelerate the reaction rate. Williamson et al. (2006) provided a quantitative comparison of iron transformation rates in these reactions in the context of AMD and concluded that the oxidation of pyrite (by either oxygen or ferric ion), rather than the oxidation of ferrous ion, is the rate-determining step in both the initiating stage and the propagation of AMD. Overall, studies of pyrite oxidation under AMD have shown that pH value and microbial activities are important influencing factors: for high pH (greater than 4), the aqueous oxidation rate of pyrite is the rate at which pyrite is oxidised by dissolved oxygen (Eq. (2-1)); when the pH is less than 4, ferric ion is sufficiently replenished from the bacteria-catalysed oxygenation of ferrous ion and the aqueous oxidation rate of pyrite is the rate at which pyrite is oxidised by ferric ion. For AMD, in the unlikely case of abiotic conditions at low pH, the oxidation rate is limited by the abiotic oxidation of ferrous ion.

In AMD the pH is rarely above 4 and the entire system is mostly under subaqueous conditions with frequent water flow. In non-AMD environments, pyrite oxidation also occurs under neutral to alkaline pH and/or unsaturated water conditions. Moses and Herman (1991) measured the oxidation rate of pyrite with pH 6 and 7 and the reaction rate constant was determined as $10^{-3.23}$ for the proposed rate law that assumes first order kinetics with respect to the ratio of total surface area to reaction solution volume ($\frac{A}{V}$ in $m^2 \cdot L^{-1}$) (see Table 2-1). Nicholson et al. (1988, 1990) and Huminicki and Rimstidt (2009) measured the rate of pyrite oxidation at neutral to high pH in carbonate-buffered solutions over time and found that the reaction rate decreased with time due to the Fe oxyhydroxide coating that developed on the pyrite surface. Nicholson et al. (1990) used the shrinking core model to fit the reaction rate over time considering the Fe oxyhydroxide coating; the shrinking core model parameters (D_s and k'' in Table 2-1) were determined for each experiment run with different pyrite grain size. Huminicki and Rimstidt (2009) compared the amount of Fe precipitated onto the grain surface with the calculated Fe product and inferred that only 3% of Fe released from pyrite oxidation precipitated on the pyrite surface. They further determined a rate law of prolonged pyrite oxidation as a function of time considering the diffusion of oxygen through the Fe oxyhydroxide coating (Table 2-1). For cases where pyrite is oxidised under unsaturated water conditions, Jerz and Rimstidt (2004) investigated the oxidation rate of dried pyrite in moist air and observed that at the initial stage (several hours), the reaction rate is significantly higher than the aqueous oxidation rate but soon decreases to a level below the aqueous oxidation rate; a rate law was determined as a function of the reaction time and oxygen partial pressure (Table 2-1). León et al. (2004) measured the pyrite oxidation rate for water saturation of 0.1%, 25%, 70%, 95% and found that the oxidation rate increased from practically no saturation (0.1%), reached a maximum at 25% saturation and thereafter decreased, which indicates a non-monotonic influence of water content. Field observations of pyritic mine tailings in Elberling et al. (2000) also showed that the oxidation rate of pyrite is much faster in well-drained sites than in wet sites. An experimental study that investigated the release of

hazardous trace elements in Tamoto et al. (2015) also found that higher water saturation lowers the leachabilities of the trace elements released from pyrite oxidation. These studies show that water condition is another important factor that influences the rate of pyrite oxidation. However, it has rarely been considered in the rate models for pyrite oxidation.

Predicting the level of pyrite oxidation in rock stockpiles requires the oxidation rate under various conditions. Water content is often a relevant condition in rock stockpiles as is temperature since pyrite oxidation is an exothermic reaction. The rate laws published in the literature for pyrite oxidation cover the following situations: (1) initial oxidation rate in acidic, neutral and alkaline solutions (subaqueous conditions) with or without microbial activity; (2) time-dependent oxidation rates at high pH values in carbonate buffered solutions considering the development of Fe oxyhydroxide coating on a pyrite surface and (3) time-dependent oxidation rate for atmospheric oxidation of pyrite. However, a reaction rate law that incorporates the influences of water saturation and temperature for prolonged pyrite oxidation is not available, although studies have been conducted to investigate the influence of these two factors. As a result, the oxidation rates used in the modelling of pyrite oxidation over time in rock stockpiles or waste dumps are based on the rate laws available in the literature; and the influencing factors, such as water condition and temperature, have been neglected or simplified in the model simulation. For example, Elberling et al. (1994) used a uniform reaction rate formula for pyrite oxidation at all depths in a tailing with first-order kinetics considering only oxygen concentration. A similar approach can also be found in Ardejani et al. (2014). Wunderly et al. (1996) and Molson et al. (2005) assume that the pyrite oxidation rate is relatively fast and the volumetric reaction rate is completely controlled by the diffusion of oxygen through the host rock that contains evenly distributed pyrite; based on this, a diffusion-controlled shrinking core model is used to describe pyrite oxidation in the host rock. Lefebvre et al. (2001) and Xu et al. (2000) considered the effect of temperature and water conditions on the oxidation rate in their models but a simple scaling factor between 0 to 1 is used to give different reaction rates with different temperatures and water saturations. These assumptions and simplifications may be acceptable for predicting acid mine drainage and the reactive transport of the reaction species in waste rock piles and tailings but are not suitable for predicting the pyrite oxidation level, which is the fundamental input for the evaluation of low-grade refractory gold-bearing material.

The objective of this paper is to fill this research gap by focusing on the rate of prolonged pyrite oxidation in non-AMD environments for the purpose of modelling and predicting the pyrite oxidation level in rock stockpiles. Although the starting point of this study is to facilitate the re-evaluation of low-grade refractory gold-bearing material, the research work on the rate of pyrite oxidation in this study is generic because pyrite oxidation in non-AMD environments with circum-neutral to alkaline pH and unsaturated water conditions is also an important geochemical process that is often associated with the mobility of toxic elements in sulphide and carbonate rich wastes, excavations in urban constructions or aquifer systems (see Tabelin et al. (2018) and Karikari-Yeboah et al. (2018)). Furthermore, AMD caused by pyrite oxidation must be initiated in water with circum-neutral pH before acidity is produced. In this study, we focus on the quantitative effects of water content and temperature on pyrite oxidation rate

over time. We review the reaction rate data measured over time in León et al. (2004), Jerz and Rimstidt (2004) and Nicholson et al. (1988) within the framework of the shrinking core model to investigate the quantitative effect of water saturation and temperature. A new reaction rate model for pyrite oxidation under various water conditions and temperatures is then derived based on the shrinking core model and the values of the key parameters obtained from our analyses.

2.2 Methods and materials

The derivation of the reaction rate model for pyrite oxidation requires reaction rates measured over time under different conditions. León et al. (2004) measured the reaction rates of pyrite oxidation over twelve weeks under different water conditions with neutral to slightly alkaline pH. Pyrite oxidation rates over time were also reported in Nicholson et al. (1990) and Jerz and Rimstidt (2004) for partially saturated conditions and in moist air respectively. In this study, reaction rate data from León et al. (2004) are used to determine the quantitative effect of water saturation. Data from Nicholson et al. (1990) and Jerz and Rimstidt (2004) are used for comparison and validation. The effects of temperature are incorporated on the basis of the measured activation energy as reported in the literature.

In the remaining part of this section, the model derivation process is introduced. Firstly, the experimental data from the literature used in this study are all converted to the same units based on the same type of specific surface area for model fitting and data comparison. The present model is based on the shrinking core model with modification to account for the half-order surface reaction. The surface reaction rates based on the measured initial oxidation rates available in the literature are then determined. The effect of water content is then analysed and incorporated in the proposed model. Finally, in the results section, the oxygen diffusion coefficient in this model is determined by least squares fitting of the experimental data using the model.

2.2.1 Data treatment considering the specific surface area

The method for calculating the specific surface area ($m^2 \cdot g^{-1}$) in different studies is worth noting since the surface reaction rate ($mol \cdot m^{-2} \cdot s^{-1}$) was obtained by dividing the amount of change in the reactants or products in reaction by the total surface area of pyrite. Jerz and Rimstidt (2004) used the BET (Brunauer, Emmett and Teller) method to measure the surface area of the sample, which includes the pore size distribution and is based on the physical adsorption of gas molecules on solid surfaces. In Nicholson et al. (1988), the specific surface area was calculated from the particle size, as the product of the number of particles per gram of sample and the surface area of a single (spherical) particle, which results in the expression:

$$A_s = \frac{6}{\rho d} \tag{2-5}$$

where ρ is the pyrite density and d is the particle diameter. The measured and calculated specific surface area in different studies can differ significantly as demonstrated in Table 2-2. For comparison, the reaction rate data used in the present study are normalised to the surface

reaction rate ($mol \cdot m^{-2} \cdot s^{-1}$) by the calculated specific surface area using Eq.(2-5). The conversion factors are given in Table 2-3.

Table 2-2: Pyrite grain size and specific surface area (SSA) used in different studies of pyrite oxidation rate: in studies where surface area is measured, the measured SSA is used to calculate the surface reaction rate

Reference	Grain size (µm)	SSA ($cm^{-2} \cdot g^{-1}$)	
		Calculated	Measured
McKibben and Barnes (1986)	187.5 (125 – 250)	64	251
Moses and Herman (1991)	41.5 (38 – 45)	289	660
Williamson and Rimstidt (1994)	200 (150 -250)	60	470
Kameia and Ohmotob (2000)	125.5 (74-177)	96	538
Jerz and Rimstidt (2004)	335 (250 – 420)	36	100
Gleisner et al. (2006)	156.5 (63 – 250)	77	1470
Nicholson et al. (1990)	108 (90 – 125)	110	--
León et al. (2004)	108 (90 – 125)	110	--
Tabelin et al. (2017)	605 (500-710)	20	240
Qiu et al. (2016)	<74	162	13000

Table 2-3: Conversion factors for the reaction data used in the model fitting: converted from original units to mol-pyrite/m^2/s

Ref.	Original unit	Measured SSA (m^2/g)	Calculated SSA (m^2/g)	Conversion factor
1	mol-pyrite/cm^2/min	0.0251	0.0064	653.65
2	mol-pyrite/g/h	--	0.0158	0.0176
3	µmol-pyrite/s @2.5 g pyrite	0.066	0.0289	1.38E-05
4	mol-pyrite/m^2/s	0.047	0.006	7.833
5	mol-O2/m^2/s	0.011	0.00358	0.7976
6	mg-SO_4^{2-}/kg-sample/day @ 5% pyrite in sample	0.011	0.00358	1.095E-10

1: *McKibben and Barnes (1986)*
2: *Nicholson et al. (1988, 1990)*
3: *Moses and Herman (1991)*
4: *Williamson and Rimstidt (1994)*
5: *Jerz and Rimstidt (2004)*
6: *León et al. (2004)*

2.2.2 Modification of the shrinking core model

We use the theory of the shrinking core model (SCM) to predict the reaction rate of prolonged pyrite oxidation. The shrinking core model was first proposed by Yagi and Kunii (Yagi and Kunii, 1955, 1961). They visualized five steps during a typical gas-solid reaction, mainly including two types of processes: diffusion of gaseous reactant from the bulk phase to the reacting surface (through the gas film and the oxidized layer); and the reaction of the gaseous reactant with the solid at the reacting surface. Based on this idea, Szekely et al. (1976) and Levenspiel (1972) developed a detailed mathematical model to describe and predict the reaction process,

known as the shrinking core model, in which the rate of pyrite destruction is given by Eq.(2-6) (assuming that resistance of diffusion through the gas film is negligible):

$$-\frac{dN}{dt}=\frac{4\pi R^2 bC}{\frac{R}{D_s}\left(\frac{R}{r_c}-1\right)+\frac{1}{k''}\frac{R^2}{r_c^2}} \tag{2-6}$$

where $\frac{dN}{dt}$ is the pyrite destruction rate, b is the stoichiometric coefficient (mole of pyrite oxidized per mole of oxygen), R is the initial radius of pyrite particles, r_c is the radius of the unreacted core, D_s is the effective diffusion coefficient for oxygen through the oxidised layer, k'' is the reaction rate constant for the surface reaction with respect to oxygen consumption and C is the oxygen concentration.

As the reaction proceeds, the radius of the unreacted core r_c decreases from R to zero if eventually the pyrite particle is completed reacted. The change rate of r_c is given by Eq. (2-7):

$$-\frac{dr_c}{dt}=\frac{bC/\rho_B}{\frac{(R-r_c)r_c}{RD_s}+\frac{1}{k''}} \tag{2-7}$$

where ρ_B is the pyrite molar density.

The original shrinking core model assumes that the surface reaction rate is of first-order with respect to oxygen concentration. However, many recent studies have shown that the surface reaction rate is of half-order with respect to oxygen concentration, as can be seen in the rate laws listed in Table 2-1. To incorporate this in the shrinking core model, the governing equation, assuming that the surface reaction is of half-order with respect to oxygen concentration, is derived as Eq. (2-8) (see Appendix 2.A for details):

$$\begin{cases}(a) & -\dfrac{dN}{dt}=\dfrac{4\pi R^2 bC}{\frac{R}{D_s}\left(\frac{R}{r_c}-1\right)+\frac{1}{k''}\frac{R^2}{r_c^2}C^{0.5}} \\ (b) & -\dfrac{dr_c}{dt}=\dfrac{bC/\rho_B}{\frac{(R-r_c)r_c}{RD_s}+\frac{C^{0.5}}{k''}}\end{cases} \tag{2-8}$$

2.2.3 Determination of the surface reaction rate constant

To be able to predict the reaction rate for pyrite oxidation, the values of D_s and k'' under various experimental conditions must be determined. In this study, D_s will be determined by fitting the shrinking core model to the experimental data. The value of k'' can be obtained from the initial reaction rate of pyrite oxidation based on the half-order reaction rate law:

$$Rate_{pyrite}=bk''C^{0.5} \tag{2-9}$$

The initial reaction rate of pyrite oxidation has been measured in many studies either in solution or in air. From the initial reaction rate reported in the literature, the rate constant can be calculated based on Eq. (2-9). Table 2-4 lists some of the initial reaction rates reported

in different studies with the summarised experimental conditions including pH, pyrite grain size and oxygen concentration. Based on this information, the values of k'' for different studies were calculated as shown in Table 2-4. Note that all listed reaction rates are converted to specific reaction rates in mol·m^{-2}·s^{-1} based on the calculated specific surface area; the oxygen concentration in Eq. (2-9) is in mol·m^{-3}; the value of the stoichiometric coefficient b is given as 2/7 by Eq. (2-1). The average value of k'' for these five studies is 5 × 10^{-8} mol$^{0.5}$·m$^{-0.5}$·s^{-1} and this value of k'' will be used in this study.

Table 2-4: Initial oxidation rate (IOR) of pyrite oxidation measured in the literature and the calculated reaction rate constant k''

Ref.	pH	Pyrite grain size (μm)	SSA_m (m^{-2}·g^{-1})	IOR (mol·m^{-2}·s^{-1})	O2 Conc. (mol·m^{-3})	k'' (mol$^{0.5}$·m$^{-0.5}$·s^{-1})
1	1.9	125-250	0.0251	$10^{-8.76}$	0.237	1.23E-08
2	6.7-8.5	180-250	N/A	$10^{-8.92}$	0.258	8.23E-09
3	6-7	38-45	0.066	$10^{-7.86}$	0.0268	9.35E-08
4	2-10	150-250	0.047	$10^{-8.21}$	0.258	4.25E-08
5	<7	250-420	0.01	$10^{-7.10}$	8.7	9.42E-08
				Average		5.01E-08

1: McKibben and Barnes (1986)
2: Nicholson et al. (1988)
3: Moses and Herman (1991)
4: Williamson and Rimstidt (1994)
5: Jerz and Rimstidt (2004)

2.2.4 The effect of water content

León et al. (2004) showed that the degree of water saturation significantly affects the oxidation rate and partial water saturation (around 25%) is the most conducive to the reaction. Welch et al. (1990) also reported a similar trend for the total oxygen consumption by pyrite for different water contents. This non-monotonic behaviour of pyrite oxidation for different water content may result from two roles that water plays in the pyrite oxidation reaction. On one hand, increasing water saturation prohibits oxygen diffusion from the gas phase to the pyrite surface and also decreases the oxygen concentration due to lower solubility of oxygen in water than in air. From this perspective, excessive water content can decrease the reaction rate of pyrite oxidation. On the other hand, insufficient water content leads to the super-saturation and precipitation of the soluble reaction products. The precipitations could resist the diffusion of oxygen to the fresh pyrite surface and hence lower the reaction rate. Based on this discussion, the effect of water content on the oxidation rate of pyrite is summarised as: an increase in water content would decrease the oxygen concentration C while increasing the diffusivity of the diffusion barrier D_s.

For the D_s value of the diffusion barrier, it is reasonable to assume that when there is sufficient water (e.g. above 25% water saturation based on the reaction rate data from León et al. (2004)) to dissolve all the soluble oxidation products, the diffusion coefficient D_s is a constant. When there is insufficient water to dissolve all soluble oxidation products, the value of D_s decreases as the water content decreases and reaches the minimum under dry conditions. Based on this assumption, the value of D_s takes the following form considering the effect of the water condition (θ_w represents the water saturation):

$$D_s = \begin{cases} constant & when\ \theta_w \geq 25\% \\ f(\theta_w) & when\ 0 < \theta_w < 25\% \end{cases} \tag{2-10}$$

In this study, for the oxygen concentration affected by water, we use the concept of effective oxygen concentration to approximate the actual oxygen concentration at the particle surface affected by the degree of water saturation. The effective oxygen concentration is given by the oxygen concentration C_g in the gas phase (in air-filled pore space) and a factor F the value of which depends on the degree of water saturation θ_w:

$$C_e(\theta_w) = C_g \cdot F(\theta_w) \tag{2-11}$$

For the atmospheric pyrite oxidation, the concentration of oxygen is the atmospheric oxygen concentration; and for pyrite oxidation submerged in solution, the oxygen concentration is given by oxygen solubility in water. Hence, the following relationships must be included in Eq. (2-11):

$$\begin{cases} C_e(\theta_w = 0) = C_g, & hence\ \ F(\theta_w = 0) = 1 \\ C_e(\theta_w = 1) = C_g \cdot H^{cc}, & hence\ F(\theta_w = 1) = H^{cc} \end{cases} \tag{2-12}$$

where H^{cc} is the dimensionless Henry's law solubility, which has a value of 0.03527 for oxygen at 20 ℃. An exponential relationship is proposed for Eq. (2-12):

$$F(\theta_w) = e^{\log(H^{cc}) \cdot \theta_w} \tag{2-13}$$

and therefore,

$$C_e(\theta_w) = C_g \cdot e^{\log(H^{cc}) \cdot \theta_w} \tag{2-14}$$

and the oxygen concentration C in Eq. (2-8) should then be replaced with Eq. (2-14).

The values of D_s under different water conditions are then determined by fitting Eq. (2-8) and (2-14) to the experimental data.

2.3 Results and discussion

Based on the hypothesis in this study, the reaction rate data from León et al. (2004) are fitted using Eq. (2-8) and (2-14) to determine the value of D_s for two water conditions: 1) when water saturation is greater than or equal to 25% and 2) when water saturation is 0.1%. The values of the other parameters in Eq. (2-8) are given in Table 2-5.

Table 2-5: The parameters used for fitting the rate model to the rate data in León et al. (2004)

Parameters	Descriptions	Unit	Value
ρ_B	Molar density of pyrite	mol·m^{-3}	41674
C_g	O2 concentration in gas phase	mol·m^{-3}	8.73
b	Stoichiometric coefficient	Dimensionless	2/7
R	Radius of pyrite particle	μm	108/2
k''	Reaction rate constant	mol$^{0.5}$·m$^{-0.5}$ ·s^{-1}	5×10^{-8}
H^{cc}	Henry's law solubility	Dimensionless	0.0353

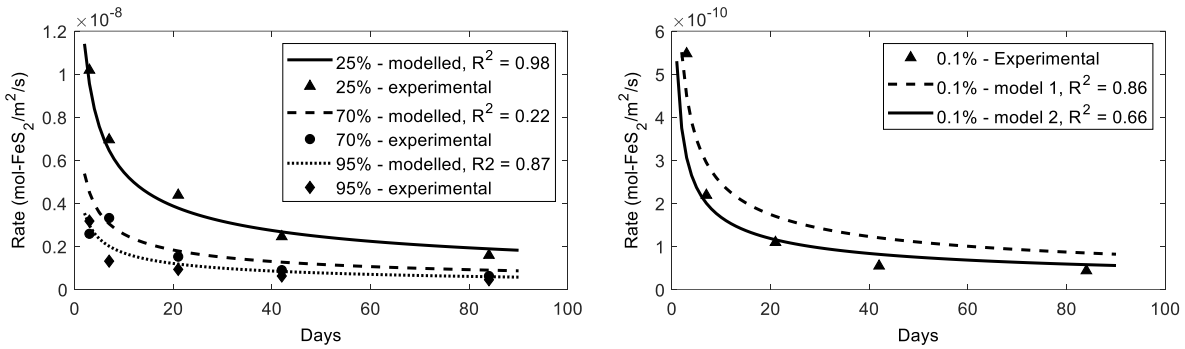

Fig. 2-1: SCM fitted for reaction rate data in León et al. (2004) with different water saturation: (a) water saturation of 25%, 70% and 95%; (b) water saturation of 0.1%

Fig. 2-1 compares the fitted curve and the experimental data. For water saturation above 25% (Fig. 2-1 (a)), the best fitting value of D_s is 1.2 × 10^{-15} m^2·s^{-1} with an overall R-square value of 0.94; the R-square values for reaction rate data under the three different water saturations are 0.98 (25% water saturation), 0.22 (70% water saturation) and 0.87 (95% water saturation) respectively. The low R-square value for the case with 70% water saturation is due to the abnormally low oxidation rate measured on day 3 compared with the trend shown by the other data sets and predicted by the shrinking core model (excluding this point gives an R-square value of 0.92). For the case with water saturation of 0.1%, the "best" fit curve for the experimental data is shown as the dashed line in Fig. 2-1 (b) with the highest R-square value of 0.86 and a D_s value of 1 ×10^{-18} m^2·s^{-1}. However, the modelled results significantly deviate from all the data points except for the first one. As the data set shows high sensitivity to the reaction time before day 9, another curve is fitted excluding the first point and is shown as the solid line in Fig. 2-1 (b). The fitted D_s for this case is 4.7 ×10^{-19} m^2·s^{-1}; the R-square is 0.66 for the overall data set and is 0.93 excluding the first data point. Considering the sensitivity of the reaction rate to reaction time at the start of the reaction, the second fitted curve is more appropriate to describe the oxidation rate over time than the first one.

For cases where the water saturation is between 0.1% and 25%, the value of D_s is unknown due to lack of experimental data and has to be estimated. In addition, the threshold value of the degree of water saturation, such that all soluble oxidation products are dissolved, needs further investigation (currently 25% is assumed based on the available rate data). In the absence of further investigation, it is reasonable to assume that D_s is linearly proportional to the degree of water saturation over the range of 0.1% to 25%, which results in:

$$\begin{cases} D_s = 1.2 \times 10^{-15} & (for\ \theta_w \geq 25\%) \\ D_s = -4.35 \times 10^{-18} + 4.82 \times 10^{-15} \cdot \theta_w & (for\ 0.1\% \leq \theta_w < 25\%) \end{cases} \quad (2\text{-}15)$$

The value of k'' for the half-order surface reaction as discussed above, is given as:

$$k'' = 5 \times 10^{-8} \quad (2\text{-}16)$$

The proposed reaction rate model for pyrite oxidation in neutral to high pH environments is now given by Eq. (2-8), (2-14), (2-15) and (2-16). The input variables for pyrite oxidation prediction are the oxygen concentration in the gas phase C_g, degree of water saturation θ_w and particle size (radius) R. The other two parameters in Eq. (2-8), the stoichiometric coefficient b and the molar density of pyrite ρ_B, are constants.

2.3.1 Comparison with other studies

To validate the proposed reaction rate model, the model is also fitted to the reaction rate data from Jerz and Rimstidt (2004) and Nicholson et al. (1990). Note that the experimental temperatures in Jerz and Rimstidt (2004) and Nicholson et al. (1990) are both 25 °C while the proposed model is based on 20 °C. Thus, the effect of temperature must be considered in the validation using these reaction rate data.

The reaction rate dependence on temperature can be generally described by the Arrhenius equation:

$$k = Ae^{-\frac{E_a}{\bar{R}T}} \quad (2\text{-}17)$$

where k is the reaction rate constant, E_a is the activation energy of the reaction, $\bar{R}$ is the gas constant, T is the absolute temperature and A is the pre-exponential factor.

The measured activation energy E_a for pyrite oxidation, as published in the literature, varies from 19.1 KJ·mol^{-1} to 121.1 KJ·mol^{-1} (Chiriță and Schlegel, 2017; Schoonen et al., 2000). But in most cases, the measured value is below 90 kJ·mol^{-1} (e.g. in Chiriță and Schlegel (2017), Smith (1970) and McKibben and Barnes (1986)). Lasaga (1984) suggested that the diffusion-controlled reaction would have an activation energy close to 20 kJ·mol^{-1} which indicates that the temperature dependence of the oxygen diffusion coefficient D_s can be approximated using the Arrhenius equation with an activation energy of approximately 20 kJ·mol^{-1}. Based on this information, it is reasonable to assume that the values of E_a for diffusion and surface

reaction are 20 kJ·mol^{-1} and 90 kJ·mol^{-1} respectively. Hence, the diffusion coefficient and the surface reaction rate constant in the shrinking core model can be expressed as in Eq. (2-18) to account for the effect of temperature:

$$\begin{cases} D_s = D_s^0 \cdot e^{\frac{-E_a^D}{R}(\frac{1}{T}-\frac{1}{T_0})} \\ k'' = k_0'' \cdot e^{\frac{-E_a^k}{R}(\frac{1}{T}-\frac{1}{T_0})} \end{cases} \quad (2\text{-}18)$$

where D_s^0 and k_0'' are the values at the reference temperature T_0 as given in Eq. (2-15) and (2-16) at 20°C; E_a^D and E_a^k are the activation energies for diffusion and surface reaction respectively; T is the reaction temperature and $\bar{R}$ is the gas constant with a value of 8.314. The reaction rate under different temperatures can then be estimated by incorporating Eq. (2-18) into the governing equation of Eq. (2-8).

After considering the effect of temperature, a comparison of the modelled results with the reaction rate data from Nicholson et al. (1990) and Jerz and Rimstidt (2004) is shown in Fig. 2-2 and Fig. 2-4.

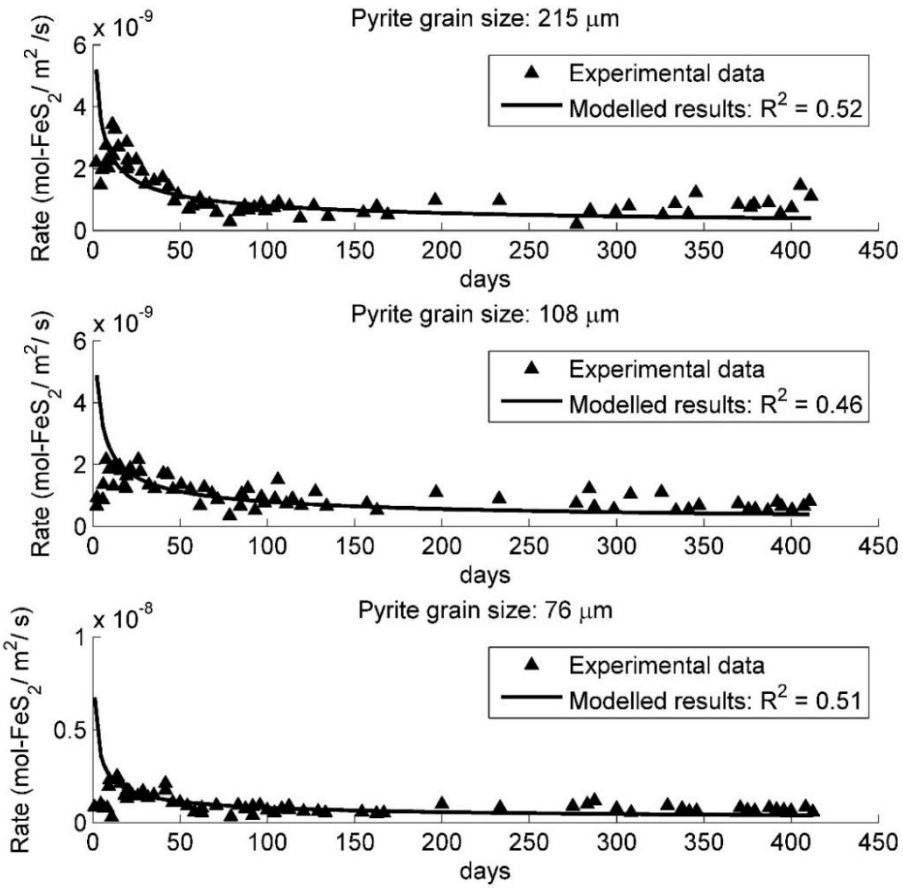

Fig. 2-2: Comparison of the modelled results and the experimental data from Nicholson et al. (1990) for pyrite samples with particle sizes of 215, 108 and 76 microns respectively. The reaction rate data before 20 days are excluded in the calculation of R-square values considering the "abnormality" of the reaction rate data at the start of the reaction.

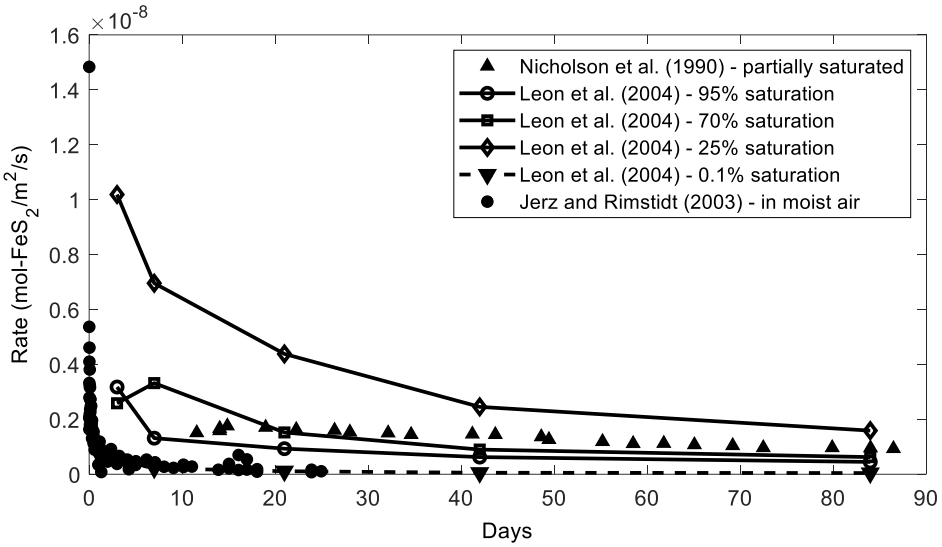

Fig. 2-3: Comparison of the reaction data for pyrite oxidation in Nicholson et al. (1990), León et al. (2004) and Jerz and Rimstidt (2004)

In Fig. 2-2, the modelled results are a very good fit to the experimental data for different pyrite particle sizes after around 20 days. However, the modelled results are higher than the experimental data for the initial oxidation rate. This is due to the fact that the measured initial oxidation rate in Nicholson et al. (1990) is significantly less than that reported in other studies. This can be seen in Table 2-4 and Fig. 2-3 where the initial reaction rate constant and the experimental reaction rate in Nicholson et al. (1990) are compared with those in other studies. The corresponding R-square values of the fittings in Fig. 2-2 are 0.52, 0.46 and 0.51 respectively if the data for the first 20 days are excluded and are 0.29, -2.36 and -2.24 respectively if those data points are included. The negative values of R-square suggest that the proposed model is unable to represent the initial ascending trend of the reaction rates that appears in the modelled data sets. The estimated water saturation for pyrite oxidation in Nicholson et al. (1990) is around 90%, which is a reasonable estimate given the experiment description in the original paper. Despite the discrepancy for the initial oxidation rate, the proposed rate model in this study is validated for prolonged pyrite oxidation with various pyrite particle sizes. In the original paper Nicholson et al. (1990), the shrinking core model is also fitted to the oxidation rate over time. The difference between the Nicholson et al. (1990) fitting and the current model is that the former assumed first-order surface reaction (i.e. Eq. (2-6) was used) and used oxygen concentration in the atmosphere as the input for oxygen concentration although the reaction occurred in a partially saturated condition. The fitted values for k'' and D_s in the Nicholson et al. (1990) study are also subject to the grain size of the pyrite sample used in each experiment.

Fig. 2-4 shows a good agreement between the reaction rate predicted by the proposed rate model and the reaction rate data in Jerz and Rimstidt (2004) for pyrite oxidation in moist air. The estimated water saturation is 0.11% which is the same as the dry condition case (0.1% saturation) in León et al. (2004); the diffusion coefficient is fitted as 1.2×10^{-18} $m^2 \cdot s^{-1}$ which is also close to that determined by León et al. (2004) (4.9×10^{-19} $m^2 \cdot s^{-1}$). This indicates that the resistance of the oxygen diffusion barrier in the two cases is at the same level despite the

difference in the reaction pH. In León et al. (2004), the pH is around 8.6 before and after the reaction, providing a favourable environment for the formation of iron oxyhydroxide coating on the pyrite surface. This iron oxyhydroxide coating, together with other precipitated soluble reaction products (e.g. ferric (hydroxy) sulphate according to Todd et al. (2003)) due to super-saturation, prohibits the diffusion of oxygen to the pyrite surface and, as a consequence, the reaction rate decreases as the coating grows with time. In Jerz and Rimstidt (2004), although the pH value was not given, the authors implied an acidic pH after the reaction and suggested that the diffusion barrier for pyrite oxidation in moist air was an acid solution film with dissolved reaction products (ferrous sulphate). In addition, they observed some iron sulphate salts on the surface of dried grains, indicating that some soluble reaction products may have precipitated in the solution film due to super saturation. In their case, the precipitations, together with the acidic solution film, form the diffusion barrier on the pyrite surface which has a diffusion coefficient comparable with that determined using data from León et al. (2004) with an iron hydroxide coating formed in a circum-neutral and high pH environment. It appears that, under semi-arid conditions, the reaction rate of prolonged pyrite oxidation is dominantly controlled by the water condition, which leads to the precipitation of oxidation products regardless of the pH value. Accordingly, the present rate model initially proposed for circum-neutral to alkaline pH may also be applicable to acidic semi-arid conditions.

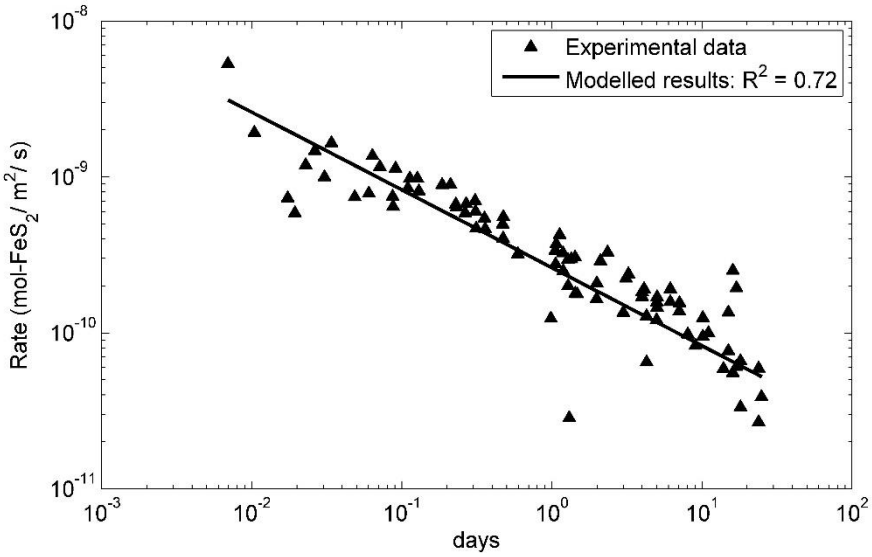

Fig. 2-4: Comparison of the modelled results in the present study and the experimental data in Jerz and Rimstidt (2004); the best fit yields a water saturation of 0.11%

2.3.2 Estimated activation energy

The measured activation energy, E_a, for pyrite oxidation varies from one study to another, but on average, most measurements lie within the range of 50 to 65 KJ·mol^{-1} for temperatures from 20°C to 45°C. Smith (1970) measured the rate of aqueous pyrite oxidation under different temperatures and an E_a of 64 KJ·mol^{-1} was obtained from the reported oxidation rate. McKibben and Barnes (1986) measured the activation energy for a temperature range

of 20°C to 40°C and reported a value of 56.9 KJ·mol^{-1}. Schoonen et al. (2000) measured the activation energy of pyrite oxidation within a pH range of 2 to 6 by increasing the temperature in steps from 23°C to 46.3°C during reactions. They found that the activation energies can vary by as much as 40 KJ·mol^{-1} with different reaction progress variables and depending on the pH value. Nevertheless, the activation energy averaged over the pH range is from 50 to 64 KJ·mol^{-1} depending on the reaction progress variable. In an electrochemical study in Chiriță and Schlegel (2017), the activation energy for pyrite oxidation was measured for a pH range of 1 to 5 within a temperature range of 25°C to 40°C; the reported E_a varies from 19.1 to 56.8 KJ·mol^{-1}. Nicholson et al. (1988) determined the activation energy for a temperature range of 3°C to 25°C and a value of 88 KJ·mol^{-1} was obtained which is higher than the E_a reported in the other studies mentioned above. At 60°C, the magnitude of the reaction rate is less than would be expected for this activation energy which suggests a much smaller activation energy near a temperature of 60°C. The comparison of activation energy reported in Nicholson et al. (1988) and the other studies mentioned above implies that the measured activation energy for pyrite oxidation gradually decreases with increasing temperature.

Nicholson et al. (1988) suggest that the variation in measured activation energy as temperature increases is due to a change in the relative controlling mechanism from surface reaction to oxygen diffusion. In other words, temperature affects both the surface reaction and the diffusion of oxygen through the diffusion barrier and therefore the measured activation energy will be closer to that of the rate-controlling mechanism (surface reaction or diffusion). According to this explanation, the activation energy for pyrite oxidation for different temperature ranges is estimated using the rate model proposed in this study (a combination of Eq. (2-8), (2-14), (2-15), (2-16) and (2-18)) to investigate the effect of temperature.

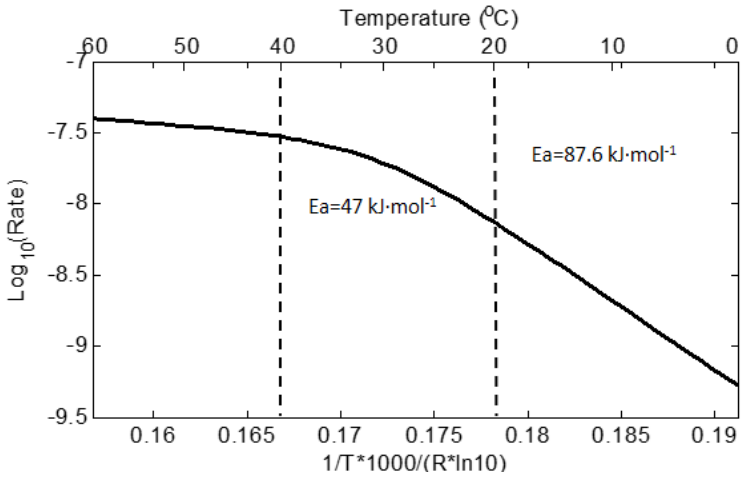

Fig. 2-5: The modelled Arrhenius plot of initial reaction rate for pyrite oxidation

Fig. 2-5 shows the modelled Arrhenius plot for the initial oxidation rate of pyrite, where the activation energy of the reaction is the negative slope of the curve. The modelled apparent activation energy below 20 °C is 87.6 KJ·mol^{-1} and for temperature ranging from 20 to 40 °C, it drops to 47.0 KJ.mol^{-1}. These values are reasonably consistent with the experimental

observations in Nicholson et al. (1990), McKibben and Barnes (1986) and Schoonen et al. (2000) discussed above. However, the modelled activation energy is sensitive to both reaction time and the values of D_s^0 and k_0''. For reactions of long duration, the modelled E_a decreases rapidly with increasing reaction time and increases with slight decreases in k_0''. This sensitivity to reaction time and the value of both the reaction rate constant and the diffusion coefficient could be a reason for the discrepancy in the activation energy measured for pyrite oxidation in the literature.

2.3.3 Application of the proposed model

Given the proposed reaction rate model and the determined values of D_s and k'' for pyrite oxidation, it is possible to quantify the effect of other factors on the reaction rate in practical applications. Fig. 2-6 shows the oxidation rate measured at different times as affected by different factors. The effect of particle size is shown in Fig. 2-6 (a). The reaction rate per mass ($mol \cdot s^{-1} \cdot g^{-1}$) increases with total surface area and hence decreases with increasing particle size as, in theory, the reaction rate per surface area is independent of particle size and shape. Fig. 2-6 (b) to (d) show the reaction rate per surface area against oxygen partial pressure, degree of water saturation and temperature, the trend and variations of which are as expected.

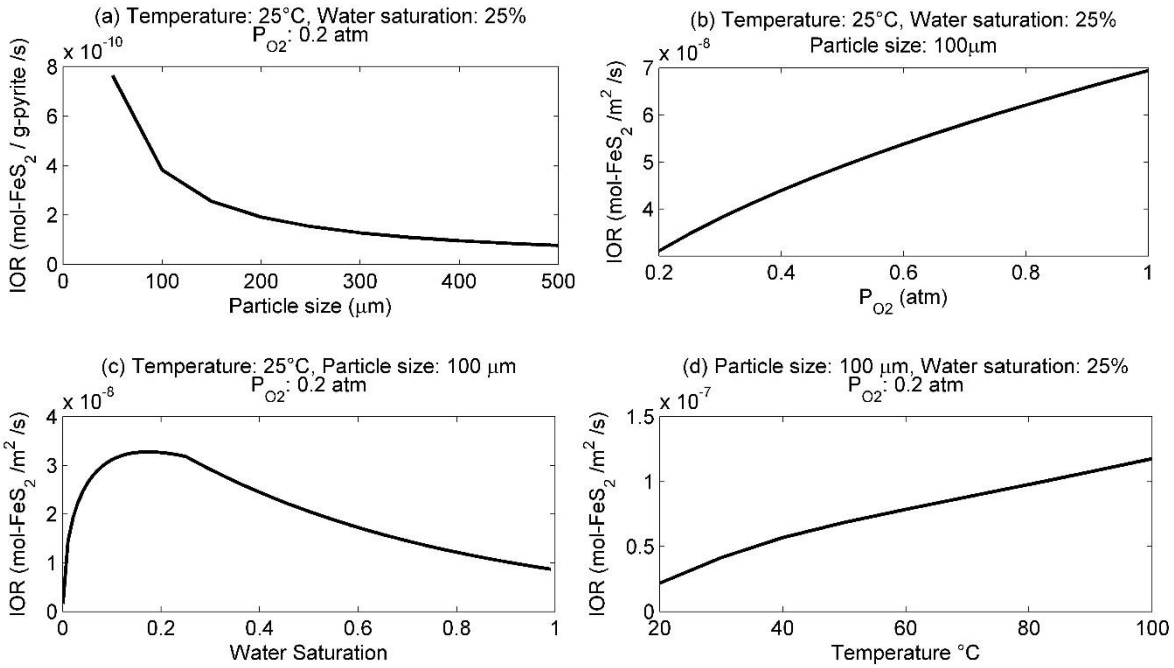

Fig. 2-6: The modelled initial oxidation rate (IOR) of pyrite with different: (a) particle sizes; (b) oxygen partial pressure; (c) water saturation; (d) temperature.

Fig. 2-7 shows the time required to achieve 50% of pyrite oxidation (half-conversion time) under different conditions predicted using the proposed reaction rate model. It shows that all four factors – pyrite grain size, oxygen partial pressure, temperature and water saturation – have significant impact on the reaction rate, especially water saturation. Under the optimal water condition of 25% saturation and a temperature of 25 °C, the time required to achieve

50% oxidation can be less than ten years with a maximum pyrite grain size of 30 μm and minimum oxygen partial pressure of 5% atm, which is a manageable period of time considering a typical mine life of a dozen years. A spontaneous rise in temperature due to the reaction could further shorten the time required to achieve an effective oxidation level for direct cyanidation.

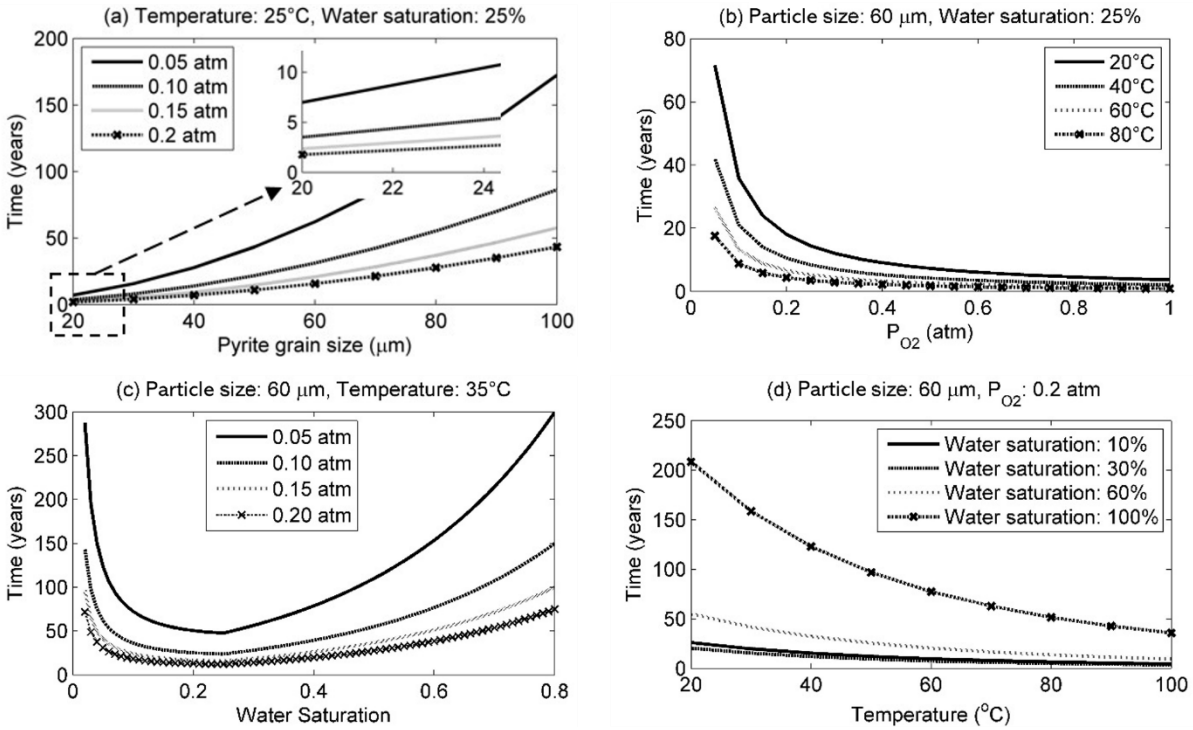

Fig. 2-7: The half conversion time for pyrite oxidation under different conditions: (a) The effect of particle size under various oxygen partial pressures at 25°C and 25% water saturation; (b) The effect of oxygen partial pressure under different temperatures at 25% water saturation and with particle size of 60 μm; (c) The effect of water saturation under various oxygen partial pressures at 25°C and with particle size of 60 μm; (d) The effect of temperature under various degrees of water saturation with particle sizes of 60 μm and 0.2 atm of oxygen partial pressure.

The proposed model is derived from the reaction rate of pure euhedral pyrite crystals at different grain sizes (see Table 2-4). In rock stockpiles, the pyrite oxidation process is also subject to the host rock particle size in addition to the factors discussed above. The majority of the pyrite-bearing rock in refractory gold ore stockpiles is boulder sized while the grain size of the contained pyrite is normally only in the range of microns to hundreds of microns with the grade commonly less than 10%. In this situation, pyrite oxidation will initially occur with pyrite grains on surfaces of the rock particles and gradually extends into the rock as oxygen and water slowly diffuse into the rock. The proposed model will be used in this framework to model the oxidation of pyrite grains contained in host rock particles. Research is currently underway to develop a stockpile pyrite oxidation model taking account of the practical considerations discussed above (e.g., rock particle sizes, pyrite grade and grain sizes) and the

stockpile geometries that affect oxygen and water/moisture concentration within stockpiles, based on the proposed model.

Note that the types of pyrite in an ore deposit may include framboidal and highly disordered pyrite which have a much higher reactivity due to their high specific surface area. Pugh et al. (1984) measured the effect of morphology on the rate of pyrite oxidation and the rates showed that, depending on the size fraction, oxidation of framboidal pyrite is 1.6 to 3.2 times faster than that of massive pyrite over 14 days of reaction. The results suggest that, at least at the initial stage of the reaction, framboidal pyrite is more reactive than massive pyrite. To model the pyrite oxidation in stockpiles properly, types of pyrite will also have to be considered. For example, as the proposed model is derived for euhedral pyrite, one simple approach of dealing with framboidal pyrite, or other types of pyrite with larger surface areas, is to scale up the reaction rate derived from the generic model or adjust the pyrite grain size in the present model according to the specific morphology.

2.3.4 Limitations of the proposed model

The proposed reaction rate law using the shrinking core model assumes invariant particle size during pyrite oxidation, which is not necessarily the case in reality because of the release of reaction product into the surrounding solution. In particular, at high water-saturation, the precipitated Fe product may only be a small percentage of the total Fe product (e.g. only 3% under submerged water condition according to Williamson and Rimstidt (1994)). Therefore, the precipitation layer on a fresh pyrite surface may, in reality, be much thinner than the theoretical one implied by the original shrinking core model. In the model proposed here, the layer between the original particle surface and the fresh pyrite surface is explained as a thin solution film that is highly saturated with oxidation products together with precipitations. Nevertheless, in predicting the pyrite oxidation rate, the possible deviation from reality is compensated by the diffusion coefficient, as it is a fitted value derived directly from experimental data.

The applicability of the proposed model is limited to certain pH environments. For high water-saturation conditions, the proposed model is only applicable for neutral or higher pH environments. For cases where the pH value is less than 4, the oxidation products would all be dissolved with sufficient water content and no precipitations would be formed. In these cases, the reaction process would no longer be within the scope of the proposed model and appropriate rate laws listed in Table 2-1 should be used for the oxidation rate where needed. At low water saturation, this model may be applied for both acidic and alkaline pH because a diffusion barrier can be formed by precipitation of the soluble reaction products due to super-saturation.

2.4 Conclusions

Natural oxidation of pyrite has the potential to contribute significantly to recovering gold from long-term stockpiled, low-grade refractory gold bearing material that otherwise may not be economically recoverable. Assessing the economic value of the partially oxidised material is

of interest to many gold mining companies that have stockpiled a large amount of this low-grade material. The key information required for this evaluation is the estimated level of pyrite oxidation in the stockpiles, which in turn requires pyrite oxidation rates under various conditions within the rock stockpiles, including temperature and water saturation. To this end, this paper proposes a reaction rate model for predicting pyrite oxidation that incorporates the influences of temperature, oxygen concentration and water saturation. The rate model is given as the rate of pyrite destruction and the rate of unreacted core shrinkage:

$$\begin{cases} (a) \quad -\dfrac{dN}{dt} = \dfrac{4\pi R^2 b C_e}{\dfrac{R}{D_s}\left(\dfrac{R}{r_c}-1\right)+\dfrac{1}{k''}\dfrac{R^2}{r_c^2}C_e^{0.5}} \\ (b) \quad -\dfrac{dr_c}{dt} = \dfrac{bC/\rho_B}{\dfrac{(R-r_c)r_c}{RD_s}+\dfrac{C^{0.5}}{k''}} \end{cases}$$

$$\begin{cases} C_e = C_g \cdot e^{\log\left(H^{cc}\right)\cdot\theta_w} \\ D_s = D_s^0 \cdot e^{\frac{-E_a^D}{R}\left(\frac{1}{T}-\frac{1}{T_0}\right)} \\ k'' = k_0'' \cdot e^{\frac{-E_a^k}{R}\left(\frac{1}{T}-\frac{1}{T_0}\right)} \end{cases} \tag{2-19}$$

For T_0 = 293.15 K:

$$\begin{cases} D_s^0 = 1.2 \times 10^{-15} & (for\ \theta_w \geq 25\%) \\ D_s^0 = 4.82 \times 10^{-15} \cdot \theta_w - 4.35 \times 10^{-18} & (for\ 0.1\% \leq \theta_w < 25\%) \\ k_0'' = 5 \times 10^{-8} \\ H^{cc} = 0.0353 \end{cases}$$

This model is based on the hypothesis that a diffusion barrier is formed around fresh pyrite particles in the reaction, which prohibits the diffusion of oxygen to the pyrite surface; it grows as the reaction proceeds and accounts for the decrease in the reaction rate over time. Depending on the pH and water conditions, the diffusion barrier may consist of solid oxidation products/precipitations and a thin solution film with dissolved reaction products. The corresponding diffusion coefficient is a function of temperature and water saturation. In this model, the effective oxygen concentration is used to represent the oxygen concentration at the particle surface as affected by the degree of water saturation. The relationship between effective oxygen concentration and water saturation is exponential. The parameters determined in this study for the proposed model, including both the surface reaction rate constant and the diffusion coefficient, are based on experimental data reported in the literature. For the diffusion coefficient, the determined value and the relationship with water saturation provide a reference for other studies where gas diffusion in reaction is important. The oxidation rate predicted by this model is consistent with the reported data from various studies. Hence, this model is able to predict the time-dependent reaction rate of prolonged pyrite oxidation at circum-neutral to alkaline pH under various temperatures and levels of water saturation. Using this model, and other rate models that consider different reaction

conditions, it is possible to predict the oxidation level of pyrite in refractory gold bearing rock stockpiles.

Appendix 2.A Derivation of the modified shrinking core model

According to Levenspiel (1999), the rate of reaction of a gaseous reactant A, oxygen in this study, at any instant, is equal to its rate of diffusion to the reaction surface:

$$-\frac{dN_A}{dt} = 4\pi r^2 Q_A = 4\pi R^2 Q_{As} = 4\pi r_c^2 Q_{Ac} \quad \text{(2-A1)}$$

where $-\frac{dN_A}{dt}$ is the oxygen consumption rate, R is the initial radius of the pyrite particle, r_c is the radius of the unreacted core, and r is any radius between r_c and R; Q_{As}, Q_{Ac} and Q_A are the oxygen flux at the particle surface, reacting front and the layer with radius of r within the oxidised layer respectively.

The oxygen flux, Q_A, depends on the diffusion coefficient within the oxidised layer (D_s) and the gradient of oxygen concentration (C_A):

$$Q_A = D_s \frac{dC_A}{dr} \quad \text{(2-A2)}$$

The oxygen flux at the reacting front Q_{Ac} is given by the reaction rate of oxygen at the reacting front and thus depends on the surface reaction kinetics. For half-order surface reaction:

$$Q_{Ac} = k'' C_{Ac}^{0.5} \quad \text{(2-A3)}$$

where C_{Ac} is the oxygen concentration at the reacting front and k'' is the half-order reaction rate constant. Substituting Eqs. (2-A2) and (2-A3) into Eq. (2-A1) gives:

$$-\frac{dN_A}{dt} = 4\pi r^2 D_s \frac{dC_A}{dr} = 4\pi r_c^2 k'' C_{Ac}^{0.5} \quad \text{(2-A4)}$$

Eq. (2-A4) can be rewritten as:

$$D_s \cdot dC_A = k'' r_c^2 C_{Ac}^{0.5} \cdot \frac{dr}{r^2} \quad \text{(2-A5)}$$

Integrating both sides across the oxidised layer:

$$D_s \cdot \int_{C_{As}}^{C_{Ac}} dC_A = k'' r_c^2 C_{Ac}^{0.5} \cdot \int_R^{r_c} \frac{dr}{r^2} \tag{2-A6}$$

$$D_s \cdot (C_{Ac} - C_{As}) = k'' r_c^2 C_{Ac}^{0.5} \cdot (\frac{1}{R} - \frac{1}{r_c}) \tag{2-A7}$$

The oxygen concentration at the reacting front can be obtained by solving Eq. (2-A7) for $C_{Ac}^{0.5}$:

$$C_{Ac}^{0.5} = -\frac{k'' r_c^2}{2D_s}\left(\frac{1}{r_c} - \frac{1}{R}\right) + \sqrt{\left[\frac{k'' r_c^2}{2D_s}\left(\frac{1}{r_c} - \frac{1}{R}\right)\right]^2 + C_{As}} \tag{2-A8}$$

Let

$$w = \frac{k'' r_c^2}{2D_s C_{As}^{0.5}}\left(\frac{1}{r_c} - \frac{1}{R}\right) \tag{2-A9}$$

and from Eq. (2-A1), the oxygen consumption rate is given as:

$$-\frac{dN_A}{dt} = 4\pi r_c^2 k'' C_{Ac}^{0.5} = 4\pi r_c^2 k''\left(\sqrt{(wC_{As}^{0.5})^2 + C_{As}} - wC_{As}^{0.5}\right) \tag{2-A10}$$

Eq. (2-A10) can be transformed as:

$$\begin{aligned} -\frac{dN_A}{dt} = 4\pi r_c^2 k'' C_{Ac}^{0.5} &= \frac{4\pi R^2 C_{As}}{\frac{R^2 C_{As}^{0.5}}{r_c^2 k''} \cdot \frac{C_{As}^{0.5}}{\sqrt{(wC_{As}^{0.5})^2 + C_{As}} - wC_{As}^{0.5}}} \\ &= \frac{4\pi R^2 C_{As}}{\frac{R^2 C_{As}^{0.5}}{r_c^2 k''} \cdot \frac{C_{As}^{0.5}(\sqrt{(wC_{As}^{0.5})^2 + C_{As}} + wC_{As}^{0.5})}{C_{As}}} = \frac{4\pi R^2 C_{As}}{\frac{R^2 C_{As}^{0.5}}{r_c^2 k''} \cdot (\sqrt{w^2+1} + w)} \end{aligned} \tag{2-A11}$$

Note that,

$$\sqrt{w^2+1} + w = 2w + 1 + (\sqrt{w^2+1} - \sqrt{w^2+2w+1}) \approx 2w + 1 \tag{2-A12}$$

and therefore, Eq. (2-A11) can be approximated as:

$$-\frac{dN_A}{dt}=\frac{4\pi R^2 C_{As}}{\frac{R^2 C_{As}^{0.5}}{r_c^2 k''}\cdot(2w+1)}=\frac{4\pi R^2 C_{As}}{\frac{R^2 C_{As}^{0.5}}{r_c^2 k''}+\frac{R^2}{D_s}\left(\frac{1}{r_c}-\frac{1}{R}\right)}=\frac{4\pi R^2 C_{As}}{\frac{R}{D_s}\left(\frac{R}{r_c}-1\right)+\frac{1}{k''}\frac{R^2}{r_c^2}C_{As}^{0.5}} \quad \text{(2-A13)}$$

The reaction rate of pyrite is given by the stoichiometry between pyrite and oxygen:

$$-\frac{dN_B}{dt}=-\frac{b\cdot dN_A}{dt}=4\pi r_c^2\cdot\rho_B\cdot\frac{dr_c}{dt} \quad \text{(2-A14)}$$

where b is the stoichiometric coefficient. Substituting Eq. (2-A13) into Eq. (2-A14), we have:

$$\frac{dr_c}{dt}=\frac{bC_{As}/\rho_B}{\frac{r_c}{D_s}\left(1-\frac{r_c}{R}\right)+\frac{1}{k''}C_{As}^{0.5}} \quad \text{(2-A15)}$$

Eqs. (2-A13) and (2-A15) are the governing equations of the modified shrinking core model.

Acknowledgement

This research was financially supported by Newcrest Mining Limited.

References

Ardejani, FD, Malakooti, SJ, Shafaei, SZ & Shahhosseini, M 2014, 'A numerical multi-component reactive model for pyrite oxidation and pollutant transportation in a pyritic, carbonate-rich coal waste pile in northern Iran', *Mine Water and the Environment*, vol. 33, no. 2, pp. 121-132.

Chiriță, P & Schlegel, ML 2017, 'Pyrite oxidation in air-equilibrated solutions: An electrochemical study', *Chemical Geology*, vol. 470, 2017/10/20/, pp. 67-74.

Elberling, B, Nicholson, RV & Scharer, JM 1994, 'A combined kinetic and diffusion model for pyrite oxidation in tailings: a change in controls with time', *Journal of Hydrology*, vol. 157, no. 1–4, pp. 47-60.

Elberling, B, Schippers, A & Sand, W 2000, 'Bacterial and chemical oxidation of pyritic mine tailings at low temperatures', *Journal of Contaminant Hydrology*, vol. 41, no. 3–4, pp. 225-238.

Evangelou, VP & Zhang, YL 1995, 'A review: Pyrite oxidation mechanisms and acid mine drainage prevention', *Critical Reviews in Environmental Science and Technology*, vol. 25, no. 2, 1995/05/01, pp. 141-199.

Gleisner, M, Herbert, RB & Kockum, PCF 2006, 'Pyrite oxidation by Acidithiobacillus ferrooxidans at various concentrations of dissolved oxygen', *Chemical Geology*, vol. 225, no. 1, pp. 16-29.

Holmes, PR & Crundwell, FK 2000, 'The kinetics of the oxidation of pyrite by ferric ions and dissolved oxygen: an electrochemical study', *Geochimica et Cosmochimica Acta*, vol. 64, pp. 263-274.

Huminicki, DMC & Rimstidt, JD 2009, 'Iron oxyhydroxide coating of pyrite for acid mine drainage control', *Applied Geochemistry*, vol. 24, no. 9, 2009/09/01/, pp. 1626-1634.

Jerz, JK & Rimstidt, JD 2004, 'Pyrite oxidation in moist air1', *Geochimica et Cosmochimica Acta*, vol. 68, no. 4, 2/15/, pp. 701-714.

Kameia, G & Ohmotob, H 2000, 'The kinetics of reactions between pyrite and O2-bearing water revealed from in situ monitoring of DO, Eh and pH in a closed system', *Geochimica et Cosmochimica Acta*, vol. 64, pp. 2585-2601.

Karikari-Yeboah, O, Skinner, W & Addai-Mensah, J 2018, 'The impact of preload on the mobilisation of multivalent trace metals in pyrite-rich sediment', *Environmental Monitoring and Assessment*, vol. 190, p. 398.

Ketcham, VJ, O'Reilly, JF & Vardill, WD 1993, 'The lihir gold project; Process plant design', *Minerals Engineering*, vol. 6, pp. 1037-1065.

La Brooy, SR, Linge, HG & Walker, GS 1994, 'Review of gold extraction from ores', *Minerals Engineering*, vol. 7, no. 10, 1994/10/01, pp. 1213-1241.

Lasaga, AC 1984, 'Chemical kinetics of water-rock interactions', *Journal of Geophysical Research: Solid Earth*, vol. 89, pp. 4009-4025.

Lefebvre, R, Hockley, D, Smolensky, J & Lamontagne, A 2001, 'Multiphase transfer processes in waste rock piles producing acid mine drainage: 2. Applications of numerical simulation', *Journal of Contaminant Hydrology*, vol. 52, pp. 165-186.

León, EA, Rate, A, Hinz, C & Campbell, G 2004, 'Weathering of sulphide minerals at circum-neutral-pH in semi-arid/arid environments: Influence of water content', in *Proc., SuperSoil 2004: 3rd Australian New Zealand Soils Conf*.

Levenspiel, O 1972, 'Chemical reaction engineering', Wiley Eastern Limited.

Levenspiel, O 1999, 'Chemical reaction engineering', *Industrial & engineering chemistry research*, vol. 38, no. 11, pp. 4140-4143.

McKibben, MA & Barnes, HL 1986, 'Oxidation of pyrite in low temperature acidic solutions: Rate laws and surface textures', *Geochimica et Cosmochimica Acta*, vol. 50, no. 7, pp. 1509-1520.

Molson, JW, Fala, O, Aubertin, M & Bussière, B 2005, 'Numerical simulations of pyrite oxidation and acid mine drainage in unsaturated waste rock piles', *Journal of Contaminant Hydrology*, vol. 78, no. 4, pp. 343-371.

Moses, CO & Herman, JS 1991, 'Pyrite oxidation at circumneutral pH', *Geochimica et Cosmochimica Acta*, vol. 55, no. 2, 1991/02/01, pp. 471-482.

Nicholson, RV, Gillham, RW & Reardon, EJ 1988, 'Pyrite oxidation in carbonate-buffered solution: 1. Experimental kinetics', *Geochimica et Cosmochimica Acta*, vol. 52, no. 5, 1988/05/01, pp. 1077-1085.

Nicholson, RV, Gillham, RW & Reardon, EJ 1990, 'Pyrite oxidation in carbonate-buffered solution: 2. Rate control by oxide coatings', *Geochimica et Cosmochimica Acta*, vol. 54, pp. 395-402.

Olson, GJ 1991, 'Rate of pyrite bioleaching by Thiobacillus ferrooxidans: results of an interlaboratory comparison', *Applied and environmental microbiology*, vol. 57, pp. 642-644.

Pesic, B, Oliver, DJ & Wichlacz, P 1989, 'An electrochemical method of measuring the oxidation rate of ferrous to ferric iron with oxygen in the presence of Thiobacillus ferrooxidans', *Biotechnology and Bioengineering*, vol. 33, pp. 428-439.

Pugh, C, Hossner, L & Dixon, J 1984, 'Oxidation rate of iron sulfides as affected by surface area, morphology, oxygen concentration, and autotrophic bacteria', *Soil Science*, vol. 137, no. 5, pp. 309-314.

Qiu, G, Luo, Y, Chen, C, Lv, Q, Tan, W, Liu, F & Liu, C 2016, 'Influence factors for the oxidation of pyrite by oxygen and birnessite in aqueous systems', *Journal of Environmental Sciences*, vol. 45, pp. 164-176.

Schoonen, M, Elsetinow, A, Borda, M & Strongin, D 2000, 'Effect of temperature and illumination on pyrite oxidation between pH 2 and 6', *Geochemical Transactions*, vol. 1, no. 4, p. 23.

Singer, PC & Stumm, W 1970, 'Acidic mine drainage: the rate-determining step', *Science*, vol. 167, no. 3921, pp. 1121-1123.

Smith, EE 1970, 'Sulfide to sulfate reaction mechanism : a study of the sulfide to sulfate reaction mechanism as it relates to the formation of acid mine waters'.

Szekely, J, Evans, JW & Sohn, HY 1976, 'Gas-solid reactions'.

Tabelin, CB, Igarashi, T, Villacorte-Tabelin, M, Park, I, Opiso, EM, Ito, M & Hiroyoshi, N 2018, 'Arsenic, selenium, boron, lead, cadmium, copper, and zinc in naturally contaminated rocks: A review of their sources, modes of enrichment, mechanisms of release, and mitigation strategies', *Science of The Total Environment*, vol. 645, 2018/12/15/, pp. 1522-1553.

Tabelin, CB, Veerawattananun, S, Ito, M, Hiroyoshi, N & Igarashi, T 2017, 'Pyrite oxidation in the presence of hematite and alumina: I. Batch leaching experiments and kinetic modeling calculations', *Science of The Total Environment*, vol. 580, pp. 687-698.

Tamoto, S, Tabelin, CB, Igarashi, T, Ito, M & Hiroyoshi, N 2015, 'Short and long term release mechanisms of arsenic, selenium and boron from a tunnel-excavated sedimentary rock under in situ conditions', *Journal of Contaminant Hydrology*, vol. 175-176, pp. 60-71.

Todd, E, Sherman, D & Purton, J 2003, 'Surface oxidation of pyrite under ambient atmospheric and aqueous (pH= 2 to 10) conditions: electronic structure and mineralogy from X-ray absorption spectroscopy', *Geochimica et Cosmochimica Acta*, vol. 67, no. 5, pp. 881-893.

Welch, VS, Dann, MW & Mehta, B 1990, 'Predicting Oxygen Depletion in Reservoir Environments', *SPE Annual Technical Conference and Exhibition*, Society of Petroleum Engineers, New Orleans, Louisiana, p. 12, DOI: 10.2118/20721-MS.

Williamson, MA, Kirby, CS & Rimstidt, JD 2006, 'Iron dynamics in acid mine drainage', in RI Barnhisel (ed.), *International Conference on Acid Rock Drainage (ICARD)*, American Society of Mining and Reclamation (ASMR), St. Louis MO, DOI: 10.21000/JASMR06022411.

Williamson, MA & Rimstidt, JD 1994, 'The kinetics and electrochemical rate-determining step of aqueous pyrite oxidation', *Geochimica et Cosmochimica Acta*, vol. 58, no. 24, pp. 5443-5454.

Wunderly, M, Blowes, D, Frind, E & Ptacek, C 1996, 'Sulfide mineral oxidation and subsequent reactive transport of oxidation products in mine tailings impoundments: A numerical model', *Water Resources Research*, vol. 32, no. 10, pp. 3173-3187.

Xu, T, White, S, Pruess, K & Brimhall, G 2000, 'Modeling of Pyrite Oxidation in Saturated and Unsaturated Subsurface Flow Systems', *Transport in Porous Media*, vol. 39, pp. 25-56.

Yagi, S & Kunii, D 1955, 'Studies on combustion of carbon particles in flames and fluidized beds', *Symposium (International) on Combustion*, vol. 5, pp. 231-244.

Yagi, S & Kunii, D 1961, 'Fluidized-solids reactors with continuous solids feed—I: Residence time of particles in fluidized beds', *Chemical Engineering Science*, vol. 16, pp. 364-371.

Yu, J-Y, McGenity, TJ & Coleman, ML 2001, 'Solution chemistry during the lag phase and exponential phase of pyrite oxidation by Thiobacillus ferrooxidans', *Chemical Geology*, vol. 175, pp. 307-317.

Chapter 3

Modelling the pyrite oxidation level in a refractory gold-bearing stockpile to assess its potential for gold recovery by direct cyanide leaching

Statement of Authorship

Title of Paper	Modelling the pyrite oxidation level in a refractory gold-bearing stockpile to assess its potential for gold recovery by direct cyanide leaching
Publication Status	☐ Published ☐ Accepted for Publication ☑ Submitted for Publication ☐ Unpublished and Unsubmitted w ork w ritten in manuscript style
Publication Details	Updates: Accepted for Publication on 21 July 2021 Wang, H., Xu, C. and Dowd, P.A. 2021 'Modelling the pyrite oxidation level in a refractory gold-bearing stockpile to assess its potential for gold recovery by direct cyanide leaching', *Minerals Engineering,* vol. 171, 2021/09/01/, p. 107089.

Principal Author

Name of Principal Author (Candidate)	Hang Wang		
Contribution to the Paper	Model development, simulation, results analysis and manuscript drafting.		
Overall percentage (%)	70%		
Certification:	This paper reports on original research I conducted during the period of my Higher Degree by Research candidature and is not subject to any obligations or contractual agreements with a third party that would constrain its inclusion in this thesis. I am the primary author of this paper.		
Signature		Date	07/04/2021

Co-Author Contributions

By signing the Statement of Authorship, each author certifies that:

i. the candidate's stated contribution to the publication is accurate (as detailed above);

ii. permission is granted for the candidate in include the publication in the thesis; and

iii. the sum of all co-author contributions is equal to 100% less the candidate's stated contribution.

Name of Co-Author	Chaoshui Xu		
Contribution to the Paper	Supervision, design of the work and reviewing the manuscript.		
Signature		Date	8-4-2021

Name of Co-Author	Peter A. Dowd		
Contribution to the Paper	Supervision, design of the work and reviewing the manuscript.		
Signature		Date	09/04/2021

Please cut and paste additional co-author panels here as required.

Abstract

This study presents a three-dimensional numerical modelling method for predicting the pyrite oxidation level in refractory gold-bearing stockpiles under various conditions. The physical and chemical processes incorporated into the model include oxygen transport, heat transfer, air convection and pyrite oxidation. Different reaction rate models based on the shrinking core model are used to quantify the oxidation of pyrite grains in rock particles considering the influence of oxygen concentration, degree of water saturation, temperature and pH conditions. The oxygen concentration gradient within rock particles is considered for pyrite oxidation and is solved using the diffusion-reaction equation in the polar-coordinate system. Particle size distributions for both pyrite grains and rock particles are incorporated in the modelling of pyrite oxidation and oxygen consumption. Several scenarios with different parameters were examined and the simulation results show that after ten years, the pyrite oxidation level over the stockpile is up to 50% depending on the location within the stockpile, the rock types and stockpile properties such as porosity and water content. The model can simulate the overall pyrite oxidation level as well as the oxidation profile of the pyrite grains, i.e., the oxidation depth of pyrite grains of different sizes and at different locations within the rock particles. These are essential inputs required for the estimation of gold recovery by direct cyanide leaching for possible reclamation of the partially oxidised stockpile without incurring expensive pre-treatment of the material.

3.1 Introduction

The most common gold-bearing minerals in refractory gold ore deposits are sulphides, which must be pre-treated prior to cyanidation by pressure oxidation (POX), bio-oxidation, roasting or ultrafine grinding in order to separate the gold particles from the host sulphide minerals. However, when these sulphides are exposed to air and water for an extensive period of time, pyrite may be naturally oxidised, which may reduce the need for pre-treatment and hence reduce the processing cost. This may occur in long-term stockpiles of low-grade gold-bearing material in many refractory gold mining operations. This low-grade material (below the prevailing economic cut-off grade) may have been mined to access ore or may have resulted from limited mining selectivity, and it is commonly stockpiled for potential processing at a later stage of the mine life. It may also consist of low-grade ore that is stockpiled to give priority to processing higher-grade ores. Oxidised material can be directly leached to extract the contained gold without expensive pre-treatment. Hence the natural oxidation of pyrite in refractory gold-bearing stockpiles may increase the profitability of stockpile reclamation by enabling gold recovery using direct cyanide leaching. In this context, it is essential to understand the level of the natural oxidation of pyrite within the stockpile in order to evaluate the potential for recovering the gold without pre-treatment.

Natural oxidation of pyrite has been studied extensively because of its negative impact on the environment. When exposed to water and oxygen, pyrite can be oxidised to release sulphate, iron ions and acid. The resulting effluent is acidic and can dissolve metals and elements that can be toxic to local flora and fauna if discharged into the local groundwater system; this process is referred to as acid rock drainage (ARD). Research on the natural oxidation of pyrite, including both laboratory studies and numerical modelling, has largely focused on ARD, with the aims of determining the rate-controlling factors and predicting the effluent discharge for control and remediation. The oxidation reaction in these cases is often associated with low-pH and intro-aqueous conditions. Pyrite oxidation can also occur in non-acidic conditions and under different water contents, with different rates of reaction depending on conditions (Huminicki and Rimstidt, 2009; León et al., 2004; Moses and Herman, 1991; Nicholson et al., 1988). Prediction of the oxidation level of pyrite in stockpiles requires consideration of the various reaction conditions that affect the oxidation rate.

Oxygen availability is widely recognised as the most important among all the factors that affect the pyrite oxidation rate in mine tailings and rock piles. Oxygen, as one of the reactants, needs to be replenished constantly from the atmosphere into the stockpile to sustain the reaction. The oxygen can be replenished via diffusion and/or advection. The diffusion rate depends on the stockpile properties including porosity and water content. The water content in the stockpile generally inhibits the oxygen transport as oxygen diffuses much slower in water than in air. Both laboratory studies (León et al., 2004) and field observations (Elberling et al., 2000) have found that partially saturated conditions are the most favourable for pyrite oxidation. In addition to diffusion, as pyrite oxidation is exothermic, thermal-induced air convection may also be an effective source of oxygen resupply. The heat generated from the reaction raises the temperature of the stockpile, which may induce air movement between

the stockpile and the atmosphere. The increased temperature will also directly affect the oxidation rate, as documented in Chiriță and Schlegel (2017), Schoonen et al. (2000) and McKibben and Barnes (1986). Other factors, such as particle size distribution, mineral composition and the shape and size of the stockpile, also affect pyrite oxidation by influencing the water flow, oxygen transport and the pH environment. As the effects of these factors on pyrite oxidation are mostly non-linear and interdependent, a coupled numerical modelling approach is required to predict the pyrite oxidation level in stockpiles.

Many numerical modelling tools have been developed to simulate pyrite oxidation as well as the related physical and geochemical processes for ore leaching and AMD prediction. Early modelling work can be found in Cathles and Apps (1975), Jaynes et al. (1984), Davis and Ritchie (1986), Pantelis (1993), Elberling et al. (1994), Wunderly et al. (1996) and Gerke et al. (1998). The work reported in these papers has contributed to the development of more advanced models, including TOUGH AMD (Lefebvre et al., 2001), SULFIDOX (Brown et al., 1999), MIN3P (Mayer et al., 2002; Pabst et al., 2017), POLYMIN (Molson et al., 2005) and THERMOX (da Silva et al., 2009).

Cathles and Apps (1975) developed a one-dimensional, non-steady-state model for sulphide mineral oxidation in the leaching process of a copper waste dump. Their model assumed air convection to be the dominant transport mechanism for oxygen and considered heat generation and bacteria catalysis on ferrous ion oxidation. Pyrite oxidation was modelled using the shrinking core model (Levenspiel, 1999) with a constant surface reaction rate independent of oxygen concentration. Jaynes et al. (1984) presented a variation of the model from Cathles and Apps (1975) to study acid mine drainage from a reclaimed coal strip mine. Their model assumed gaseous diffusion to be the dominant mechanism for oxygen transport. They also simulated the removal of reaction products with water percolation.

Wunderly et al. (1996) developed a one-dimensional numerical model (PYROX) based on the work of Davis and Ritchie (1986) to simulate the oxidation of pyrite in the vadose zone of mine tailings. In the PYROX model, the bulk diffusion coefficient of oxygen is spatially variable depending on the moisture content, porosity and temperature. They also coupled the PYROX model with the existing reactive transport model MINTRAN developed by Walter et al. (1994) to create the MINTOX model for simulating both pyrite oxidation and the subsequent transport of oxidation products in mine tailing impoundments. A similar approach was taken by Gerke et al. (1998), in which a 2D pyrite oxidation model was added to the MINTRAN model. The heterogeneity of hydraulic conductivity and sulphide mineral fractions were incorporated to provide a better means of simulating the concentration of oxidation products in the effluent at the local scale. Molson et al. (2005) derived a model (POLYMIN) from the work of Gerke et al. (1998) for acid mine drainage simulation and studied the effects of the interior structure of the waste rock pile on the flow path of acid mine drainage. Their model incorporates oxygen diffusion, kinetic (diffusion-limited) sulphide oxidation, multi-component advective-dispersive transport and geochemical reactions. The water content in their model was simulated using HYDRUS-2D (Simunek et al., 1999).

Lefebvre et al. (2001) simulated acid mine drainage from waste rock piles using TOUGH AMD developed by Lefebvre (1995). The model was based on TOUGH2 which was first presented by Pruess (1991). Their model considered oxygen advection and diffusion, heat transfer, pyrite oxidation and sulphate transport with water infiltration and liquid flow. Pyrite oxidation was modelled using kinetic and geometric factors to represent the effects on the volumetric oxidation rate of temperature, oxygen partial density and the proportion of remaining pyrite. These factors provide kinetic control for the reaction to avoid the modelling difficulty in extreme cases such as the total absence of oxygen from the system.

Brown et al. (1999) and Pantelis et al. (2002) provided the SULFIDOX software package, which evolved from FIDHELM (Pantelis, 1993), to model air and water flow, chemical reactions and reactive transport in waste rock piles including dissolution and precipitation of minerals. They used the Monod model, the bilinear model or a combination of the two to describe the reaction rate of sulphide oxidation Pantelis et al. (2002). Another comprehensive model, MIN3P, described in Mayer et al. (2002) incorporates a generalized formulation for kinetically controlled reactions into a multicomponent reactive transport model that can simulate intra-aqueous reactions, mineral dissolution and precipitation, as well as geochemical equilibrium processes. For pyrite oxidation, MIN3P uses the shrinking core model and assumes the reaction is controlled by oxygen diffusion. da Silva et al. (2009) provided a comprehensive ARD modelling program THERMOX, derived from HYDRUS-2D (Simunek et al., 1999) and PHREEQC (Parkhurst et al., 1980). This program can simulate oxygen transport by diffusion and advection, heat transfer, pyrite oxidation and geochemical reactions. In THERMOX, pyrite oxidation is modelled using the shrinking core model in the same way as used in Wunderly et al. (1996), Molson et al. (2005) and Mayer et al. (2002), which assumes diffusional control for the reaction in rock fragments.

To summarise, the processes considered in the modelling programs discussed above include oxygen transport by diffusion and/or convection, pyrite oxidation, heat transfer and reactive transports (fluid flow and geochemical reactions). In these models, pyrite oxidation is modelled by taking a whole rock fragment as the solid reactant and the reaction progress is represented either by the shrinking core model assuming diffusion of oxygen through the rock particle controls the reaction or simply by geometric/kinetic factors. The diffusion-controlled shrinking core modelling approach was used in most of these models (da Silva et al., 2009; Davis and Ritchie, 1986; Gerke et al., 1998; Mayer et al., 2002; Molson et al., 2005; Wunderly et al., 1996). This approach assumes that pyrite occurs in a very fine size and is homogeneously distributed within the rock particles; hence it reacts immediately in the presence of oxygen. Thus, the oxygen diffusion front inside the rock particle is the reacting front as well as the boundary that divides the rock particle into two parts: the completely altered rim and the unreacted core. This assumption simplifies the modelling of the reaction of pyrite inside rock particles and gives good approximations for the release rate of reaction products and the overall reaction progress, which is acceptable for ARD prediction. However, this assumption may not be realistic, especially when the grain size of pyrite inside the rock particles is significant and, hence, the reaction between pyrite grains and oxygen cannot be assumed to be immediate, and instead, may be at a rate comparable with oxygen diffusion

through the rock particles. In this case, the overall reaction progress is controlled by both the diffusion of oxygen within the rock particles and the chemical reaction at the pyrite grains.

The purpose of the research presented here differs from that of the ARD prediction models and is to develop a modelling tool that can effectively predict the distribution of different pyrite oxidation levels within a stockpile for the estimation of the gold recovery by direct cyanide leaching from refractory ore. The focus of the model presented in this paper is on the oxidation of pyrite grains within rock particles. We consider a more general case by using the diffusion-reaction equation to describe the oxidation of pyrite grains within a rock particle instead of using the diffusion-controlled shrinking core model. The benefit of using this more complex model is to allow a wider range of applications considering different material types with various rock diffusivities and particle size distributions for both rock particles and pyrite grains. The effects of temperature, water content, oxygen concentration, pH condition and particle size distributions are also incorporated in the modelling of pyrite oxidation. The processes that are interdependent with the reaction, including oxygen transport and heat transfer, are simulated. Other influencing factors such as water content are treated as pre-defined parameters in this model.

3.2 Mathematical model

3.2.1 Pyrite oxidation

The oxidation of pyrite by oxygen in the stockpile is generally described by the following stoichiometric equation:

$$2FeS_2 + 7O_2 + 2H_2O \rightarrow 2Fe^{2+} + 4{SO_4}^{2-} + 4H^+ \quad (3\text{-}1)$$

where pyrite is oxidised in the presence of oxygen and water.

In reality, pyrite oxidation may involve multiple reactions including oxygenation of ferrous ion that generates ferric ion, the oxidation of pyrite by ferric ion and the hydrolysis of ferric ion (Singer and Stumm, 1970); both oxygen and ferric ion are the oxidants for pyrite oxidation. The kinetics of this reaction is therefore complex as each individual intermediate step could be affected differently by reaction conditions. There are numerous published studies on the kinetics of pyrite oxidation with specific focus on the rate-controlling step of the reaction, e.g., see discussions and reviews in Williamson and Rimstidt (1994), Evangelou and Zhang (1995) and Chandra and Gerson (2010). Experimental studies show that the overall oxidation rate is affected by factors including the pH condition, oxygen concentration, temperature, water content and iron-oxidizing bacteria (Wang et al., 2019).

Under the theoretical framework of the shrinking core model, the abiotic oxidation of pure pyrite can be separated into two different cases depending on whether a diffusion barrier, such as an oxidised coating or a thin saturated solution film, develops on the fresh pyrite surface during the reaction. For cases where a diffusion barrier develops, Wang et al. (2019) proposed a reaction rate model for abiotic oxidation of pyrite grains based on empirical rate

data, which applies to circum-neutral to high pH and/or unsaturated water conditions. This reaction rate model is given in Eq. (3-2), where $-\frac{dN}{dt}$ is the pyrite destruction rate, b is the stoichiometric coefficient given by Eq. (3-1) as 2/7, ρ_B is the molar density of pyrite, R is the initial radius of pyrite particles, r_c is the radius of the unreacted core, D_s is the diffusion coefficient for oxygen through the oxidised layer of the pyrite grain which depends on the degree of water saturation S_w and temperature T; k'' is the reaction rate constant (in terms of oxygen) for the surface reaction and also depends on temperature T; C_e is the effective oxygen concentration which is given by the oxygen concentration in gas phase C_g and the degree of water saturation S_w; D_s^0 and k_0'' are the values of D_s and k'' at the reference temperature T_0 of 20°C; E_a^D and E_a^k are the activation energies for diffusion and surface reaction respectively; T is the reaction temperature in Kelvin; $\bar{R}$ is the gas constant and H^{cc} is the Henry's law solubility ($[O_2]_{water}/[O_2]_{air}$).

$$\begin{cases} (a) \quad -\dfrac{dN}{dt} = \dfrac{4\pi R^2 b C_e}{\dfrac{R}{D_s}\left(\dfrac{R}{r_c}-1\right)+\dfrac{1}{k''}\dfrac{R^2}{r_c^2}C_e^{0.5}} \\ (b) \quad -\dfrac{dr_c}{dt} = \dfrac{bC_e/\rho_B}{\dfrac{(R-r_c)r_c}{RD_s}+\dfrac{C_e^{0.5}}{k''}} \end{cases}$$

$$\begin{cases} C_e = C_g \cdot e^{log(H^{cc})\cdot S_w} \\ D_s = D_s^0 \cdot e^{\frac{-E_a^D}{\bar{R}}(\frac{1}{T}-\frac{1}{T_0})} \\ k'' = k_0'' \cdot e^{\frac{-E_a^k}{\bar{R}}(\frac{1}{T}-\frac{1}{T_0})} \end{cases} \tag{3-2}$$

For T_0 = 293.15 K:

$$\begin{cases} D_s^0 = 1.2 \times 10^{-15} & (for\ S_w \geq 25\%) \\ D_s^0 = 4.82 \times 10^{-15} \cdot \theta_w - 4.35 \times 10^{-18} & (for\ 0.1\% \leq S_w < 25\%) \\ k_0'' = 5 \times 10^{-8} \\ H^{cc} = 0.0353 \end{cases}$$

For cases where no diffusion barrier develops (under intro-aqueous acidic environment), expressions of (a) and (b) in Eq. (3-2) become those in Eq. (3-3) while other terms remain the same.

$$\begin{cases} (a) \quad -\dfrac{dN}{dt} = \dfrac{4\pi R^2 b C_e}{\dfrac{1}{k''}\dfrac{R^2}{r_c^2}C_e^{0.5}} \\ (b) \quad -\dfrac{dr_c}{dt} = \dfrac{bC_e/\rho_B}{\dfrac{C_e^{0.5}}{k''}} \end{cases} \tag{3-3}$$

Eqs. (3-2) and (3-3) give the reaction rate for pure pyrite grains. The oxidation of pyrite contained in rock particles will also depend on the diffusion of oxygen inside rock particles and the process is described by a diffusion-reaction equation. Assuming that rock particles are perfect spheres, and the reaction status only varies along the radius direction, the diffusion-reaction equation can be written as:

$$\varphi_r \frac{\partial C}{\partial t} = D_e \left(\frac{\partial^2 C}{\partial r^2} + \frac{2}{r} \frac{\partial C}{\partial r} \right) - S_{py} \tag{3-4}$$

where C is the oxygen concentration inside the rock particle varying with the radius location r and time t and is equivalent to the gaseous oxygen concentration C_g in Eq. (3-2); φ_r is the porosity of the rock particle; D_e is the oxygen diffusivity in the rock particle and S_{py} is the rate of oxygen consumption by pyrite grains in a unit volume of the pyrite-bearing rock. The boundary conditions for Eq. (3-4) is given as Eq. (3-5). At the rock particle surface, the first type of boundary condition is used and the boundary value for oxygen is given by the oxygen concentration in the space between rock particles. At the centre of the rock particle, the boundary condition is set as no diffusive flux, hence, the concentration gradient is zero.

$$\begin{aligned} C(r = R) &= C_0 \\ \frac{\partial C}{\partial r}(r = 0) &= 0 \end{aligned} \tag{3-5}$$

The value of S_{py} depends on the local oxygen concentration $C(r, t)$, pyrite grain size and the reaction progress of the pyrite grains. In this work, the pyrite grain size distribution (by mass) is defined as:

$$\begin{aligned} PSD_{py} &= \begin{pmatrix} R_1 & R_2 \dots R_i \dots R_n \\ m_1 & m_2 \dots m_i \dots m_n \end{pmatrix} \\ F_i &= \frac{m_i}{\frac{4}{3}\pi R_i^3 \cdot \rho_{py}} \end{aligned} \tag{3-6}$$

where R_i and m_i represent the i^{th} grain size radius and the corresponding relative mass proportion. ρ_{py} is the pyrite density and F_i represents the number of pyrite grains at the i^{th} grain size in a pyrite group with total mass of $\sum_{i=1}^{n} m_i$ and with this grain size distribution.

For each pyrite grain size, the oxygen consumption rate can be calculated by Eq. (3-2) or (3-3). For a unit volume of pyrite particles, the total oxygen consumption rate is the sum of the rates for the different sizes. This requires the solution of Eq. (3-2) or (3-3) for each pyrite grain size, which is computationally costly. For simplification, it is assumed that the depth of oxidation is the same for pyrite grains of different sizes under the same reaction environment. Hence

only one reaction rate model needs to be solved for the largest pyrite grain, and the reaction progress of smaller pyrite grains can be estimated quickly by the depth of oxidation solved from the obtained reaction rate model.

Based on this approximation, the overall reaction of a group of pyrite grains is defined by Eqs. (3-7) and (3-8) for cases with and without a diffusion barrier respectively. In Eqs. (3-7) and (3-8), $RateO_{gp}$ is the oxygen consumption rate of the pyrite group, R_n is the original radius of the largest pyrite grain in the group, r_c is the unreacted core radius of the pyrite of grain size R_n and $r_c(i)$ is the unreacted core radius of the pyrite grain size R_i (representing the reaction progress of the pyrite grain); k'' and D_s are the same as those in Eqs. (3-2) and (3-3), $C_e(r)$ is the effective oxygen concentration at radius r in the rock particles. Note that when $r_c(i)$ becomes zero, the corresponding contribution to the summation for $RateO_{gp}$ also becomes zero. The effect of the approximation is examined by comparing the results of Eq. (3-7) or (3-8) with those calculated from Eq. (3-2) or (3-3) for each pyrite grain size, as detailed in Appendix 3.A.

$$\begin{cases} RateO_{gp} = \sum_{i=1}^{n} [\dfrac{4\pi R_i^2 \cdot C_e(r)}{\dfrac{R_i}{D_s}\left(\dfrac{R_i}{r_c(i)} - 1\right) + \dfrac{1}{k''}\dfrac{R_i^2}{r_c(i)^2} C_e(r)^{0.5}} \cdot F(i)] \\ -\dfrac{dr_c}{dt} = \dfrac{bC_e(r)/\rho_B}{\dfrac{(R_n - r_c)r_c}{R_n D_s} + \dfrac{C_e(r)^{0.5}}{k''}} \\ r_c(i) = max\{0, R_i - (R_n - r_c)\} \end{cases} \tag{3-7}$$

$$\begin{cases} RateO_{gp} = \sum_{i=1}^{n} [\dfrac{4\pi R_i^2 \cdot C_e(r)}{\dfrac{1}{k''} \cdot \dfrac{R_i^2}{r_c(i)^2} \cdot C_e(r)^{0.5}} \cdot F(i)] \\ -\dfrac{dr_c}{dt} = \dfrac{b \cdot C_e(r)/\rho_B}{\dfrac{C_e(r)^{0.5}}{k''}} \\ r_c(i) = max\{0, R_i - (R_n - r_c)\} \end{cases} \tag{3-8}$$

The volumetric oxygen consumption rate S_{py} is then given by Eq. (3-9) where $Py\%$ is the volumetric content of pyrite:

$$S_{py} = RateO_{gp} \cdot \frac{Py\%}{\frac{4}{3}\pi \sum_{i=1}^{n}(R_i^3 \cdot F_i)} \tag{3-9}$$

In addition to pyrite grain size, the rock particle size is also an important factor when estimating the oxidation level of the material for a processing unit. In stockpiles, rock particles can have significantly different sizes ranging from the millimetre to the metre scale. The pyrite contained in rock fragments of various sizes has different accessibility to oxygen depending

on its radius location. For example, pyrite grains near the rock surface would have easier access to oxygen than those in the inner part of the rock particle and hence can be oxidised more quickly. In other words, the larger the rock particle, the more difficult for the internal pyrite to be oxidised. The accessibility to oxygen can be determined by the distance between the location of pyrite and the rock surface and based on this simplification, it can be assumed that the reaction progress is the same for pyrite with the same distance to the rock particle surface regardless of the rock particle size. Using this approximation, the solution of the diffusion-reaction equation (Eq. (3-4)) for a large rock particle can be used for rock particles of various smaller sizes.

Again, a discrete distribution is used in this work to define the rock particle size distribution in a stockpile:

$$PSD_{rock} = \begin{pmatrix} R_{rock}(1) & R_{rock}(2) \dots & R_{rock}(j) & \dots & R_{rock}(p) \\ m_{rock}(1) & m_{rock}(2) \dots & m_{rock}(j) & \dots & m_{rock}(p) \end{pmatrix}$$
$$F_{rock}(j) = \frac{m_{rock}(j)}{\frac{4}{3}\pi R_{rock}^3(j) \cdot \rho_{rock}} \tag{3-10}$$

where $R_{rock}(j)$ and $m_{rock}(j)$ represent the j^{th} rock particle size and the corresponding relative mass proportion; ρ_{rock} is the rock density and $F_{rock}(j)$ represents the number of rock particles at size $R_{rock}(j)$ among the rock particles of a total mass of $\sum_{j=1}^{p} m_{rock}(j)$ and with this particle size distribution. The largest rock particle of size $R_{rock}(p)$ is discretised into several layers with equal thickness of Δr; the layer sequence is denoted by k and $k = 1$ represents the outmost layer. The distance to the particle surface for layer k is $\frac{\Delta r}{2} + \Delta r(k - 1)$, hence k also denotes the distance sequence. All layers in rock particles of different sizes can be categorized into the distance sequence of $k \in [1, \frac{R_{rock}(p)}{\Delta r}]$. The total amount of pyrite $Py(k)$ at layer k in a unit volume of stockpile material is given by Eq. (3-11) where $Py\%$ is the volumetric content of pyrite.

$$\begin{cases} Py(k) = \dfrac{Py\% \cdot \sum_{j=1}^{p} [\frac{4}{3}\pi \cdot (r_{kj(1)}^3 - r_{kj(2)}^3) \cdot F_{rock}(j)]}{\frac{4}{3}\pi \sum_{j=1}^{p} \left(R_{rock}^3(j) \cdot F_{rock}(j)\right)} \\ r_{k,j(1)} = max\{R_{rock}(j) - \Delta r \cdot (k-1), 0\} \\ r_{k,j(2)} = max\{R_{rock}(j) - \Delta r \cdot k, 0\} \end{cases} \tag{3-11}$$

The oxygen consumption rate of a pyrite group at the distance category k can then be calculated by Eq. (3-7) or Eq. (3-8) with the oxygen concentration $C_e(r)$ solved from Eq. (3-4) for the layer k. Therefore, for a unit volume of stockpile material, the total oxygen consumption rate is given by Eq. (3-12) and the reaction progress of the pyrite grains is given by r_c as defined in Eq. (3-7) or Eq. (3-8) for each layer.

$$RateO_{vo} = \sum_{j=1}^{p} (RateO_{gp}(k) \cdot \frac{Py(k)}{\frac{4}{3}\pi \sum_{i=1}^{n}(R_i^3 \cdot F_i)}) \tag{3-12}$$

To summarize, the governing equations for pyrite oxidation in rock particles of different sizes are Eqs. (3-4), (3-7), (3-8) and (3-9) with the parameters given in Eq. (3-2). The total volumetric oxygen consumption rate is given in Eq. (3-12).

3.2.2 Oxygen transport

Oxygen transport over the stockpile can be described by the diffusion-advection equation for fluid flow transport in porous media with source/sink term shown as Eq. (3-13) (after Holzbecher (1998)):

$$\frac{\partial}{\partial t}(\varphi U) = \nabla(D_b \cdot \nabla U) - \nabla \cdot (\boldsymbol{\nu} \cdot U) + q_{O_2} \tag{3-13}$$

where U is the oxygen concentration in the void space of the stockpile, φ is the stockpile bulk porosity, D_b is the oxygen bulk diffusion coefficient over the stockpile, $\boldsymbol{\nu}$ is air velocity and q_{O_2} is the sink term, i.e., the volumetric oxygen consumption rate given by Eq. (3-12).

The bulk diffusion coefficient of oxygen D_b depends on the water content in the stockpile. The relationship used in the present model is that of Molson et al. (2005) which is based on the model proposed in Aachib et al. (2002):

$$D_b = \frac{1}{\theta_s^2}(D_a \theta_a^{P_a} + H^{cc} D_w \theta_w^{P_w}) \tag{3-14}$$

where θ_s is the saturated water content (or porosity), H^{cc} is the Henry's law of solubility, D_a and D_w are the oxygen diffusion coefficients in air and water respectively, θ_a and θ_w are the air-filled porosity and water content, and P_a and P_w are the fitting coefficients based on experimental data. The value $P_a = P_w = 10/3$ is suggested in Aachib et al. (2002) for most cases and is adopted in the work presented here.

The value of D_b also depends on temperature since both D_a and D_w are temperature dependent. The expression of the bulk diffusion coefficient D_b as a function of temperature T (in Kelvin) is given in Eq. (3-15) and its derivation is given in Appendix 3.B.

$$D_b = \frac{1}{\theta_s^2}(1.1005 \times 10^{-5} \cdot T^{1.726} \theta_a^{3.3} + 10^{-7} \times (0.0058T^2 - 2.146T + 163.35)\theta_w^{3.3}) \tag{3-15}$$

3.2.3 Heat transfer

The temperature profile for the stockpile can be described by the heat balance equation. Holzbecher (1998) presented the heat balance equation based on Fourier's law as shown in Eq. (3-16) considering heat source, heat conduction and heat convection through fluid flow in porous media:

$$\frac{\partial T}{\partial t} = \nabla \cdot (-\gamma \boldsymbol{v} T + D_h \nabla T) + \frac{q_h}{(\rho C)} \qquad \text{with} \qquad \gamma = \frac{\rho^* C^*}{(\rho C)} \tag{3-16}$$

In this work, only air flow is considered for the convective heat transfer. In Eq. (3-16), T is the temperature of the stockpile, $\boldsymbol{v}$ is the air velocity field, D_h is the thermal diffusivity, ρ and C are respectively the density and the specific heat capacity for the stockpile material, and ρ^* and C^* are those of the air. q_h is the heat source from pyrite oxidation and is defined as the volumetric rate of heat generation.

The heat generation rate per unit volume of material can be derived from the volumetric consumption rate of oxygen (Eq. (3-12)) as:

$$q_h = \delta \cdot b \cdot RateO_{vol} \tag{3-17}$$

where δ is the heat produced per mol of pyrite oxidised in the reaction and b is the stoichiometric coefficient. The value of δ used in this study is 1049 kJ after Wels et al. (2003).

3.2.4 Air velocity

The air velocity field $\boldsymbol{v}$ is required for both oxygen transport and heat transfer over the stockpile. According to Holzbecher (1998), the convective air flow is governed by the following equations:

Darcy's law for gas flow in porous media:

$$\boldsymbol{v} = -\frac{\kappa}{\mu}(\nabla P - \rho \boldsymbol{g}) \tag{3-18}$$

mass conservation of air:

$$\frac{\partial}{\partial t}(\varphi \rho) = -\nabla \cdot (\rho \boldsymbol{v}) \tag{3-19}$$

and the ideal gas law:

$$\rho = \frac{MP}{\bar{R}T} \tag{3-20}$$

where κ is the permeability of the porous media, μ is the dynamic viscosity of the gas, P is the pressure, ρ is the air density, $\boldsymbol{g}$ is the gravitational acceleration, φ is the stockpile porosity, M is the molar mass of air, $\bar{R}$ is the gas constant and T is the absolute temperature.

The variables of air density, temperature and pressure are included in Eqs. (3-18) to (3-20). Substituting Eqs. (3-18) and (3-20) into Eq. (3-19) to eliminate air density gives the partial differential equation that contains only pressure and temperature. As changes in air density and/or pressure do not cause changes in temperature in this open system, temperature can be treated as a known parameter in these equations. The final governing equation is given in Eq. (3-21) where B is the square of the pressure P. The derivation is given in Appendix 3.C.

$$\frac{\partial B}{\partial t} = \alpha \cdot \nabla^2 B + \boldsymbol{\beta} \cdot \nabla B + \theta \cdot B$$

$$\alpha = \frac{\kappa P_0}{\varphi \mu}$$

$$\begin{cases} \beta_x = -\dfrac{\kappa P_0}{\varphi \mu} \cdot \dfrac{1}{T} \dfrac{\partial T}{\partial x} \\ \beta_y = -\dfrac{\kappa P_0}{\varphi \mu} \cdot \dfrac{1}{T} \dfrac{\partial T}{\partial y} \\ \beta_z = -\dfrac{\kappa P_0}{\varphi \mu} \dfrac{1}{T} \cdot \left(\dfrac{\partial T}{\partial z} + \dfrac{2M\boldsymbol{g}}{\bar{R}}\right) \end{cases} \tag{3-21}$$

$$\theta = \frac{2}{T} \frac{\partial \mathrm{T}}{\partial \mathrm{t}} + \frac{\kappa P_0}{\varphi \mu} \frac{4M\boldsymbol{g}}{\bar{R}} \frac{1}{T^2} \frac{\partial T}{\partial z}$$

3.2.5 Numerical solution

The time-dependent governing equations are solved in three dimensions representing the shape and size of the stockpile. An Alternating Direction Implicit (ADI) finite difference scheme, termed the Douglas-Gunn method, is used to solve numerically the partial differential equations (PDEs) described above. The simulated processes, namely pyrite oxidation, oxygen transport, heat transfer and air convection, are coupled through variables passing between different sub-systems. For example, the oxygen concentration solved in the oxygen transport equation is passed to the pyrite oxidation model to calculate the pyrite reaction rate and oxygen consumption rate; the latter is then fed back to the oxygen transport equation as the sink term. Heat generation is also calculated from pyrite oxidation and is passed to the heat transfer equation as the source term. The solved temperature value is in turn used as the reaction temperature for the pyrite oxidation of the next time step. The temperature value is also used in the pressure equation to calculate the air velocity field based on the solved

pressure profile. The calculated air velocity is then fed into the transport equations for both oxygen and heat.

Different iteration approaches were used for the coupling between different processes. As shown in Fig. 3-1, within each time step, the coupling between temperature and pressure is first performed using the sequential iterative approach (SIA); the solved temperature and air velocity are then passed to the oxygen transport and pyrite oxidation processes, which are coupled using the Newton-Raphson (N-R) method. The calculated heat generation rate is fed to the temperature equation in the temperature-pressure iteration loop for the next time step and the above calculations are repeated. A sequential non-iterative approach is adopted between heat transfer and pyrite oxidation to avoid self-increase of temperature as the two processes mutually promote each other.

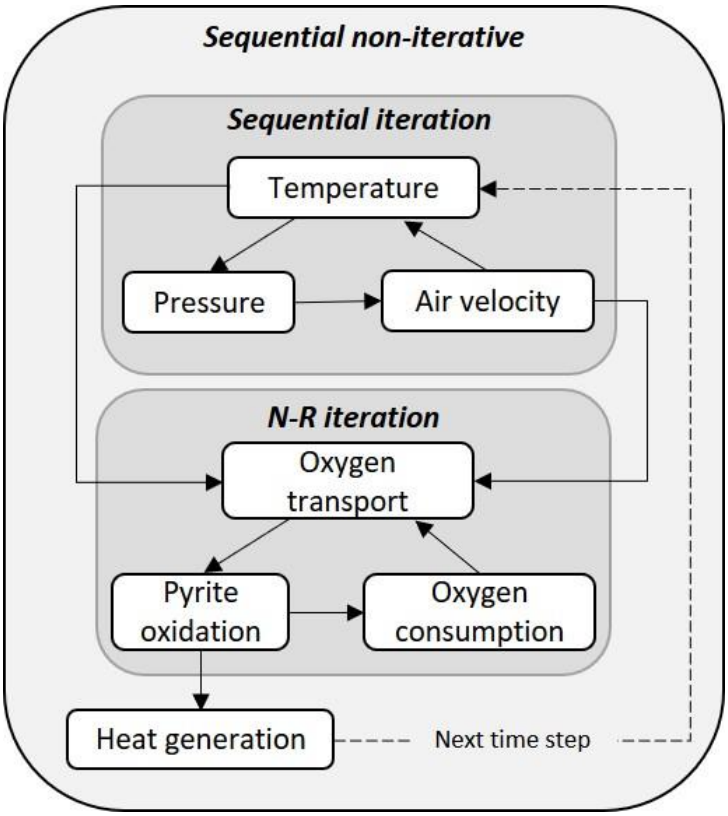

Fig. 3-1: The numerical solution strategy for the coupling among heat transfer, oxygen transport and pyrite oxidation

For the case study described below, a time step of one day is used for all processes except for the diffusion-reaction equation of rock particles, where a time step of 1.2 hours is used to accommodate the small spatial step discretising the rock particles. High Performance Computing (HPC) clusters were used to run the simulations in this paper and the run time depends on the number of iterations required and the size of the model. On average, for a simulation with 14586 nodes and 3650 time-steps, around 900 core-hours are required (each simulation took around 45 hours using a computer node with 20 cores and 32G memory).

3.3 Results and discussions

3.3.1 Test case model

The test rock stockpile model is 102 m long, 52 m wide and 22 m high. A rectangular grid is used with each node representing a block. This allows easy transfer of stockpile properties and simulation results from and to a block model format commonly used in mining operations. The spatial step/block size of the test model is 2 m × 2 m × 2 m.

Note that in our modelling system, the oxygen transport is simulated at two different scales. One is at the bulk scale over the stockpile, where it is assumed that oxygen concentration in the void space of the stockpile is uniform within each block. This assumption also applies for temperature, pressure and air velocity for each block to simplify the system. The other scale is the diffusion of oxygen within rock particles, where the oxidation of pyrite grains is modelled, and the oxygen consumption rate is calculated. To avoid non-positive oxygen concentration resulting from a large volumetric consumption rate, a lower limit of 0.5 mol-O_2/m^3-air for oxygen concentration is imposed, below which the pyrite reaction rate parameters (i.e., D_s and k'' in Eq. (3-2)) decrease exponentially. This assumption was found to be necessary for cases in which the pyrite surface area within a unit volume is large, i.e., when pyrite content is high and/or pyrite grain sizes are small. Although, with the original reaction rate parameters, the intrinsic reaction rate decreases dramatically at low oxygen concentration, the total oxygen consumption by all reacting pyrite grains can still be excessively large such that the consumption rate (which is constant within the current time step) cannot be compensated by the oxygen replenishing rate and the available oxygen at the current time step. By setting the reaction rate coefficients to decrease exponentially with low oxygen concentration, the volumetric reaction rate will be maintained at a minimal level to avoid generating negative oxygen concentration. A similar setting is also used in the model in Lefebvre et al. (2001) where the reaction rate becomes zero when oxygen concentration is below a threshold value.

For the boundary conditions for oxygen concentration, no diffusive flux boundary is assumed at the stockpile bottom and a first-type boundary condition, i.e., a constant atmospheric oxygen concentration, is applied at the stockpile surface with a constant value being assigned to the virtual blocks that cover the stockpile surface.

For the temperature profile, the simulated region includes both the stockpile and a region of 10 m directly below the stockpile to consider the effect of geothermal heat on the oxidation process. A constant temperature value is used as the first-type boundary condition at the bottom of the extended region of the model. Heat loss is considered at the stockpile surface. The boundary conditions for the modelled variables are described in Appendix 3.D. Fig. 3-2 provides a schematic diagram of the test case model.

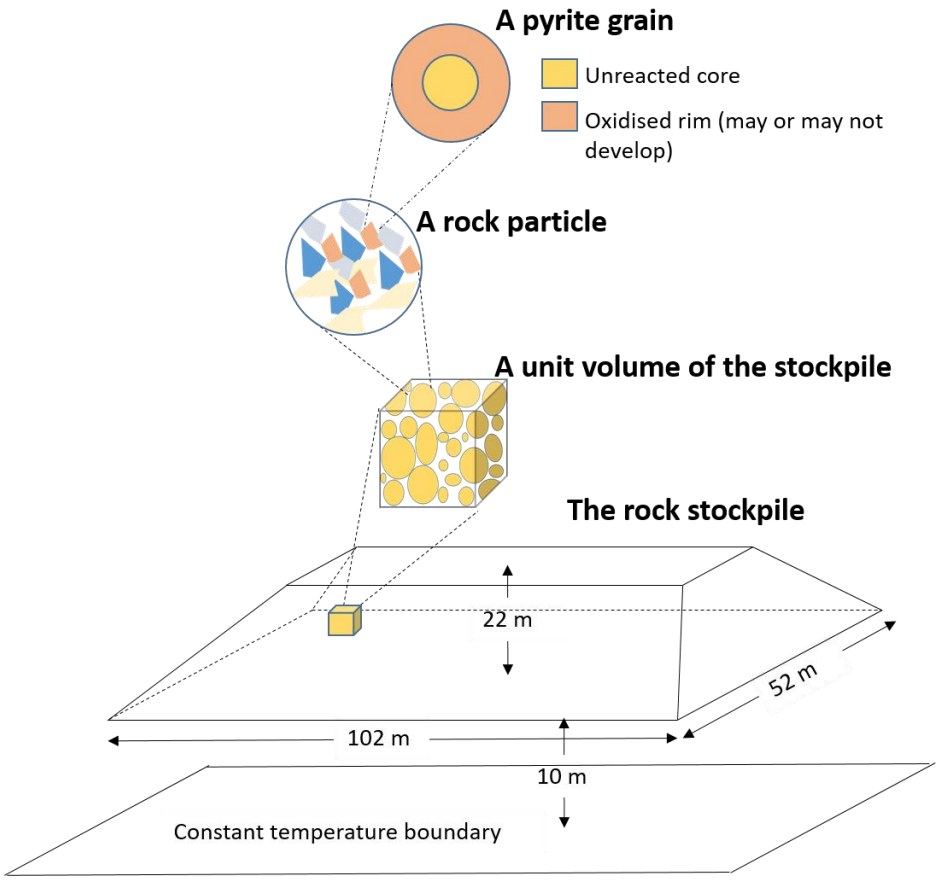

Fig. 3-2: Test case model for pyrite oxidation in rock stockpiles

It is assumed that the test case stockpile consists of three different material types, Material A, Material B and Material C, each of which has different properties for rock particle size distribution, pyrite grain size distribution, rock diffusion coefficient and porosity, pyrite content, and acid neutralisation capacity (ANC), as shown in Table 3-1, Table 3-2 and Table 3-3. Values for pyrite content and particle size distributions for rock and pyrite grains are derived from the measured values for samples taken from a rock stockpile. The porosity values of the three types of rocks are taken as the measured values of dolomite, sandstone and mudstone in Peng et al. (2012). Values for the rock diffusion coefficients are assumed based on the measurements documented in Voutilainen et al. (2018) where the magnitude of rock diffusivity is around 10^{-9} m^2/s. In Table 3-3, the factor F_ANC represents the relative acid neutralization capacity for different material types, which are used to estimate the pH value based on Eq. (3-22).

$$pH = -log_{10}(2 \cdot OxiLevel \cdot Py\% \cdot \rho_B / \varphi / 1000 / F\_ANC) \quad (3\text{-}22)$$

Where $OxiLevel$ is the overall oxidation level of that block, $Py\%$ is the pyrite content, ρ_B is pyrite molar density, φ is the porosity of the bulk material of the block. Other fixed parameters used in the simulation are given in Table 3-4.

Table 3-1: Rock particle size distribution (by mass) for different material types

Bins of rock particle size (in diameter, mm)		+125	-125 +31.5	-31.5 +1.25	-1.25
Average size used for simulation (in diameter, mm)		250	78.25	16.375	1.25
Mass dist. (%)	Material A	22.36	30.18	24.83	22.64
	Material B	32.94	28.22	19.92	18.92
	Material C	31.4	30.73	19.78	18.09

Table 3-2: Pyrite grain size distribution for different material types

Bin of pyrite grain size (in diameter, μm)		-30000 +10600	-10600 +5300	-5300 +2650	-2650 +1000	-1000 +500	-500 +250	-250 +50
Average size used for simulation (μm)		20250	7950	3975	1825	750	375	150
Mass dist. (%)	Material A	3.7	6.2	16.4	25.2	24.8	15.7	8
	Material B	17.9	10.7	19.2	21.2	16.6	9.7	4.7
	Material C	32.6	15	18.1	15	10.4	6.4	2.5

Table 3-3: Parameters used in the simulations for different material types

Parameters	Material A	Material B	Material C
Porosity	0.09	0.15	0.3
Diffusion coefficient (m^2s^{-1})	10^{-9}	5×10^{-9}	8×10^{-9}
Pyrite content	5%	3%	10%
Factor of ANC	200	400	100

Table 3-4: Other parameters used in the simulations

Parameters	Value	Unit/Comment
Stoichiometric coefficient of pyrite reaction	2/7	Pyrite to oxygen
Pyrite molar density ρ_B	4.17×10^4	$mol\cdot m^{-3}$
Gravitational acceleration g	-9.8	$m\cdot s^{-2}$
Reference air density ρ	1.165	$kg\cdot m^{-3}$
Gas constant $\bar{R}$	8.314	$Pa\cdot m^3\cdot mol^{-1}\cdot K^{-1}$
Henry's law constant H^{cc}	3.2×10^{-2}	@ 25 °C
Specific heat capacity of air C_g	1006.1	$J\cdot K^{-1}\cdot kg^{-1}$
Volumetric heat capacity of rock media	1.98×10^6	$J\cdot K^{-1}\cdot m^{-3}$
Heat generated per mole of pyrite reacted	1.409×10^6	$J\cdot mol^{-1}$
Heat loss coefficient	0.3	$W\cdot K^{-1}\cdot m^{-2}$
Heat diffusivity of the stockpile material	1.4×10^{-6}	$m^2\cdot s^{-1}$
Initial O_2 concentration C in air	8.28	$mol\cdot m^{-3}$
Initial and reference pressure P_0	1	atm
Initial temperature T_0	23	°C

In the test case model, each block of the stockpile was randomly assigned a type of rock material. The model also takes the stockpile construction stage into consideration, i.e., new material was added to the stockpile at different times. This can take place periodically from the time when the stockpile was initially constructed to the present date, leading to constant changes in the size and shape of the stockpile. Consequently, the access to air for both oxygen replenishment and heat transfer of each block would vary and the total time of exposure to air of different blocks would also be different depending on the time when the block was added to the stockpile. The present model updates the geometry of the modelled region during the simulation according to the variations in the size and shape of the stockpile. Fig. 3-3 shows the size and shape of the test case stockpile at different stages with block colours indicating material types.

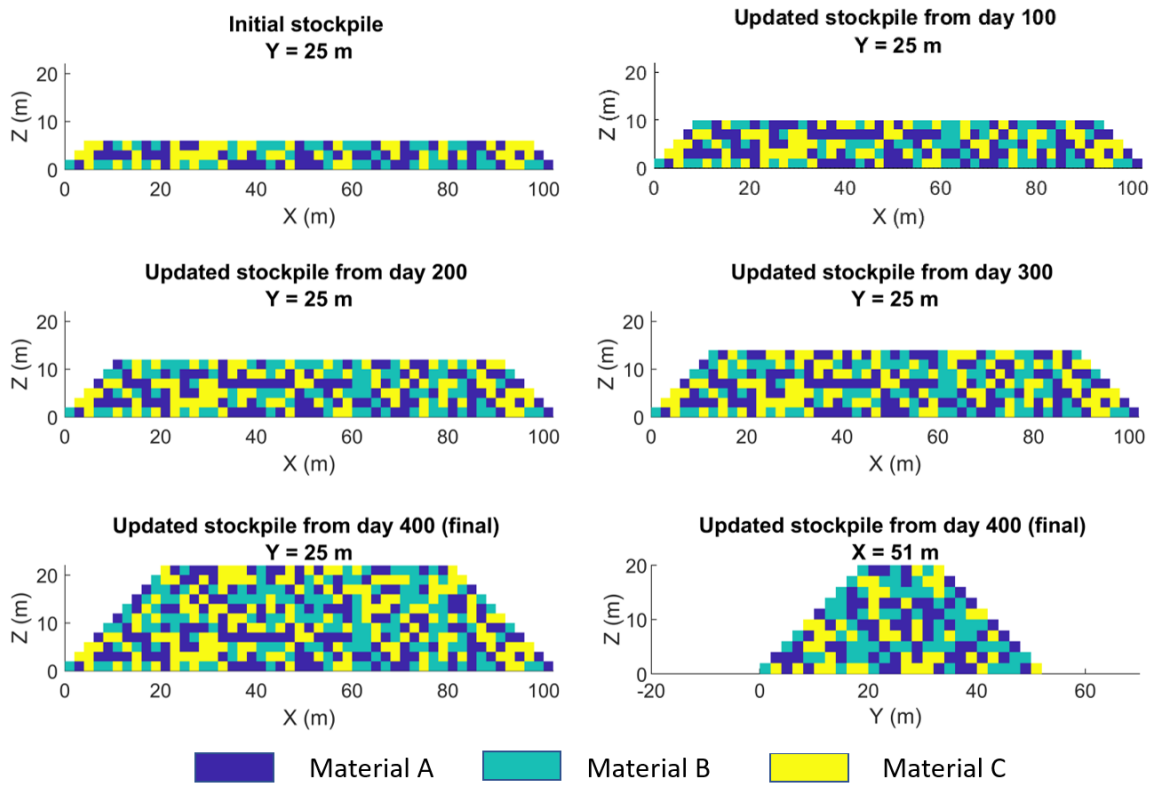

Fig. 3-3: The size and shape of the stockpile at different stages and its associated distribution of different types of rock materials

3.3.2 Results of the base case model

The values of stockpile porosity, permeability and degree of water saturation used for the base case model are given in Table 3-5. All other parameters not specified here use the values listed in Section 3.3.1. The temperature dependent parameters for pyrite oxidation (i.e., the reaction rate constant and diffusion coefficient through the diffusion barrier) are as provided in the governing equations (Eq. (3-2)).

Table 3-5: Specific parameters used in the base case simulation

Parameters	Value	Unit
Porosity of the stockpile	0.4	
Air permeability of the stockpile	10^{-12}	m^{-2}
Water saturation degree of the stockpile	25%	
Temperature boundary value at 10 m below	70	°C

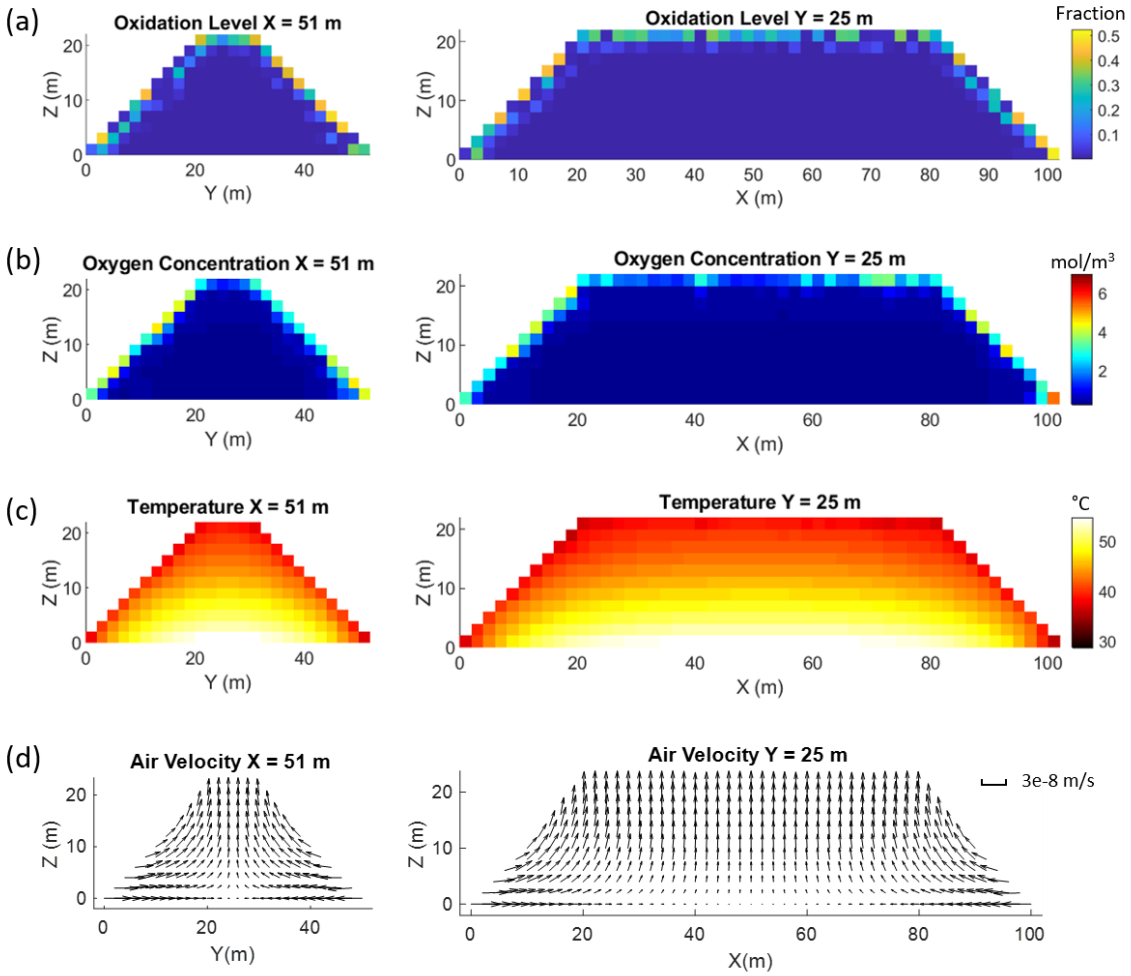

Fig. 3-4: Simulated results for the base case model: (a) pyrite oxidation level; (b) oxygen concentration (mol·m^{-3}); (c) temperature (°C); (d) air velocity (m·s^{-1})

Fig. 3-4 and Fig. 3-5 shows the simulated results for the base case ten years after the stockpile construction. The level of pyrite oxidation over the stockpile ranges from 0.12% to 52.41%, with the highly oxidised blocks mainly on the stockpile surface. The oxygen concentration profile shows that oxygen concentration is at a significant level only at the surface of the stockpile which is still far below the atmospheric oxygen concentration (8.28 mol/m^3), whereas for locations beneath the stockpile surface, the oxygen concentration is only 0.2 to 0.4 mol/m^3 as a result of relatively fast consumption by pyrite oxidation. The stockpile temperature has risen due to the heat generated from the reaction over the years. The

highest temperature occurs at the bottom of the stockpile due to the geothermal heat, reaching 55°C (initial and ambient atmosphere temperature is 23°C); and the temperature gradually decreases from this location to the surface of the stockpile to about 36°C to 40°C. This temperature gradient over the stockpile induces the air flow that comes into and out of the stockpile as shown in Fig. 3-4d. The magnitude of the air velocity is small, only up to 3.83 × 10^{-8} m·s^{-1} or 1.21 metres per year.

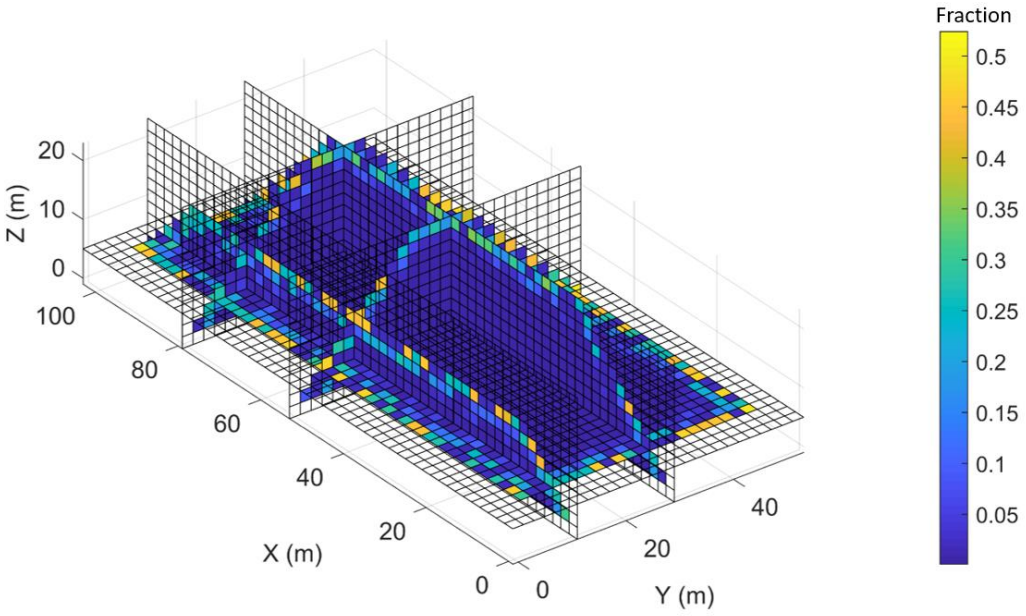

Fig. 3-5: The oxidation level over the stockpile after ten years

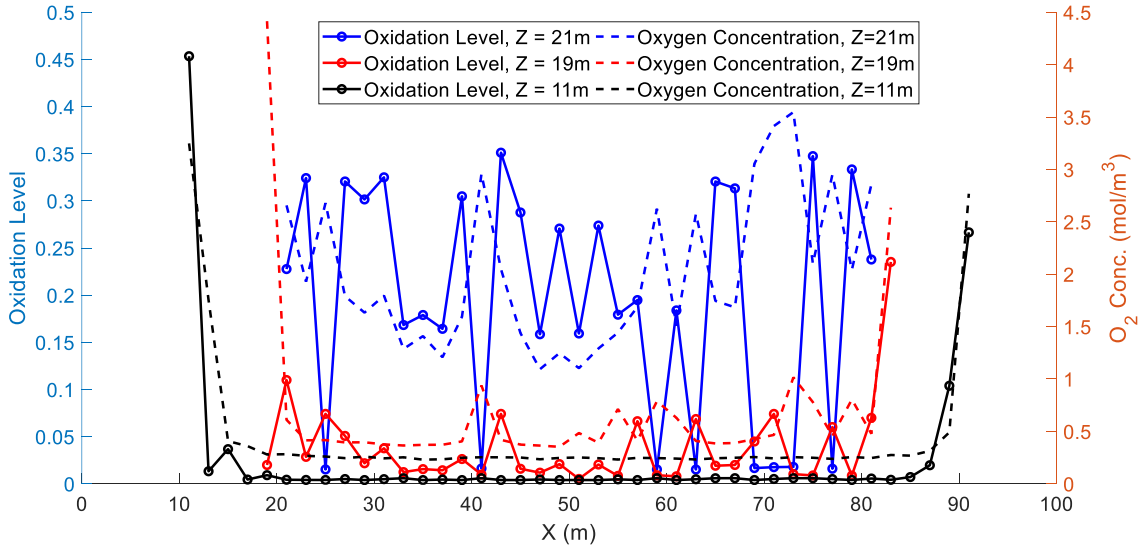

Fig. 3-6: The oxidation level and oxygen concentration along the central line of different layers in the stockpile

The simulated profiles for the level of pyrite oxidation (Fig. 3-5) and oxygen concentration (Fig. 3-4b) are similar, indicating that at the stockpile scale, the pyrite oxidation is dominantly determined/limited by the oxygen concentration. Note that on the stockpile surface,

although all blocks have the same access to oxygen (exposed to the atmosphere), some blocks are less oxidised than others due to the difference in the types of rock materials. This is further illustrated in Fig. 3-6 which shows that the oxidation level at the surface (Z = 21m) varies from less than 0.05 to about 0.35. The oxygen concentration in these blocks also varies and the variation trend is, in general, opposite to that of the oxidation level. This is mainly because the oxygen concentration is affected by the oxygen consumption rate in that block, i.e., it will be maintained at a low value if the consumption rate is high. Fig. 3-6 also shows that as the depth of the block increases (from the stockpile surface to the bottom), both oxidation level and oxygen concentration decrease with less variability laterally across the stockpile. This indicates that as the depth increases, the reaction rate is increasingly limited by the availability of oxygen and less affected by the reactivity of the materials.

Overall, the oxidation levels for different types of materials are significantly different. Fig. 3-7 shows the histograms of block oxidation levels for each type of material, which suggests that the Material B blocks are much less oxidised than the other two types of blocks. The average oxidation levels for Material A, Material B and Material C blocks are 11.47%, 0.91% and 6.80% respectively. These differences are caused by the differences in the material properties, mainly the acid neutralisation capacity which determines the time required to go into the fast reaction stage in which coating does not develop on pyrite grain surfaces.

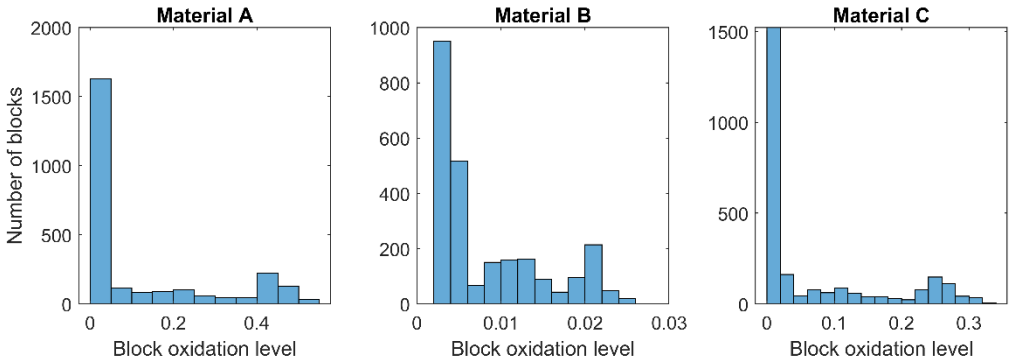

Fig. 3-7: Histograms of oxidation level of blocks after ten years for each material types

Fig. 3-8 shows the variations of oxidation level, oxygen concentration and temperature with time for six selected blocks with their locations marked in Fig. 3-8a. The oxidation levels of these blocks increase with time at different rates. Oxygen concentration decreases initially due to consumption by reaction, and then stabilises at a certain level from year two, indicating an achieved equilibrium between consumption and replenishment. Similarly, the temperature increases for the first three years due to reaction and then also stabilises in subsequent years for most blocks, indicating that the heat transfer process over the stockpile has stabilised. Blocks 1, 2 and 3 are all Material A but with very different oxygen concentration and temperature over time. Consequently, the oxidation levels of these blocks are significantly different as shown in Fig. 3-8b. In Fig. 3-8c, although blocks 4, 5 and 6 have very similar temperatures and accessibility to oxygen, the oxidation rates are very different due to different types of materials in these blocks. Although the Material C rock type has the highest diffusion coefficient and the smallest acid neutralisation capacity (see Table 3-3), the block oxidation level is less than that of the Material A block due to the high pyrite content.

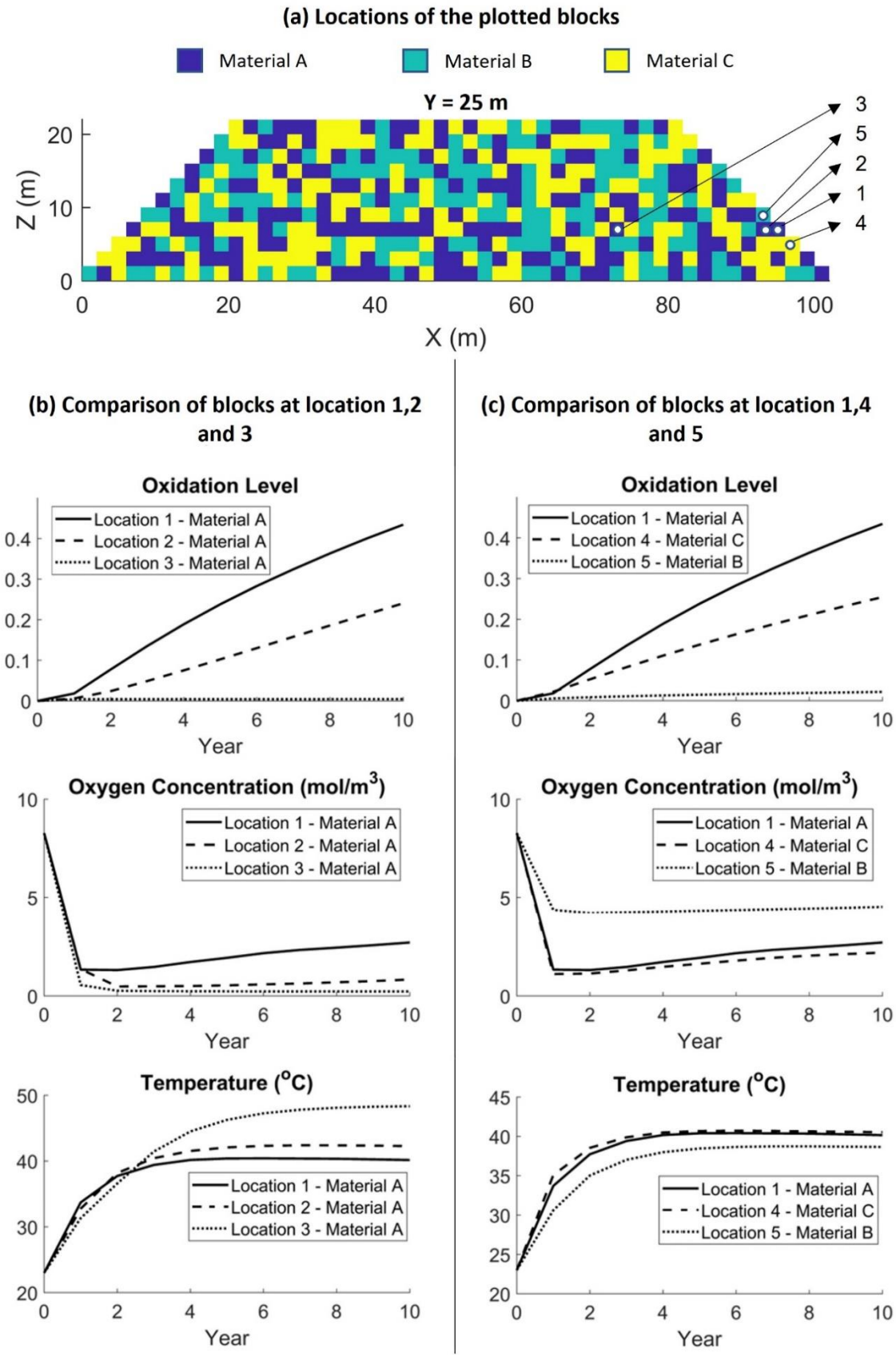

Fig. 3-8: Variation of the oxidation level, oxygen concentration and temperature at different locations: (a) The locations of the plotted blocks; (b) Blocks of same material type at different locations; (c) Blocks of different material types at comparable locations

In addition to the oxidation level at block scale, the proposed model is also able to estimate the oxidation profiles of pyrite grains in rock particles, which is an important input required for the estimation of the gold recovery by direct cyanide leaching from oxidised gold-bearing material. Gold distribution in pyrite is not homogeneous and can exhibit a certain pattern termed chemical zoning, resulting from specific rock-fluid interactions and the crystal growth kinetics during mineralisation (see, for example, Wu et al. (2019)). Pyrite grains may not need to be completely oxidised to recover the majority of the available gold content depending on the gold distribution in the pyrite. In some cases, gold may mostly be in the rim or mantle of the pyrite grains so that a shallow oxidation depth may be sufficient to release most of the gold content. Therefore, knowing the oxidation profile of pyrite grains is essential for the estimation of gold recovery without pre-treatment.

As discussed in Section 3.2.1, pyrite grains contained in the rock particles are oxidised to different degrees, decreasing from the outmost layer to the inner layers of the rock particles. The shorter the distance to the rock particle surface, the higher the depth of oxidation of the contained pyrite grains. As an example, the most oxidised block, located at (1m, 51m, 1m), with an overall oxidation level of 52.41% is used to illustrate the simulated oxidation profile of pyrite grains within a rock particle. Fig. 3-9 shows the depth of the oxidation of pyrite grains at different distances to the rock surface after ten years. As can be seen from the Fig. 3-9, only pyrite grains within a distance of around 25 mm to the surface of the rock particle are oxidised, with the corresponding depth of oxidation ranging from 6 µm to 404 µm depending on the distance.

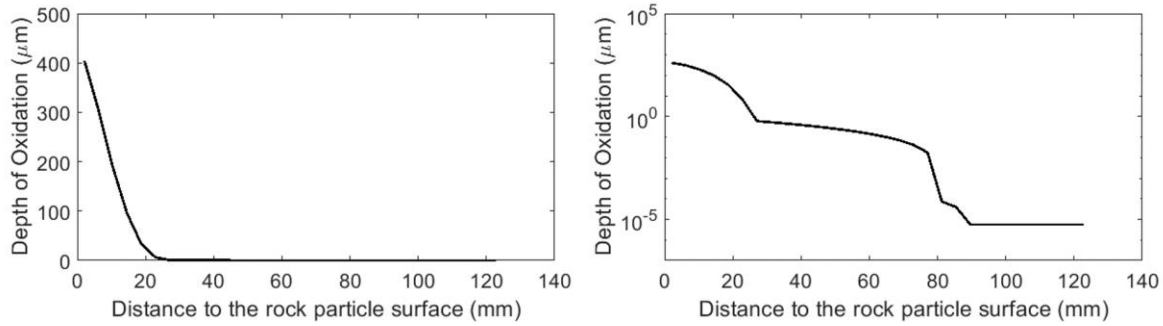

Fig. 3-9: The oxidation depth of the pyrite grains at different distances to the rock particle surface in the block at x=1m, y=51m, z=1m: left – linear scale; right – lognormal scale.

The oxidation level for pyrite grains of various sizes can be calculated from the depth of oxidation and the results are shown in Fig. 3-10. As can be seen, the oxidation level for pyrite grains of different sizes can be very different, ranging from less than 0.08 to about 0.84. For pyrite grains of the same size, the oxidation level also varies depending on pyrite location within the rock particle. Fig. 3-11 shows the relative depth of oxidation, i.e., the ratio of the depth of oxidation to the grain radius. It shows that for pyrite grains smaller than 375 µm, more than half of the pyrite is almost completely oxidised. As the grain size increases, the relative depth of oxidation decreases. For pyrite grains larger than 7.95 mm, only a thin layer of the pyrite rim has been oxidised after ten years.

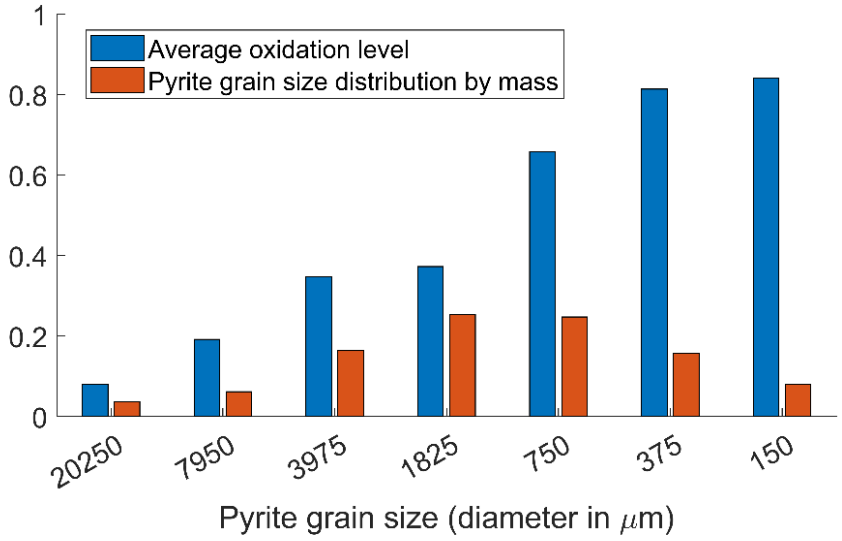

Fig. 3-10: The oxidation level for pyrite grains of various sizes in a Material A block with 52.41% overall oxidation level

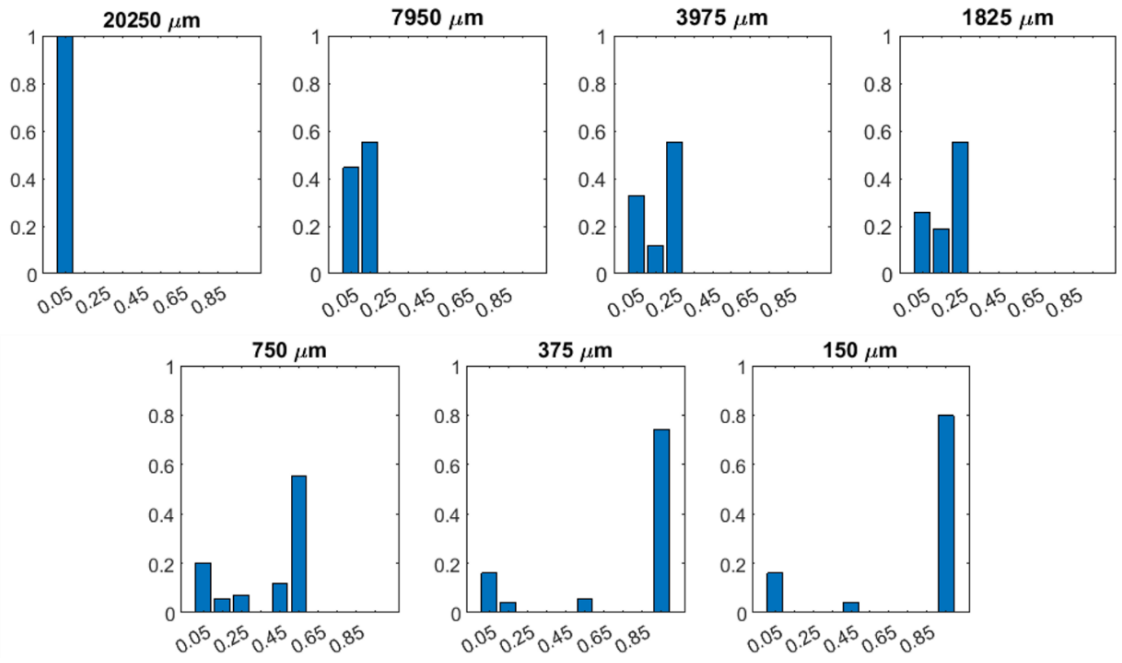

Fig. 3-11: The distribution of the relative depth of oxidation of pyrite grains at different sizes

3.3.3 Simulations of other scenarios

To study the influence of different parameters on the stockpile oxidation level, different scenarios have been simulated and compared with the base case model presented above. The variations of parameters examined in these scenarios are listed in Table 3-6.

Table 3-6: Scenarios examined for parametric studies

Cases		Changes of parameters examined
0.	Base case	
1.	Smaller rock diffusion coefficient	1e-10, 5e-10 and 8e-10 m^2s^{-1} for Material A, Material B and Material C respectively, which are ten times smaller than those used in the base case.
2.	No convection	Air velocity is set to zero.
3.	Lower porosity	Porosity changes from 0.4 to 0.25.
4.	Low water saturation	Degree of water saturation changes from 25% to 8%.
5.	Higher water saturation	Degree of water saturation changes from 25% to 80%.
6.	No geothermal heat	Boundary temperature value changes from 70°C to 15°C at the bottom of the extended region.

Fig. 3-12 shows cross-sectional views of the simulated oxidation level, oxygen concentration and temperature for the scenarios explored. Similar to the base case results, the oxidation level of the internal part of the stockpile in all cases is less than 20% while only blocks near the stockpile surface are significantly oxidised, confirming that oxygen is the dominant limiting factor for the stockpile oxidation in all cases. A comparison of the scenarios reveals that the oxidation level at the stockpile surface in Cases 1, 3 and 5 is much less than that in other cases. This can also be seen in Fig. 3-13, where the oxidation level and oxygen concentration along the central line in the x-direction at different depths of the stockpile are plotted. The curves fluctuate across the stockpile due to the variations in the location as well as the types of material. The results of the base case, Case 2 and Case 6 are very close, with their curves hard to separate in the figure, which indicates that the effects of air convection and geothermal heat are negligible in the base case.

Among all the cases, Case 1 has the highest oxygen concentration at all depths (Fig. 3-13) due to slow oxygen consumption resulting from a smaller rock diffusion coefficient. Compared with the base case, the stockpile in Case 1 is less oxidised at the surface (Z = 21 m) but slightly more oxidised at Z = 19 m due to a higher oxygen concentration at that depth. This shows that, when oxygen replenishment is limited, the more reaction that occurs at the stockpile surface, the less oxygen is available for the reaction internally within the stockpile.

Case 3 uses a decreased stockpile porosity, resulting in smaller oxygen concentration and a lower oxidation level over the stockpile than the corresponding values of the base case. Case 5 shows similar results by increasing the water content in the stockpile. In both cases, the bulk transport of oxygen is inhibited, resulting in limited amounts of oxygen available for reaction. On the contrary, with a lower water content, Case 4 has the highest oxidation level and higher oxygen concentration than most cases at all depths due to faster oxygen replenishment. Although published research has shown that the optimal degree of water saturation is around 25% for pyrite oxidation under laboratory conditions (León et al., 2004), this comparison

study shows that for a larger scale (e.g. block scale or stockpile scale), a smaller water content would be more favourable since it increases oxygen replenishment over the blocks or stockpile.

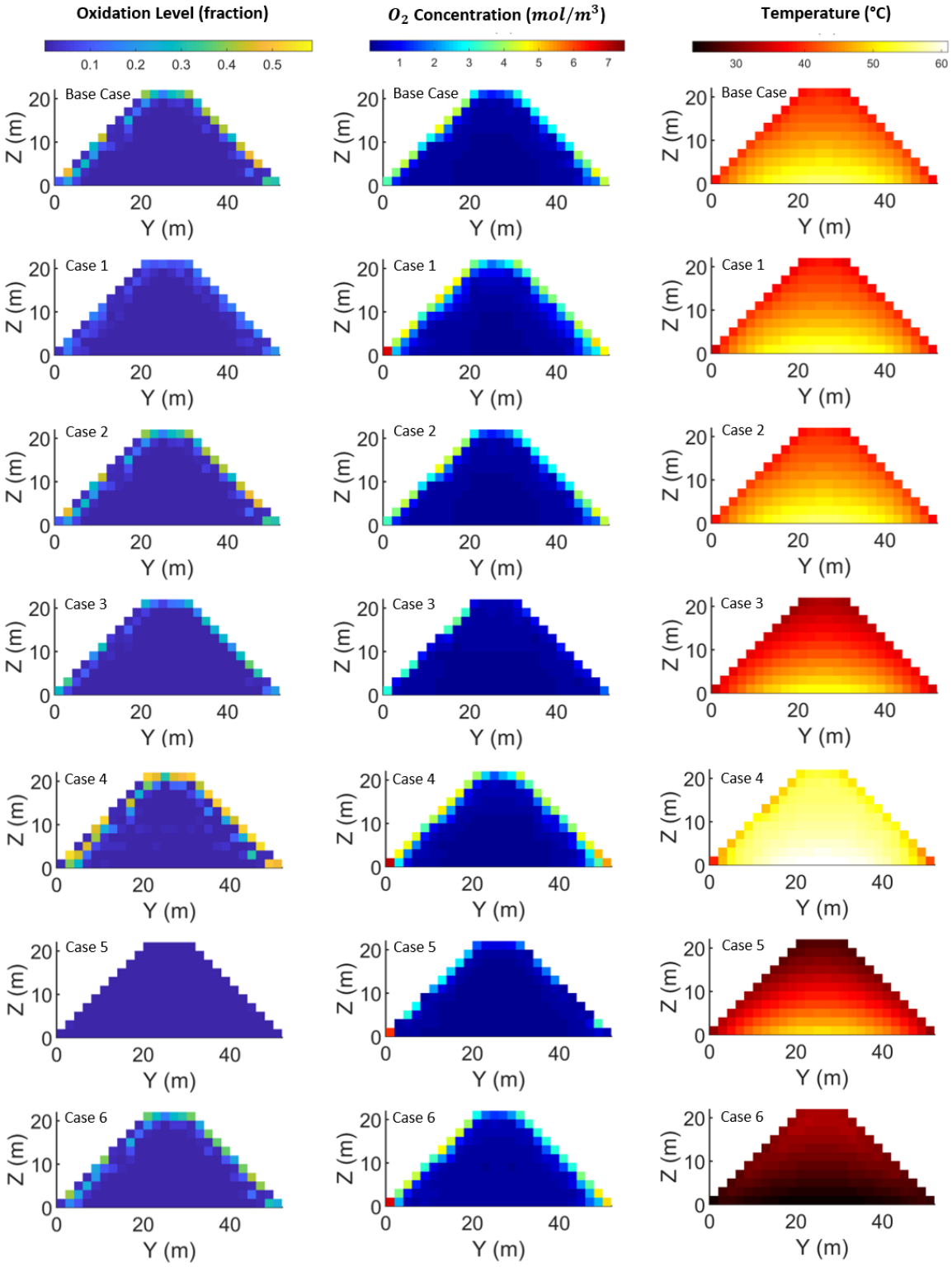

Fig. 3-12: Simulated oxidation level, oxygen concentration and temperature for all cases. Cross-sections are at X=51m

The comparison analyses discussed above confirm that the availability of oxygen is the most influential rate-limiting factor for pyrite oxidation in stockpiles. The effective transport of oxygen is dominantly through diffusion and the contribution from convection is negligible when the permeability of the stockpile is 1 Darcy or smaller and the stockpile is under natural environmental conditions without any forced air flow. Therefore, properties that affect oxygen diffusivity over the stockpile would have significant impacts on the pyrite oxidation level. These properties mainly include the bulk porosity (hence rock particle size) of the stockpile and water content. Temperature also has some impact on the oxidation level, but to a much lesser degree compared with the oxygen availability and it has very little impact unless there is sufficient oxygen available for the reaction.

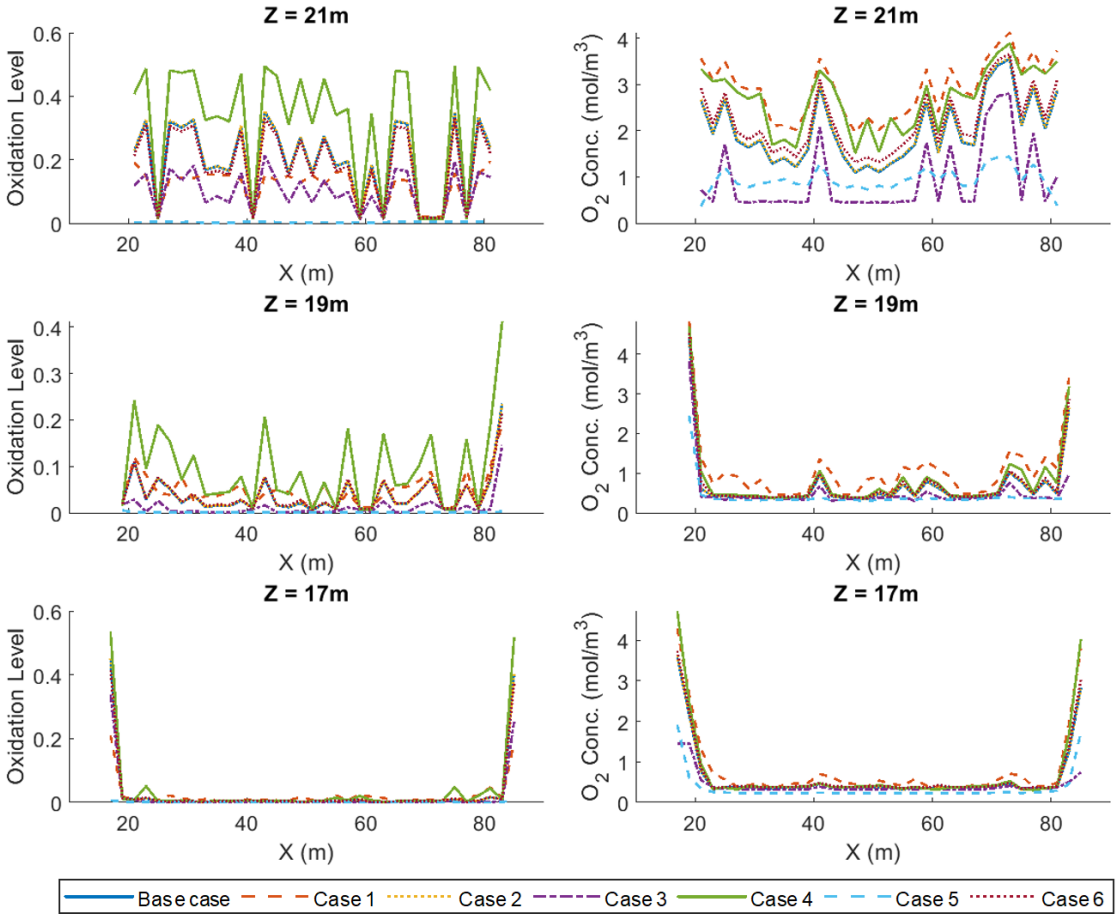

Fig. 3-13: Oxidation level and oxygen concentration on the vertical section at y=25m and different depths. Case 1 – smaller diffusion coefficients of rock particles; Case 2 – no convection; Case 3 – smaller porosity; Case 4 – 8% water saturation degree; Case 5 – 80% water saturation degree; Case 6 – no geothermal heat

3.3.4 Conclusions

This paper presents a numerical modelling framework for estimating the pyrite oxidation level in refractory gold ore stockpiles. The solution framework couples pyrite oxidation with phyiscal processes including oxygen transport and geothermal heat transfer, and is capable of modelling the influences of oxygen concentration, temperature, water content, pH value

and rock material properties, such as particle size distribution, on pyrite oxidation within the stockpile. The comparison study of different scenarios shows that oxygen availiblity is the most important influencing factor for pyrite oxidation within the stockpile and any conditions that affect oxygen availability, such as stockpile porosity and water content, have a significant impact on the overall oxidation level. In addition, in the proposed framework, the oxidation of pyrite grains contained in rock particles is modelled using the diffusion-reaction equation in which the reaction term is obtained by the reaction rate model for pure pyrite grains. This approach allows the estimation of the oxidation level of pyrite grains at different distances to the surface of rock particles of various sizes. The framework presented here will facilitate the estimation of potential gold recovery through direct cyanidation in partially oxidised stockpiles.

Appendix 3.A The approximated solutions of the oxidation of a group of pyrite grains at various sizes

The oxidation of a group of pyrite grains is described by two variables: one is the total oxygen consumption rate and the other is the oxidation level of the pyrite grains calculated from the unreacted core radius. The performance of the approximation using Eqs. (3-7) and (3-8) is examined by comparing the total oxygen consumption rate of the pyrite group and the oxidation level of pyrite grains at different sizes.

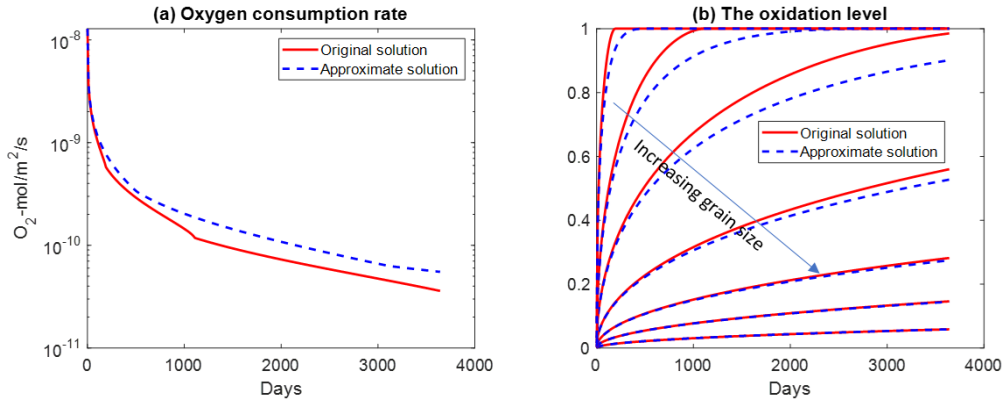

Fig. A-1: Comparison of pyrite oxidation with diffusion barrier: (a) The total oxygen consumption rate (y axis is in lognormal scale); (b) The oxidation level of pyrite grains

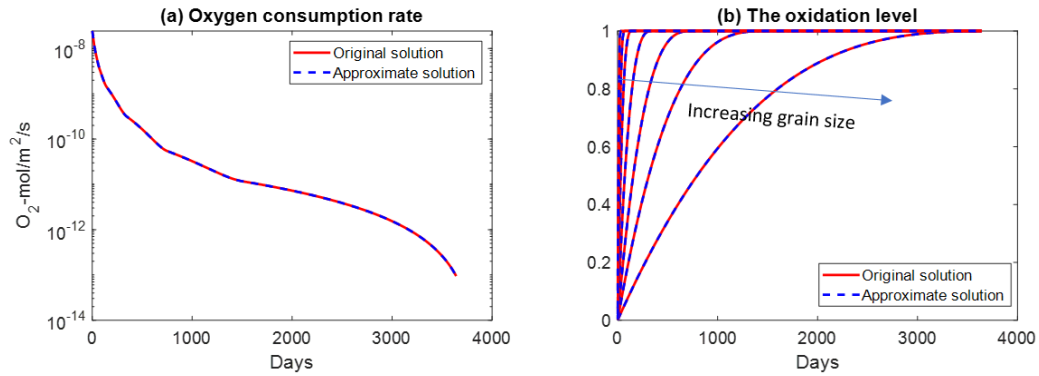

Fig. A-2: Comparison for pyrite oxidation without diffusion barrier: (a) The total oxygen consumption rate (y axis is in lognormal scale); (b) The oxidaiton level of pyrite grians.

Fig. A-1 and Fig. A-2 compare the approximation to the original solution for pyrite oxidation with and without a diffusion barrier respectively. The oxygen consumption rate is normalized by the initial total surface area of the original pyrite grains. The pyrite grain size distribtion (by mass or volume) in the calculation uses the values for Material A in Table 3-2 with the sizes scaled down by a factor of 50 so as to have complete reaction for at least small size pyrite grains (large pyrite grains cannot be completely reacted within a decade when a diffusion barrier develops). The approximate solutions are reasonably close to the orignal ones (Fig. A-1) for cases with a diffusion barrier, espeically for the total oxygen consumption rate. For cases without a diffusion barrier (Fig. A-2), the results are almost identical.

Appendix 3.B The effect of temperature on the bulk diffusion coefficient

The diffusion coefficient model proposed by Aachib et al. (2002) is shown in Eq. (3-14) and is repeated here as:

$$D_b = \frac{1}{\theta_s^2}(D_a\theta_a^{P_a} + H^{cc}D_w\theta_w^{P_w}) \tag{3-B1}$$

The oxygen diffusion coefficient D_a as a function of temperature is given by the Chapman-Enskog theory as shown in Eq. (3-B2) (Cussler, 2009):

$$D_a = \frac{1.86\cdot 10^{-3}T^{3/2}(1/M_1 + 1/M_2)^{1/2}}{p\sigma_{12}^2\Omega} \tag{3-B2}$$

where p is the atmospheric pressure, T is the absolute temperature, M_1 and M_2 are the molecular weights of oxygen and air respectively, σ_{12} is the collision diameter of oxygen in air, Ω is the collision integral in the Chapman-Enskog theory. The value of Ω is determined by the value of K_BT/ε_{12}, where K_B is the Boltzmann constant and ε_{12} is the interaction energy between colliding molecules. Table 5.1-3 in Cussler (2009) lists the measured values of Ω at different K_BT/ε_{12} values for an oxygen-air binary system for temperature ranging from 25°C to 235°C, based on which a relationship is fitted as Eq. (3-B3) with an R-square value of 0.992.

$$\Omega = 1.2123 \times (K_BT/\varepsilon_{12})^{-0.226} \tag{3-B3}$$

According to Cussler (2009), for the oxygen-air pair, the values of the Lennard-Jones potential parameters are: σ_1 = 3.467, σ_2 = 3.711, ε_1/K_B = 106.7, ε_2/K_B = 78.6, therefore:

$$\sigma_{12} = \frac{1}{2}(\sigma_1 + \sigma_2) = 3.589 \tag{3-B4}$$

$$\varepsilon_{12}/K_B = \sqrt{(\varepsilon_1/K_B)\,(\varepsilon_2/K_B)} = 91.58 \tag{3-B5}$$

Substituting Eqs. (3-B3), (3-B4) and (3-B5) into Eq. (3-B2) gives:

$$D_a = 1.1005 \times 10^{-5} \times T^{1.726} \tag{3-B6}$$

The oxygen diffusion coefficient in water can be estimated from the Stokes-Einstein equation:

$$D_w = \frac{K_B T}{6\pi\mu R_0} \tag{3-B7}$$

where μ is the solvent viscosity and R_0 is the Stokes radius of the solute which has a value of 1.73×10^{-8} cm according to Cussler (2009). The water viscosity equation is given by Eq. (3-B8) (Al-Shemmeri, 2012).

$$\mu(T) = 2.414 \times 10^{-5} \times 10^{247.8/(T-140)} \tag{3-B8}$$

Therefore, Eq. (3-B7) can be converted to Eq. (3-B9):

$$D_w = 1.753 \times 10^{-5} \times \frac{T}{10^{247.8/(T-140)}} \tag{3-B9}$$

A polynomial approximation to Eq. (3-B9) with an R-square value of 0.9998 gives:

$$D_w = 10^{-6} \times (0.0193T^2 - 7.124T + 542.33) \tag{3-B10}$$

Substituting Eq. (3-B6) and Eq. (3-B10) into Eq. (3-B1) gives the oxygen bulk diffusion coefficient as a function of temperature, which is written as Eq. (3-B11) (Eq. (3-15)).

$$D_e = \frac{1}{\theta_s^2}(1.1005 \times 10^{-5} \cdot T^{1.726}\theta_a^{3.3} + 10^{-7} \times (0.0058T^2 - 2.146T + 163.35)\theta_w^{3.3}) \tag{3-B11}$$

Appendix 3.C The non-isothermal pressure profile and air velocity field

The governing equations for convective air flow are given by Darcy's law for gas flow in porous media, mass conservation and the ideal gas law, as shown in Eqs. (3-18) to (3-20) and are repeated here as Eqs. (3-C1) to (3-C3).

$$\boldsymbol{v} = -\frac{\kappa}{\mu}(\nabla P - \rho \boldsymbol{g}) \tag{3-C1}$$

$$\frac{\partial}{\partial t}(\varphi\rho) = -\nabla \cdot (\rho \boldsymbol{v}) \tag{3-C2}$$

$$\rho = \frac{MP}{\bar{R}T} \tag{3-C3}$$

Substituting Eq. (3-C1) and Eq. (3-C3) into Eq. (3-C2) to eliminate the density variable and assume isotropic permeability and viscosity, gives Eq. (3-C4):

$$\varphi \frac{\partial}{\partial t}\left(\frac{MP}{\bar{R}T}\right) = \frac{\kappa}{\mu}\nabla \cdot \left(\frac{MP}{\bar{R}T}\left(\nabla P - \frac{MP}{\bar{R}T}\boldsymbol{g}\right)\right) \tag{3-C4}$$

As M and $\bar{\mathrm{R}}$ are constants, they can be cancelled on each side of equation, and therefore:

$$\varphi \frac{\partial}{\partial t}\left(\frac{P}{T}\right) = \frac{\kappa}{\mu}\nabla \cdot \left(\frac{P}{T}\left(\nabla P - \frac{MP}{\bar{R}T}\boldsymbol{g}\right)\right) \tag{3-C5}$$

Eq. (3-C5) can be written as:

$$\frac{1}{T^2}\left(\frac{\partial P}{\partial t}T - \frac{\partial T}{\partial t}P\right) = \frac{\kappa}{\varphi\mu}\left[\frac{1}{T^2}\left(T \cdot \nabla\left(P(\nabla P)\right) - \nabla T \cdot P(\nabla P)\right) - \frac{M\boldsymbol{g}}{\bar{R}}\nabla\left(\frac{P}{T}\right)^2\right] \tag{3-C6}$$

Note that:

$$P(\nabla P) = \frac{1}{2}\nabla P^2 \tag{3-C7}$$

$$\nabla\left(P(\nabla P)\right) = \frac{1}{2}\nabla^2(P^2) \tag{3-C8}$$

Substituting Eq. (3-C7) and Eq. (3-C8) into Eq. (3-C6) and rearranging gives:

$$\frac{\partial P}{\partial t} = \frac{1}{\mathrm{T}}\frac{\partial \mathrm{T}}{\partial \mathrm{t}} \cdot \mathrm{P} + \frac{\kappa}{\varphi\mu}\left(\frac{1}{2}\nabla^2(P^2) - \frac{\nabla T}{T} \cdot \frac{1}{2}\nabla P^2\right) - \frac{\kappa}{\varphi\mu}\frac{M\boldsymbol{g}}{\bar{R}}\frac{1}{T}\nabla P^2 + \frac{\kappa}{\varphi\mu}\frac{M\boldsymbol{g}}{\bar{R}}\frac{2\nabla T}{T^2}P^2 \tag{3-C9}$$

Eq. (3-C9) is a time-dependent partial differential equation (PDE) for pressure and temperature. Considering that temperature does not change much with pressure, it can be treated as a constant and Eq. (3-C9) is a PDE of pressure. The left-hand side is the time derivative of the pressure P and on the right-hand side are P and the first and second order derivative of P^2 with constant coefficients. This form of partial differential equation is still

difficult to solve because it involves both P and derivatives of P^2. To solve for pressure in Eq. (3-C9), the approximation in Eq. (3-C10) is used based on the assumption that the pressure in the void space fluctuates around an average value of P_0 and the fluctuation is small (Warrick, 2001).

$$P = P_0 + \Delta P, \quad P \approx P_0 \tag{3-C10}$$

Eq. (3-C9) can then be manipulated as:

$$2P \cdot \frac{\partial P}{\partial t} = 2P \cdot \frac{1}{\mathrm{T}} \frac{\partial \mathrm{T}}{\partial \mathrm{t}} \cdot \mathrm{P} + 2P_0 \cdot \frac{\kappa}{\varphi\mu} \left(\frac{1}{2} \nabla^2 (P^2) - \frac{\nabla T}{T} \cdot \frac{1}{2} \nabla P^2 \right) - 2P_0 \cdot \frac{\kappa}{\varphi\mu} \frac{M\boldsymbol{g}}{\bar{R}} \frac{1}{T} \nabla P^2 + 2P_0 \cdot \frac{\kappa}{\varphi\mu} \frac{M\boldsymbol{g}}{\bar{R}} \frac{2\nabla T}{T^2} P^2 \tag{3-C11}$$

which then becomes an equation in the variable P^2:

$$\frac{\partial P^2}{\partial t} = \frac{2}{T} \frac{\partial \mathrm{T}}{\partial \mathrm{t}} \cdot \mathrm{P}^2 + \frac{\kappa P_0}{\varphi\mu} \nabla^2 P^2 - \frac{\kappa P_0}{\varphi\mu} \frac{\nabla T}{T} \cdot \nabla P^2 - \frac{\kappa P_0}{\varphi\mu} \frac{2M\boldsymbol{g}}{\bar{R}} \frac{1}{T} \nabla P^2 + \frac{\kappa P_0}{\varphi\mu} \frac{4M\boldsymbol{g}}{\bar{R}} \frac{\nabla T}{T^2} P^2 \tag{3-C12}$$

Let $P^2 = B$, then Eq. (3-C12) is an equation in B which has the form of Eq. (3-C13) with coefficients independent of the variable B and only dependent on the temperature profile. The coefficients are given in Eq. (3-C14).

$$\frac{\partial B}{\partial t} = \alpha \cdot \nabla^2 B + \boldsymbol{\beta} \cdot \nabla B + \theta \cdot B \tag{3-C13}$$

$$\alpha = \frac{\kappa P_0}{\varphi\mu}$$

$$\begin{cases} \beta_x = -\dfrac{\kappa P_0}{\varphi\mu} \cdot \dfrac{1}{T} \dfrac{\partial T}{\partial x} \\ \beta_y = -\dfrac{\kappa P_0}{\varphi\mu} \cdot \dfrac{1}{T} \dfrac{\partial T}{\partial y} \\ \beta_z = -\dfrac{\kappa P_0}{\varphi\mu} \dfrac{1}{T} \cdot \left(\dfrac{\partial T}{\partial z} + \dfrac{2M\boldsymbol{g}}{\bar{R}} \right) \end{cases} \tag{3-C14}$$

$$\theta = \frac{2}{T} \frac{\partial \mathrm{T}}{\partial \mathrm{t}} + \frac{\kappa P_0}{\varphi\mu} \frac{4M\boldsymbol{g}}{\bar{R}} \frac{1}{T^2} \frac{\partial T}{\partial z}$$

Appendix 3.D The boundary conditions of the test case model

Two types of boundaries are considered for the test case model for temperature, pressure and oxygen concentration. One is the top stockpile surface in contact with the atmosphere and the other is the bottom boundary of the stockpile in contact with the ground surface.

For temperature, heat loss to the atmosphere can occur at the top stockpile surface when its temperature is higher than the atmospheric temperature. In this case, the heat loss is given by Eq. (3-D1) where T is the stockpile temperature at the surface, $T_\propto$ is the atmospheric temperature, h is the heat loss coefficient and $\boldsymbol{q}$ is the heat flux from the boundary block to the atmosphere. The heat flux at the boundary is also subject to the constraint of heat conduction between stockpile blocks, which is given by Eq. (3-D2), where λ is the thermal conductivity of the stockpile.

$$|\boldsymbol{q}| = h \cdot \Delta T = h \cdot (T - T_\propto) \tag{3-D1}$$

$$\boldsymbol{q} = -\lambda \cdot \frac{\partial T}{\partial l} \tag{3-D2}$$

Substituting Eq. (3-D1) into Eq. (3-D2) gives Eq. (3-D3), which is the boundary condition for temperature at the top stockpile surface considering heat loss.

$$\frac{\partial T}{\partial l} = \frac{-\boldsymbol{q}}{|\boldsymbol{q}|}\frac{h \cdot (T - T_\propto)}{\lambda}, l = x, y, z \tag{3-D3}$$

At the bottom of the stockpile, the temperature is affected by both the geothermal heat and the topography of the stockpile. To consider both factors, the simulated region for temperature is extended to include a region 10 m directly below the stockpile, and the bottom of this extended region is the new boundary for modelling temperature. At this boundary, a constant high temperature value T_g is applied to represent the supply of geothermal heat from the underground source (Eq.(3-D4)). At the sides of the extended underground region, a symmetry boundary condition is applied as given by Eq. (3-D5).

$$T = T_g \tag{3-D4}$$

$$\frac{\partial T}{\partial l} = 0, l = x, y \tag{3-D5}$$

For pressure, the first-type boundary condition is applied at the top stockpile surface where the pressure is set as the atmospheric pressure. At the bottom stockpile surface, the condition

of no air flow through the boundary is applied, which gives $\boldsymbol{v}_l = 0$, where l represents x, y or z directions. Applying this boundary condition to the x and y direction gives a zero pressure gradient along these two directions:

$$\frac{\partial P}{\partial l} = 0, l = x, y \tag{3-D6}$$

Applying this boundary condition to the z direction as $\boldsymbol{v}_z = 0$ gives:

$$\frac{\partial P}{\partial z} = \rho \boldsymbol{g} \tag{3-D7}$$

Substituting the ideal gas law (Eq. (3-20) into Eq. (3-D7) to eliminate the density variable gives:

$$\frac{\partial P}{\partial z} = \frac{MP}{\bar{R}T}\boldsymbol{g} \tag{3-D8}$$

Therefore, for the variable $B = P^2$ in Eq. (3-21), the boundary conditions are given as Eq. (3-D9) and Eq. (3-D10) for top and bottom stockpile surfaces respectively:

$$B = P_0^2 \tag{3-D9}$$

$$\begin{cases} \dfrac{\partial B}{\partial l} = 0, l = x, y \\ \dfrac{\partial B}{\partial z} = \dfrac{2M\boldsymbol{g}}{RT} \cdot B \end{cases} \tag{3-D10}$$

Similarly, for oxygen concentration, the first-type boundary is applied at the top stockpile surface where the atmospheric oxygen concentration is used (Eq. (3-D11)). At the bottom stockpile surface, the condition of no diffusive flux through the boundary is applied, which leads to Eq. (3-D12).

$$U = U_0 \tag{3-D11}$$

$$\frac{\partial U}{\partial l} = 0, l = x, y, z \tag{3-D12}$$

Note that a virtual boundary is used in the numerical scheme when implementing the boundary conditions. The virtual boundary includes the nodes/blocks that are not physically

part of the stockpile (or the modelled region) but are directly in contact with the stockpile boundaries. The purpose of using this approach is to generate solutions for all nodes within the stockpile or the modelled region, including the boundary nodes. For example, for oxygen concentration at the top stockpile surface, the boundary value is assigned to the virtual boundary that can be regarded as air blocks covering the stockpile surface. Consequently, the oxygen concentration in the stockpile surface blocks can be solved by considering oxygen transport and consumption.

Acknowledgement

This research was financially supported by Newcrest Mining Limited.

References

Aachib, M, Aubertin, M & Mbonimpa, M 2002, 'Laboratory measurements and predictive equations for gas diffusion coefficient of unsaturated soils', in *55th Canadian Geotechnical Conference and 3rd joint IAH-CNC and CGS Groundwater Specialty Conference.(Niagara Falls, Ontario),* pp. 163-172.

Al-Shemmeri, T 2012, *Engineering fluid mechanics*, Bookboon.

Brown, P, Luo, X-L, Mooney, J & Pantelis, G 1999, 'The modelling of flow and chemical reactions in waste piles', in *2nd Internat. Conf. CFD in the Minerals and Process Industries. CSIRO, Melbourne, Australia, December,* pp. 6-8.

Cathles, L & Apps, J 1975, 'A model of the dump leaching process that incorporates oxygen balance, heat balance, and air convection', *Metallurgical Transactions B*, vol. 6, no. 4, pp. 617-624.

Chandra, AP & Gerson, AR 2010, 'The mechanisms of pyrite oxidation and leaching: A fundamental perspective', *Surface Science Reports*, vol. 65, no. 9, pp. 293-315.

Chiriță, P & Schlegel, ML 2017, 'Pyrite oxidation in air-equilibrated solutions: An electrochemical study', *Chemical Geology*, vol. 470, pp. 67-74.

Cussler, EL 2009, *Diffusion: mass transfer in fluid systems*, Cambridge university press.

da Silva, JC, do Amaral Vargas, E & Sracek, O 2009, 'Modeling Multiphase Reactive Transport in a Waste Rock Pile with Convective Oxygen Supply', *Vadose Zone Journal*, vol. 8, no. 4, pp. 1038-1050.

Davis, GB & Ritchie, AIM 1986, 'A model of oxidation in pyritic mine wastes: part 1 equations and approximate solution', *Applied Mathematical Modelling*, vol. 10, no. 5, pp. 314-322.

Elberling, B, Nicholson, RV & Scharer, JM 1994, 'A combined kinetic and diffusion model for pyrite oxidation in tailings: a change in controls with time', *Journal of Hydrology*, vol. 157, no. 1–4, pp. 47-60.

Elberling, B, Schippers, A & Sand, W 2000, 'Bacterial and chemical oxidation of pyritic mine tailings at low temperatures', *Journal of Contaminant Hydrology*, vol. 41, no. 3–4, pp. 225-238.

Evangelou, VP & Zhang, YL 1995, 'A review: Pyrite oxidation mechanisms and acid mine drainage prevention', *Critical Reviews in Environmental Science and Technology*, vol. 25, no. 2, 1995/05/01, pp. 141-199.

Gerke, HH, Molson, JW & Frind, EO 1998, 'Modelling the effect of chemical heterogeneity on acidification and solute leaching in overburden mine spoils', *Journal of Hydrology*, vol. 209, no. 1, pp. 166-185.

Holzbecher, EO 1998, *Modeling density-driven flow in porous media: principles, numerics, software*, vol. 1, Springer Science & Business Media.

Huminicki, DMC & Rimstidt, JD 2009, 'Iron oxyhydroxide coating of pyrite for acid mine drainage control', *Applied Geochemistry*, vol. 24, pp. 1626-1634.

Jaynes, DB, Pionke, HB & Rogowski, AS 1984, 'Acid mine drainage from reclaimed coal strip mines 2. Simulation results of model', *Water Resources Research*, vol. 20, no. 2, pp. 243-250.

Lefebvre, R 1995, 'Modeling acid mine drainage in waste rock dumps', *Conference: TOUGH 95: transport of unsaturated ground water and heat workshop, Berkeley, CA (United States), 20-22 Mar 1995; Other Information: PBD: Mar 1995; Related Information: Is Part Of Proceedings of the TOUGH Workshop `95 Lawrence Berkeley Laborato*, pp. Medium: ED; Size: pp. 239-244.

Lefebvre, R, Hockley, D, Smolensky, J & Lamontagne, A 2001, 'Multiphase transfer processes in waste rock piles producing acid mine drainage: 2. Applications of numerical simulation', *Journal of Contaminant Hydrology*, vol. 52, pp. 165-186.

León, EA, Rate, A, Hinz, C & Campbell, G 2004, 'Weathering of sulphide minerals at circum-neutral-pH in semi-arid/arid environments: Influence of water content', in *Proc., SuperSoil 2004: 3rd Australian New Zealand Soils Conf*.

Levenspiel, O 1999, 'Chemical reaction engineering', *Industrial & engineering chemistry research*, vol. 38, no. 11, pp. 4140-4143.

Mayer, KU, Frind, EO & Blowes, DW 2002, 'Multicomponent reactive transport modeling in variably saturated porous media using a generalized formulation for kinetically controlled reactions', *Water Resources Research*, vol. 38, no. 9, pp. 13-11-13-21.

McKibben, MA & Barnes, HL 1986, 'Oxidation of pyrite in low temperature acidic solutions: Rate laws and surface textures', *Geochimica et Cosmochimica Acta*, vol. 50, no. 7, pp. 1509-1520.

Molson, JW, Fala, O, Aubertin, M & Bussière, B 2005, 'Numerical simulations of pyrite oxidation and acid mine drainage in unsaturated waste rock piles', *Journal of Contaminant Hydrology*, vol. 78, no. 4, pp. 343-371.

Moses, CO & Herman, JS 1991, 'Pyrite oxidation at circumneutral pH', *Geochimica et Cosmochimica Acta*, vol. 55, no. 2, 1991/02/01, pp. 471-482.

Nicholson, RV, Gillham, RW & Reardon, EJ 1988, 'Pyrite oxidation in carbonate-buffered solution: 1. Experimental kinetics', *Geochimica et Cosmochimica Acta*, vol. 52, no. 5, 1988/05/01, pp. 1077-1085.

Pabst, T, Molson, J, Aubertin, M & Bussière, B 2017, 'Reactive transport modelling of the hydro-geochemical behaviour of partially oxidized acid-generating mine tailings with a monolayer cover', *Applied Geochemistry*, vol. 78, 2017/03/01/, pp. 219-233.

Pantelis, G 1993, 'FIDHELM: Description of model and users guide', *Australian Nuclear Science and Technology Organisation Report ANSTO M*, vol. 123.

Pantelis, G, Ritchie, A & Stepanyants, Y 2002, 'A conceptual model for the description of oxidation and transport processes in sulphidic waste rock dumps', *Applied Mathematical Modelling*, vol. 26, no. 7, pp. 751-770.

Parkhurst, DL, Thorstenson, DC, Plummer, N & U.S. Geological Survey, WRD 1980, 'PHREEQE : a computer program for geochemical calculations', in *Water-Resources Investigations Report*.

Peng, S, Hu, Q & Hamamoto, S 2012, 'Diffusivity of rocks: Gas diffusion measurements and correlation to porosity and pore size distribution', *Water Resources Research*, vol. 48, no. 2, pp. n/a-n/a.

Pruess, K 1991, *TOUGH2: A general-purpose numerical simulator for multiphase nonisothermal flows*, Lawrence Berkeley Lab., CA (United States).

Schoonen, M, Elsetinow, A, Borda, M & Strongin, D 2000, 'Effect of temperature and illumination on pyrite oxidation between pH 2 and 6', *Geochemical Transactions*, vol. 1, no. 4, p. 23.

Simunek, J, Sejna, M & Van Genuchten, MT 1999, 'The HYDRUS-2D Software Package', *International Ground Water Modeling Center*.

Singer, PC & Stumm, W 1970, 'Acidic mine drainage: the rate-determining step', *Science*, vol. 167, no. 3921, pp. 1121-1123.

Voutilainen, M, Ikonen, J, Sammaljarvi, J, Siitari-Kauppi, M, Lindberg, A, Kuva, J, Timonen, J & Lofgren, M 2018, *Investigation of Rock Matrix Retention Properties - Supporting Laboratory Studies II: Diffusion Coefficient and Permeability*.

Walter, A, Frind, E, Blowes, D, Ptacek, C & Molson, J 1994, 'Modeling of multicomponent reactive transport in groundwater: 1. model development and evaluation', *Water Resources Research*, vol. 30, no. 11, pp. 3137-3148.

Wang, H, Dowd, PA & Xu, C 2019, 'A reaction rate model for pyrite oxidation considering the influence of water content and temperature', *Minerals Engineering*, vol. 134, 2019/04/01/, pp. 345-355.

Warrick, AW 2001, *Soil physics companion*, CRC press.

Wels, C, Lefebvre, R & Robertson, AM 2003, 'An overview of prediction and control of air flow in acid-generating waste rock dumps', in *Proceedings Sixth International Conference on Acid Rock Drainage,* pp. 639-650.

Williamson, MA & Rimstidt, JD 1994, 'The kinetics and electrochemical rate-determining step of aqueous pyrite oxidation', *Geochimica et Cosmochimica Acta*, vol. 58, no. 24, pp. 5443-5454.

Wu, Y-F, Fougerouse, D, Evans, K, Reddy, SM, Saxey, DW, Guagliardo, P & Li, J-W 2019, 'Gold, arsenic, and copper zoning in pyrite: A record of fluid chemistry and growth kinetics', *Geology*, vol. 47, pp. 641-644.

Wunderly, M, Blowes, D, Frind, E & Ptacek, C 1996, 'Sulfide mineral oxidation and subsequent reactive transport of oxidation products in mine tailings impoundments: A numerical model', *Water Resources Research*, vol. 32, no. 10, pp. 3173-3187.

Chapter 4

Modelling pyrite oxidation in a refractory gold ore stockpile to estimate the gold recovery via direct cyanide leaching – a case study

Statement of Authorship

Title of Paper	Modelling pyrite oxidation in a refractory gold ore stockpile to estimate the gold recovery via direct cyanide leaching – a case study
Publication Status	☐ Published ☐ Accepted for Publication ☑ Submitted for Publication ☐ Unpublished and Unsubmitted w ork w ritten in manuscript style
Publication Details	Updates: Accepted for Publication on 31 Aug 2021 Wang, H., Dowd, P.A. and Xu, C. 2021 'Modelling pyrite oxidation in a refractory gold ore stockpile to estimate the gold recovery via direct cyanide leaching – a case study', submitted to *Minerals Engineering*

Principal Author

Name of Principal Author (Candidate)	Hang Wang		
Contribution to the Paper	Method development, simulations, data analysis and manuscript drafting.		
Overall percentage (%)	70%		
Certification:	This paper reports on original research I conducted during the period of my Higher Degree by Research candidature and is not subject to any obligations or contractual agreements with a third party that would constrain its inclusion in this thesis. I am the primary author of this paper.		
Signature		Date	7/04/2021

Co-Author Contributions

By signing the Statement of Authorship, each author certifies that:

i. the candidate's stated contribution to the publication is accurate (as detailed above);

ii. permission is granted for the candidate in include the publication in the thesis; and

iii. the sum of all co-author contributions is equal to 100% less the candidate's stated contribution.

Name of Co-Author	Peter A. Dowd		
Contribution to the Paper	Supervision, design of the work and reviewing the manuscript.		
Signature		Date	09/04/2021

Name of Co-Author	Chaoshui Xu		
Contribution to the Paper	Supervision, design of the work and reviewing the manuscript.		
Signature		Date	8-4-2021

Please cut and paste additional co-author panels here as required.

Abstract

This paper presents a case study of the modelling of the natural oxidation of pyrite in a refractory gold ore stockpile at a mine on the island of Aniolam in Papua New Guinea to predict the gold recovery through direct cyanide leaching. The stockpile comprises low-grade material that was mined twenty years ago to access the orebody. The value of this low-grade resource could be increased if the processing cost could be reduced. The natural oxidation of the gold-bearing pyrite in the stockpile may reduce the processing cost by reducing or eliminating the need for pre-treatment of the material and enable gold recovery via direct cyanide leaching. Depending on the oxidation level and the gold recovery that could be achieved by direct cyanide leaching, reclamation of the stockpile may be more profitable if the pyrite oxidation stage could be fully or partially bypassed. In this paper, we describe the modelling of the pyrite oxidation level in the stockpile using the numerical model reported in our previous work. The characteristics of the stockpile used in the model are the stockpile geometry, the geothermal heat underneath the stockpile, and the properties of the different types of material, including the acid neutralization capacity, rock particle size distribution and pyrite grain size distribution. Limited onsite test results were used to calibrate the model and the final oxidation level over the stockpile was estimated using the calibrated model. Based on the simulation results, it was found that the accessibility to oxygen is the limiting factor for the level of pyrite oxidation when diffusion is the dominant mechanism for oxygen transport within the stockpile. However, experimental tests on samples showed that sufficient oxygen resupply should have been available in the stockpile and therefore there may be air movement mechanisms other than diffusion and thermal-induced air convection onsite. This study also demonstrates that the numerical model can be used to estimate the gold recovery via direct cyanide leaching from the simulated oxidation profile together with the gold distribution in pyrite grains and gold fractions in pyrite of different sizes.

4.1 Introduction

Material containing low-grade commodity metals comprise an important part of the metal resource and recovering metals from these materials to maximise the profit of mining operations has been a significant industry focus for some time. For refractory gold ores that have ultra-fine gold particles encapsulated within the gold-bearing minerals (sulphides), the processing cost is relatively high because of the expensive pre-treatment (such as pressure oxidation (POX), bio-oxidation, roasting or ultrafine grinding) required to liberate the gold particles from sulphide ores for the effective extraction of gold through cyanidation. However, for sulphide refractory ores that have been exposed to oxygen and moisture over a long period of time, the processing cost may be reduced if the metal-bearing sulphides are naturally oxidised. The oxidised material can be directly leached without pre-treatment, thus providing a basis for cheaper recovery of the contained metal. An example application of this approach is the Lihir gold orebody on Aniolam Island in the New Ireland Province of Papua New Guinea, where a 90% or higher gold recovery was achieved by direct cyanide leaching of a small, low-grade oxide resource that was present as a capping over the orebody (Ketcham et al., 1993). This example shows that natural oxidation of the gold-bearing sulphides can facilitate gold extraction at a lower cost by reducing the need for the pre-treatment that is normally required for fresh unoxidized refractory ore. In many refractory gold mining operations, significant amounts of low-grade material may be stockpiled for extensive periods of time for two reasons. First, low-grade ore may be stockpiled to give priority to processing higher grade ores. Second, material that contains low-grade ore may be mined for access to the orebody and be stockpiled for potential processing at a later stage if the metal price increases sufficiently or cheaper processing methods become available. The increasing need for processing low-grade resources, and the fact that exposed sulphides are naturally reactive, has stimulated industry interest in assessing the natural oxidation of sulphides in refractory materials to exploit the potential for more profitable recovery. An important aspect of evaluating this potential is to estimate the extent to which sulphides (mainly pyrite) can be oxidised in natural conditions.

Natural pyrite oxidation has been widely studied as it is a significant contributor to Acid Mine Drainage (AMD). Many laboratory studies have been conducted to investigate pyrite oxidation (León et al., 2004; McKibben and Barnes, 1986; Nicholson et al., 1988; Williamson and Rimstidt, 1994) and numerical models have been developed to predict AMD for the purposes of control and remediation (da Silva et al., 2009; Davis and Ritchie, 1986; Elberling et al., 1994; Lefebvre et al., 2001; Mayer et al., 2002; Molson et al., 2005; Pabst et al., 2017; Walter et al., 1994; Wunderly et al., 1996). These models have demonstrated that numerical modelling can be an effective means of simulating the physical and chemical processes involved in pyrite oxidation in rockpiles. In our previous work (Wang et al., 2019), these studies have been reviewed and a reaction rate model has been developed for the oxidation of pyrite grains, which is then used in a coupled numerical modelling framework developed for the prediction of pyrite oxidation levels in stockpiles under various conditions. Unlike the models developed in the context of AMD, where reactive transport is the focus, the numerical model developed in Wang et al. (2021) focuses on incorporating various influencing factors

(abiotic) affecting the pyrite oxidation rate in order to predict the oxidation level of pyrite under different conditions.

The purpose of this paper is to present a case study in which the pyrite oxidation level in a low-grade refractory gold-bearing stockpile is estimated using the model developed in Wang et al. (2021). The modelled stockpile is the Kapit Flat stockpile at the Lihir Gold Mine on Aniolam Island in Papua New Guinea. The stockpile characteristics considered in the model include the changing geometry of the stockpile during the construction stage, the geothermal heat source under the stockpile and the types of materials within the stockpile. Properties of different types of materials such as pyrite content, rock and pyrite particle size distributions, porosity and diffusivity of intact rocks and the relative acid neutralization capacity are incorporated in the modelling of the volumetric oxygen consumption and the progress of pyrite grain oxidation. Bulk stockpile properties, such as water content and porosity, are estimated from the onsite conditions and previous laboratory test results. The modelled pyrite oxidation level was compared with that measured on samples taken from the stockpile and the differences were used to calibrate the oxygen concentration within the stockpile, which was found to be the most decisive factor for pyrite oxidation. The calibrated model was then used to estimate the level of pyrite oxidation at the block scale and the oxidation profile of pyrite grains for the entire stockpile. This result was used to estimate the potential gold recovery by direct cyanide leaching and to provide input for reclamation scheduling.

4.2 Materials and method

Most input parameters related to the site characteristics required by the model were sourced from existing reports of laboratory tests of materials from the deposit. Some parameters were assumed when relevant information was not available.

4.2.1 Numerical modelling method

The model presented in Wang et al. (2021) is used in this case study for modelling the pyrite oxidation. The physical and chemical processes considered include pyrite oxidation in rock particles, heat transfer, heat-induced air convection and oxygen transport through diffusion and air convection.

Pyrite oxidation in a rock particle

Because of the oxygen concentration gradient within a rock particle, the oxidation of pyrite grains may differ depending on the depths of the grains from the rock particle surface. This is a diffusion-reaction process that can be described by the diffusion-reaction equation using the polar coordinate system given in Eq. (4-1), where C is the oxygen concentration inside the rock particle as a function of the radial coordinate r and time t; φ_r and D_e are the porosity and oxygen diffusion coefficient of the rock particle respectively; and S_{py} is the sink term representing the oxygen consumption by pyrite grains inside the rock particle. The term S_{py} depends on both the oxygen concentration C, which is solved by Eq. (4-1), and the reaction progress of the pyrite grains at that radial location.

$$\varphi_r \frac{\partial C}{\partial t} = D_e \left(\frac{\partial^2 C}{\partial r^2} + \frac{2}{r} \frac{\partial C}{\partial r} \right) - S_{py} \tag{4-1}$$

For a single pyrite grain, the reaction can be described by different reaction rate models under different reaction conditions. For reactions under circum-neutral to alkaline conditions and/or low-water-content conditions, diffusion barriers, such as the oxidised layer (an iron hydroxide coat) or a thin saturated solution film, can develop on the surface of the pyrite grain, which subsequently inhibits the diffusion of oxygen to the fresh pyrite layer (Wang et al., 2019) . For this case, the reaction rate model derived by Wang et al. (2019) is used to model the reaction progress controlled by both diffusion and reaction for the pyrite grain. For reactions under acidic and intro-aqueous conditions, the reaction products are dissolved and diluted in the pore-water and thus neither a solid coating nor a concentrated/saturated solution film is formed on the pyrite surface. Hence the reaction rate is controlled only by the surface reaction and the corresponding reaction rate model should be used for this case.

The sizes of pyrite grains in a rock particle are important influencing factors for the overall oxidation rate. For the same pyrite content, the smaller the grain sizes, the higher the overall reaction rate of the pyritic rock particle due to larger pyrite surface area. To consider the effect of pyrite grain size distribution, Wang et al. (2021) proposed a rate formula for a group of pyrite grains of different sizes. Assuming the pyrite grain size distribution shown in Eq. (4-2), defined by n size categories, the oxygen consumption rate of the pyrite group with a total mass of $\sum_{i=1}^{n} m_i$ can be approximated by Eqs. (3-7) and (3-8) respectively for reactions with and without a diffusion barrier formed during the reaction (Wang et al., 2021).

$$PSD_{py} = \begin{pmatrix} R_1 & R_2 \dots R_i \dots R_n \\ m_1 & m_2 \dots m_i \dots m_n \end{pmatrix}$$
$$F_i = \frac{m_i}{\frac{4}{3}\pi R_i^3 \cdot \rho_{py}} \tag{4-2}$$

$$\begin{cases} RateO_{gp} = \sum_{i=1}^{n} \left[\dfrac{4\pi R_i^2 \cdot C_e(r)}{\frac{R_i}{D_s}\left(\frac{R_i}{r_c(i)} - 1\right) + \frac{1}{k''}\frac{R_i^2}{r_c(i)^2} C_e(r)^{0.5}} \cdot F(i) \right] \\ -\dfrac{dr_c}{dt} = \dfrac{bC_e(r)/\rho_B}{\frac{(R_n - r_c)r_c}{R_n D_s} + \frac{C_e(r)^{0.5}}{k''}} \\ r_c(i) = max\{0, R_i - (R_n - r_c)\} \end{cases} \tag{4-3}$$

$$\begin{cases} RateO_{gp} = \sum_{i=1}^{n} [\dfrac{4\pi R_i^2 \cdot C_e(r)}{\dfrac{1}{k''} \cdot \dfrac{R_i^2}{r_c(i)^2} \cdot C_e(r)^{0.5}} \cdot F(i)] \\ -\dfrac{dr_c}{dt} = \dfrac{b \cdot C_e(r)/\rho_B}{\dfrac{C_e(r)^{0.5}}{k''}} \\ r_c(i) = max\{0, R_i - (R_n - r_c)\} \end{cases} \quad (4\text{-}4)$$

In Eqs. (4-2), (3-7) and (3-8), R_i and m_i are the radius and the mass proportion of the ith grain size respectively. F_i is the number of pyrite grains of size R_i in a pyrite group with a total mass of $\sum_{i=1}^{n} m_i$. $RateO_{gp}$ is the oxygen consumption rate of the pyrite group at the radial location r inside a rock particle. $C_e(r)$ is the effective oxygen concentration depending on the degree of water saturation. r_c is the simulated unreacted core radius of pyrite of grain size R_n and $r_c(i)$ is the unreacted core radius of the pyrite grain size R_i which is estimated from r_c. ρ_B is the molar density of pyrite and b is the stoichiometric coefficient given as the mole ratio of reacted pyrite to consumed oxygen. D_s is the diffusion coefficient of oxygen through the diffusion barrier developed during the reaction and k'' is the surface reaction rate constant of pyrite. According to Wang et al. (2019), the values of D_s and k'' depend on the degree of water saturation, S_w, and the temperature, T. The effective oxygen concentration C_e also depends on the degree of water saturation, S_w. Their values are given as Eq. (4-5) in Wang et al. (2019), where D_s^0 and k_0'' are the values of D_s and k'' at the reference temperature T_0, E_a^D and E_a^k are the activation energies for diffusion and surface reaction respectively, T is the reaction temperature in Kelvin, $\bar{R}$ is the gas constant, H^{cc} is the Henry's law solubility and C_g is the oxygen concentration in gas phase which is solved using Eq. (4-1).

$$\begin{cases} C_e = C_g \cdot e^{\log(H^{cc}) \cdot S_w} \\ D_s = D_s^0 \cdot e^{\frac{-E_a^D}{\bar{R}}(\frac{1}{T} - \frac{1}{T_0})} \\ k'' = k_0'' \cdot e^{\frac{-E_a^k}{\bar{R}}(\frac{1}{T} - \frac{1}{T_0})} \end{cases}$$

For T_0 = 293.15 K: (4-5)

$$\begin{cases} D_s^0 = 1.2 \times 10^{-15} & (for\ S_w \geq 25\%) \\ D_s^0 = 4.82 \times 10^{-15} \cdot \theta_w - 4.35 \times 10^{-18} & (for\ 0.1\% \leq S_w < 25\%) \\ k_0'' = 5 \times 10^{-8} \\ H^{cc} = 0.0353 \end{cases}$$

The oxygen consumption rate at different radial locations in the rock particle (S_{py}) is given in Eq. (3-9) where $Py\%$ is the volumetric pyrite content. The reaction progress is known from the unreacted core radius $r_c(i)$ for pyrite grains of different sizes and at different radial locations in the rock particle, as discussed above.

$$S_{py} = RateO_{gp} \cdot \frac{Py\%}{\frac{4}{3}\pi \sum_{i=1}^{n}(R_i^3 \cdot F_i)} \tag{4-6}$$

Overall pyrite oxidation within a unit volume of the stockpiled materials

Rocks in a stockpile can range from very fine particles to very blocky fragments and the progress of pyrite oxidation will differ across the size range. The rock particle size distribution can be defined generally using a non-parametric form as shown in Eq. (4-7) with m categories of sizes, where $R_{rock}(j)$ is the average radius of rock particles in category j and $m_{rock}(j)$ is the mass proportion of rock particles in that size category. $F_{rock}(j)$ is the number of particles for the category among rocks of a total mass of $\sum_{j=1}^{p} m_{rock}(j)$. This distribution can be quantified by measuring rock sizes in the stockpile directly or indirectly using photogrammetry or laser scanning. For a unit volume of the stockpiled materials with different rock particle sizes, the overall volumetric oxygen consumption rate $RateO_{vo}$ is given in Eq. (3-11) (Wang et al., 2021).

$$PSD_{rock} = \begin{pmatrix} R_{rock}(1) & R_{rock}(2) \dots & R_{rock}(j) & \dots R_{rock}(p) \\ m_{rock}(1) & m_{rock}(2) \dots & m_{rock}(j) & \dots m_{rock}(p) \end{pmatrix}$$

$$F_{rock}(j) = \frac{m_{rock}(j)}{\frac{4}{3}\pi R_{rock}^3(j) \cdot \rho_{rock}} \tag{4-7}$$

$$RateO_{vo} = \sum_{j=1}^{p} (RateO_{gp}(k) * \frac{Py(k)}{\frac{4}{3}\pi \sum_{i=1}^{n}(R_i^3 \cdot F_i)})$$

$$\begin{cases} Py(k) = \dfrac{Py\% \cdot \sum_{j=1}^{p}[\frac{4}{3}\pi \cdot (r_{kj(1)}^3 - r_{kj(2)}^3) \cdot F_{rock}(j)]}{\frac{4}{3}\pi \sum_{j=1}^{p}\left(R_{rock}^3(j) \cdot F_{rock}(j)\right)} \\ r_{k,j(1)} = \max\{R_{rock}(j) - \Delta r \cdot (k-1), 0\} \\ r_{k,j(2)} = \max\{R_{rock}(j) - \Delta r \cdot k, 0\} \end{cases} \tag{4-8}$$

Eq. (3-11) is derived on the assumption that the oxidation of pyrite in rock particles depends on the distance of the pyrite grains to the nearest void space between rock particles as this distance determines the accessibility to oxygen. Based on this assumption, within a unit volume of the stockpiled material, the oxidation of pyrite grains in different rock particles is the same if their distance to the void space (i.e., to the surface of the rock particles) is the same. In Eq. (3-11), k denotes the sequence of discrete layers in the largest rock particle with $k = 1$ representing the outermost layer and thus it represents the distance to the void space (particle surface). Using this representation, pyrite oxidation at different radial locations inside rock particles of different sizes can be estimated using the same layer sequence k. The

oxidation rate of a pyrite group in layer k is $RateO_{gp}(k)$, which is given by Eq. (3-7) or (3-8), and the pyrite volume fraction for layer k in all rock particles is calculated as $Py(k)$ from the rock particle size distribution. In Eq. (3-11), $r_{kj(1)}$ and $r_{kj(2)}$ are the outer and inner radius respectively of layer k in a rock particle of size $R_{rock}(j)$ and Δr is the uniform layer thickness. Based on these equations, the pyrite oxidation in the unit volume at a location within a stockpile can be calculated by simulating the diffusion-reaction process of only the largest rock particle using Eq. (4-1).

Oxygen transport in the stockpile

The transport of oxygen in the stockpile is given by Eq. (3-13), where U is the oxygen concentration in the void space within the stockpile, φ is the stockpile porosity, D_b is the oxygen diffusion coefficient in the stockpile, $\boldsymbol{v}$ is the air velocity field and q_{O_2} is the source term from the reaction and has a non-positive value.

$$\frac{\partial}{\partial t}(\varphi U) = \nabla(D_b \cdot \nabla U) - \nabla \cdot (\boldsymbol{v} \cdot U) + q_{O_2} \tag{4-9}$$

The diffusion coefficient is calculated from the temperature value and the water content using Eq. (3-15) derived in Wang et al. (2021).

$$D_b = \frac{1}{\theta_s^2}(1.1005 \times 10^{-5} \cdot T^{1.726}\theta_a^{3.3} + 10^{-7} \times (0.0058T^2 - 2.146T + 163.35)\theta_w^{3.3}) \tag{4-10}$$

The source term q_{O_2} is the volumetric oxygen consumption rate and is given in Eq. (4-11):

$$q_{O_2} = -RateO_{vo} \tag{4-11}$$

The heat-induced air velocity can be calculated from the temperature and pressure profile within the stockpile. The partial differential equation for the pressure profile, as given in Eq. (4-12), was derived in Wang et al. (2021) based on mass conservation, the ideal gas law and Darcy's law for air flow in porous media. The air velocity is then given by Darcy's Law as Eq. (4-13). In these two equations, B is the square of the pressure P, P_0 is a reference pressure known from the ambient environment, κ is the air permeability of the stockpile, μ is the air viscosity, M is the molar mass of air, $\bar{R}$ is the gas constant, $\boldsymbol{g}$ is the gravitational acceleration and T is the absolute temperature obtained by solving the heat transfer equation.

$$\frac{\partial B}{\partial t} = \alpha \cdot \nabla^2 B + \boldsymbol{\beta} \cdot \nabla B + \theta \cdot B$$

$$\alpha = \frac{\kappa P_0}{\varphi \mu}$$

$$\begin{cases} \beta_x = -\dfrac{\kappa P_0}{\varphi \mu} \cdot \dfrac{1}{T} \dfrac{\partial T}{\partial x} \\ \beta_y = -\dfrac{\kappa P_0}{\varphi \mu} \cdot \dfrac{1}{T} \dfrac{\partial T}{\partial y} \\ \beta_z = -\dfrac{\kappa P_0}{\varphi \mu} \dfrac{1}{T} \cdot \left(\dfrac{\partial T}{\partial z} + \dfrac{2M\boldsymbol{g}}{\bar{R}}\right) \end{cases} \tag{4-12}$$

$$\theta = \frac{2}{T} \frac{\partial \mathrm{T}}{\partial \mathrm{t}} + \frac{\kappa P_0}{\varphi \mu} \frac{4M\boldsymbol{g}}{\bar{R}} \frac{1}{T^2} \frac{\partial T}{\partial z}$$

$$P = B^{1/2}$$

$$\boldsymbol{v} = -\frac{\kappa}{\mu}(\nabla P - \rho \boldsymbol{g}) \tag{4-13}$$

Temperature profile in the stockpile

The temperature profile is given by Eq. (3-16), where T is the temperature of the stockpile, $\boldsymbol{v}$ is the velocity field of air, D_h is the thermal diffusivity of the stockpile, ρ and C are respectively the density and the specific heat capacity of the stockpile material and ρ^* and C^* are those of the air. The source term q_h is the heat flux generated from pyrite oxidation.

$$\frac{\partial T}{\partial t} = \nabla \cdot (-\gamma \boldsymbol{v} T + D_h \nabla T) + \frac{q_h}{(\rho C)} \qquad \text{with} \qquad \gamma = \frac{\rho^* C^*}{(\rho C)} \tag{4-14}$$

The volumetric heat generation rate q_h is calculated by Eq. (4-15) where δ is the heat produced per mole of pyrite oxidised and b is as defined in Eq. (3-8).

$$q_h = \delta \cdot b \cdot RateO_{vol} \tag{4-15}$$

Integrated modelling framework

The relationships described above are the governing equations for modelling the pyrite oxidation in stockpiles. In this study, a finite difference scheme, the Douglas-Gunn method, is used to solve the partial differential equations (Eqs. (3-13), (4-12) and (3-16)) based on the 3D stockpile geometry. Instead of following the numerical solution strategy described in Wang et al. (2021), a sequential non-iterative approach is used in this work to reduce the computational cost. The spatial grid sizes for the x, y and z directions used in the simulation are 10 m, 10 m and 12 m, respectively, resulting in a total of 21,452 blocks/node points that have to be calculated for the final stockpile geometry. As the rate of oxygen consumption by

pyrite is relatively high compared with that of the oxygen bulk transport and heat transfer over the stockpile, different time steps are used in the simulation for pyrite oxidation and other processes. In general, for modelling the pyrite oxidation in rock particles, the time step is adjusted dynamically depending on the reaction rate during the simulation and for other processes a time step of one day is used. The typical run time using a 32-core, 64GB-memory cluster with parallel programming is around 80 hours for a 20-year simulation timeframe.

4.2.2 Site characteristics and model inputs

The gold-bearing refractory stockpile in this study is the Kapit Flat stockpile at the open-cut gold mine on Aniolam (also known as Lihir) Island in Papua New Guinea, owned and operated by Newcrest Mining Limited since August 2010. Stockpiled material at Lihir is classified as a Measured Mineral Resource with a total of approximately 83Mt at 1.9 g/t gold as at December 2019 (Newcrest 2019 Resources and Reserves, 2020). The Kapit Flat stockpile, which is modelled in this study, is the largest of several stockpiles. Gold in the Lihir orebody is mainly present as solid solution gold within pyrite and is thus classified as refractory and resistant to recovery by standard cyanidation and carbon adsorption processes. Oxidation of the sulphide minerals is therefore required to release the gold particles before effective gold extraction by cyanidation, which uses the pressured oxidation (POX) as the pre-treatment method at Lihir Mine. The average sulphur grade of the stockpiled material is around 6% and the main sulphide mineral is pyrite. More details about the Lihir deposit can be found in the recent technical report released by Newcrest (e.g. Gleeson et al. (2020)).

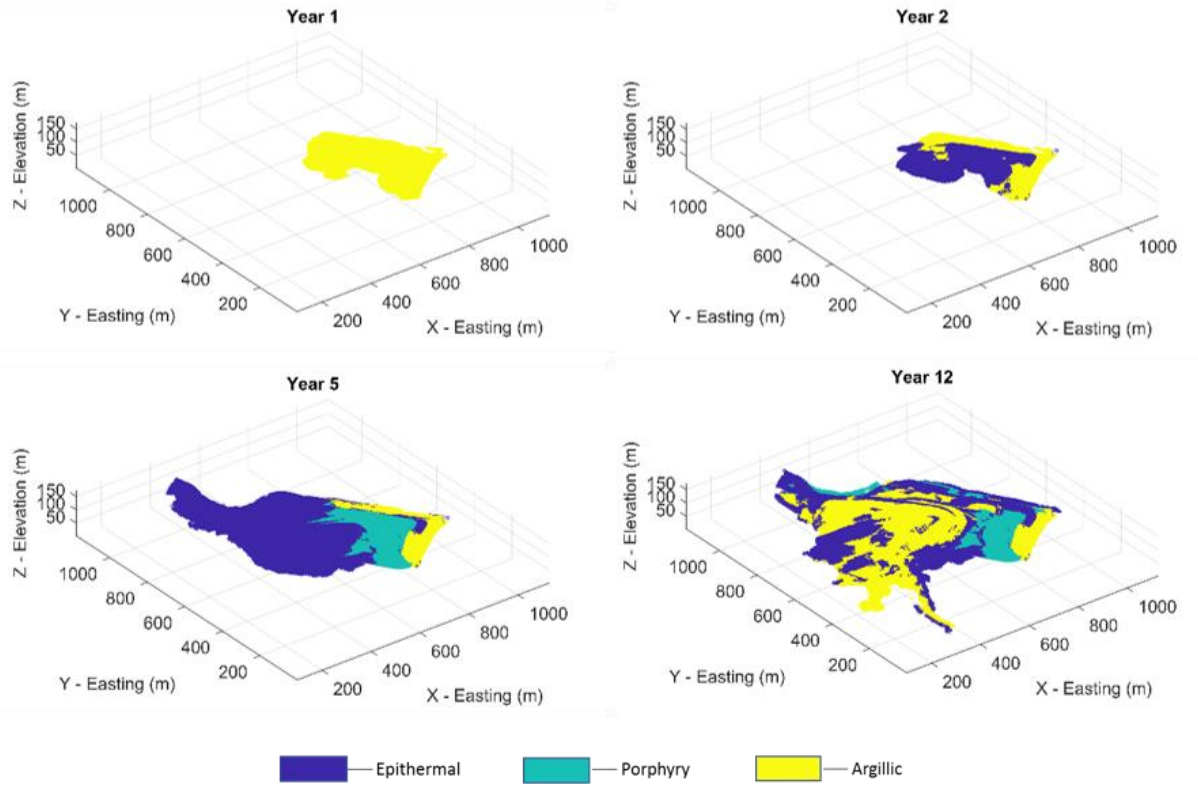

Fig. 4-1: The shape and spatial distributions of materials of the stockpile at years 1, 2, 5 and 12

The Kapit Flat stockpile is located near the open pit and has a maximum footprint of about 25 hectares and a height of up to 60 m. The stockpile commenced in 1998 and since then new material has been mined and dumped from time to time until 2010 (Gardner, 2018a). The size and shape of the stockpile changed over the twelve-year period and different areas of the stockpile had different exposure histories to the atmosphere, which is believed to have affected the oxidation at different locations within the stockpile.

By way of example, Fig. 4-1 shows the shape of the stockpile at years 1, 2, 5 and 12 respectively. The materials making up the stockpile are categorised as three types: porphyry, epithermal and argillic, using an "alteration domain" classification based on geology, mineralization and metallurgy. The spatial distributions of the three types of materials are shown in Fig. 4-1 using different colours.

The input variables for pyrite oxidation modelling of the Kapit Flat stockpile include the degree of water saturation, bulk porosity of the stockpile, boundary temperature conditions including the geothermal heat, rock particle size distribution, pyrite grain size distribution, the acid buffering ability of the materials and the porosity and diffusivity of intact rocks. Many of these properties depend on the type of material. Although the values of these parameters were not measured specifically for this study, some previous laboratory test results were available to provide reference values for this study.

Laboratory test results for samples from run of mine blast waste were used to estimate the relevant properties of the stockpiled materials. The tests suggested that the bulk porosity of the samples is around 30% to 40% with a maximum particle size of 37.5 mm, and the intrinsic permeability ranges from 8×10^{-16} to 4×10^{-10} m^2. Thus, in the case study, the value of 40% is used for the stockpile porosity and 10^{-12} m^2 for the permeability for air flow. The test results also suggested that the samples have a thermal conductivity between 1 and 1.4 W/m/°C under saturated conditions and 0.1 and 0.8 W/m/°C under dry conditions with a moisture content (by volume) between 4% and 9%, hence the value of 1 W/m/°C is used for the stockpile in this model. For the water content, it is believed that the stockpile has remained partially saturated as the climate on the island is very humid with abundant rainfall and efficient water runoff drainage has been maintained to avoid ponding. The simulation therefore uses a water saturation of 25% as the average condition for the simulation period.

A previous laboratory study was conducted to investigate the potential for acid rock drainage (ARD) from any long-term stockpiling of low-grade sulphide ore and the column test results can be found in Doyle et al. (2003). Four column tests lasting from 56 to 224 days were conducted and it was observed that the dissolution of pyrite was accompanied by the dissolution of the acid buffering minerals such as calcite and orthoclase together with the precipitation of jarosite and iron oxide. The measured and theoretical acid consumption based on the column leaching results and the assumed reaction stoichiometry indicate that all columns except column four were acid consuming. These tests indicate that the stockpiled material, which is known to contain acid buffering minerals, is likely to undergo pyrite oxidation in a non-acidic environment for a long initial period, after which the net acid generation may become positive if the buffering minerals are consumed while pyrite remains.

The length of this initial period depends on the amount of contained pyrite and the acid buffering minerals, which vary for different types of materials. This variation with types of materials can be seen from the pH values measured before and after the cyanide leaching tests conducted on samples of different types of materials. The final pH values after the cyanide leaching were around 3, 5 and 7 for the sample materials of argillic, epithermal and porphyry respectively (Gardner, 2018b), indicating that, on average, the acid buffering capacity increases in the order of argillic > epithermal > porphyry. An assumed factor representing the relative acid neutralization capacity (F_ANC) is used for the estimation of the pH value in the simulations conducted in this work. The formula used to estimate the pH value is given in Eq. (4-16), where the generated acid is calculated from the oxidation level $OxiLevel$, pyrite content $Py\%$ and the neutralization factor F_ANC; ρ_B is the pyrite molar density and φ is the stockpile porosity. The values of F_ANC are set to 1, 2 and 4 for argillic, epithermal and porphyry materials respectively to account for their relative acid neutralisation capacity. The pH value calculated by Eq. (4-16) for each time step determines which reaction rate model (with or without coating) should be used for pyrite oxidation in each block.

$$pH = -\log_{10}(2 \cdot OxiLevel \cdot Py\% \cdot \rho_B / \varphi / 1000 / F\_ANC) \tag{4-16}$$

The distributions of rock particle size and pyrite grain size were measured for the three types of materials and the results are shown in Fig. 4-2 and Fig. 4-3. As can be seen from Fig. 4-2, the rock particle size distributions differ slightly among the three types of materials, with the porphyry materials being the blockiest. The pyrite grain size decreases in the order of argillic > porphyry > epithermal materials.

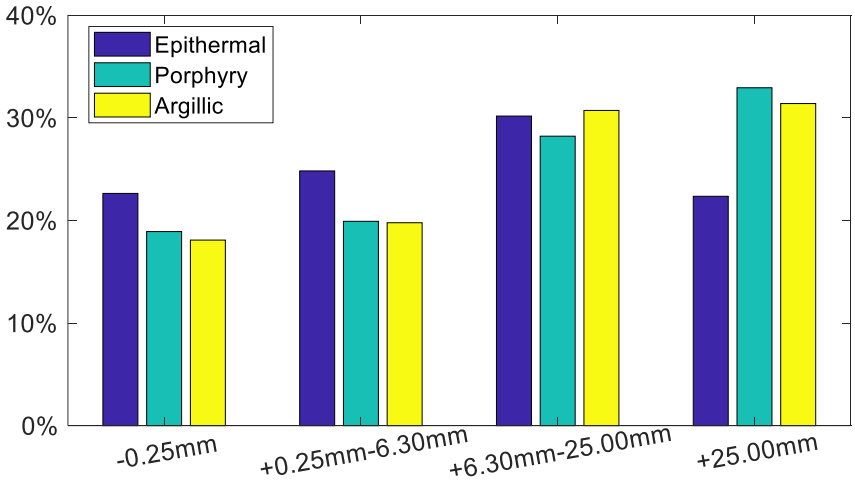

Fig. 4-2: Rock particle size distribution (by mass) for epithermal, porphyry and argillic materials

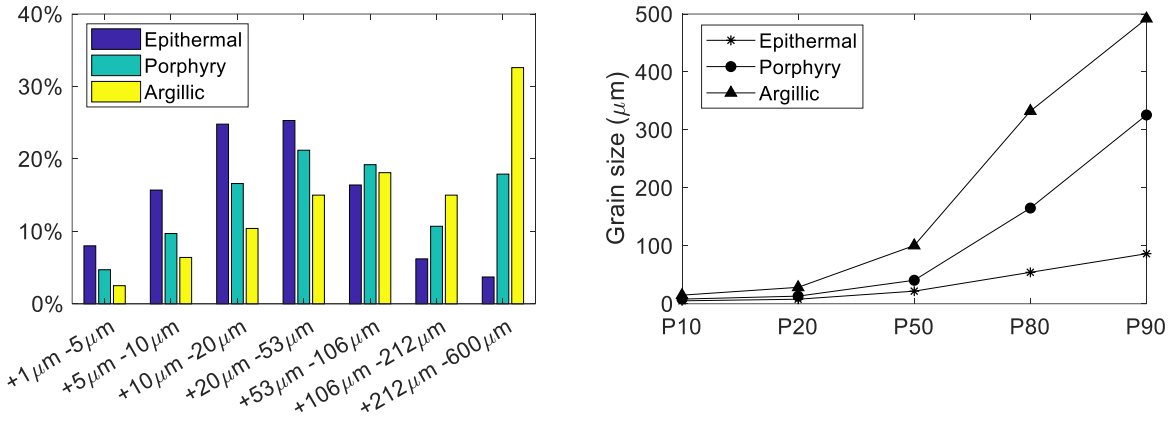

Fig. 4-3: Pyrite grain size distribution for the three types of materials; left: relative mass distributions, right: the grain sizes of P10, P20, P50, P80 and P90 for the three types of materials

The porosity and diffusivity inside the rock particles are believed to vary for the three types of materials. As measured data are not available, these values are estimated from those measured for other types of rocks as published in the literature. Fig. 4-4 shows sample photos of the epithermal, porphyry and argillic materials. The porosity of these materials is estimated to be 0.09, 0.15 and 0.3 respectively from the measured values for dolomite, sandstone and mudstone in Peng et al. (2012) where similar rock structures were observed. The gas diffusion coefficients in the rocks used in the simulations are 10^{-10}, 5×10^{-10} and 8×10^{-10} m^2/s respectively.

Fig. 4-4: Sample photos for epithermal, porphyry and argillic materials

Studies have shown that impurities, such as arsenic within the pyrite crystal structure, can increase the reactivity of pyrite (Lehner and Savage, 2008; Lehner et al., 2007). Arsenic is the most common impurity identified in Lihir pyrites and evidence has shown that pyrite with higher arsenic content appears to oxidise more readily than that with lower content. The average arsenic contents in the three different types of materials are different, with epithermal pyrite being the highest (1320 ppm) followed by porphyry pyrite (830 ppm) and argillic pyrite (600 ppm). To account for the difference in pyrite reactivity of different types of

materials, adjustment factors of 2, 1.25 and 1 were applied to modify the oxidation rate in our simulations for the epithermal, porphyry and argillic pyrite respectively.

The Kapit Flat stockpile is situated over a main heat source of an active geothermal area and the temperature below the surface is higher than that of the atmosphere. In 2017, several holes were drilled and the temperatures logged in them were up to 70°C at a depth of around 80 m. A constant temperature boundary condition of 70°C in the case study model is thus set at, and beyond, a depth of 84 m. In other words, for the simulation of temperature, the modelled region includes the stockpiled material and the ground directly beneath it to a depth of 84 m with a constant bottom boundary temperature set at 70°C.

To summarise, the value of all parameters related to the stockpile materials are given in Table 3-1, Table 3-2 and Table 4-3. All other parameters used in the simulations are listed in Table 4-4.

Table 4-1: Rock particle size distribution (by mass) for different types of materials

Rock particle size (mm) bin		+25	-25 +6.3	-6.3 +0.25	-0.25
Average size used for simulation (diameter)		50	15.65	3.275	0.25
Mass dist. (%)	Epithermal	22.36	30.18	24.83	22.64
	Porphyry	32.94	28.22	19.92	18.92
	Argillic	31.4	30.73	19.78	18.09

Table 4-2: Pyrite grain size distribution for different types of materials

Pyrite grain size (µm) bin		-600 +212	-212 +106	-106 +53	-53 +20	-20 +10	-10 +5	-5 +1
Average size used for simulation		406	159	79.5	36.5	15	7.5	3
Mass dist. (%)	Epithermal	3.7	6.2	16.4	25.3	24.8	15.7	8
	Porphyry	17.9	10.7	19.2	21.2	16.6	9.7	4.7
	Argillic	32.6	15	18.1	15	10.4	6.4	2.5

Table 4-3: Parameters used in the simulations for different types of materials

Parameters	Epithermal	Porphyry	Argillic
Porosity	0.09	0.15	0.3
Diffusion coefficient (m^2s^{-1})	10^{-11}	5×10^{-11}	8×10^{-11}
Pyrite content	5%	3%	10%
ANC factor	2	4	1
Pyrite reactivity factor	2	1.25	1

Table 4-4: Other parameters used in modelling the pyrite oxidation of the Kapit Flat stockpile

Parameters	Value	Unit
Porosity of the stockpile	0.4	
Air permeability of the stockpile	10^{-12}	m^{-2}
Degree of water saturation of the stockpile	25%	
Temperature boundary value at depth of 84 m	70	°C
Stoichiometric coefficient of pyrite reaction	2/7	Pyrite to oxygen
Pyrite molar density ρ_B	4.17×10^4	$mol\cdot m^{-3}$
Gravitational acceleration g	-9.8	$m\cdot s^{-2}$
Reference air density ρ	1.165	$kg\cdot m^{-3}$
Gas constant $\bar{R}$	8.314	$Pa\cdot m^3\cdot mol^{-1}\cdot K^{-1}$
Henry's law constant H^{cc}	3.2×10^{-2}	@ 25 °C
Specific heat capacity of air C_g	1006.1	$J\cdot K^{-1}\cdot kg^{-1}$
Volumetric heat capacity of rock media	1.98×10^6	$J\cdot K^{-1}\cdot m^{-3}$
Heat generated per mole of pyrite reacted	1.409×10^6	$J\cdot mol^{-1}$
Heat diffusivity of the stockpile material	1.4×10^{-6}	$m^2\cdot s^{-1}$
Initial O_2 concentration C in air	8.28	$mol\cdot m^{-3}$
Initial and reference pressure P_0	1	atm
Initial and atmosphere temperature T_0	25	°C

4.2.3 Sample test results

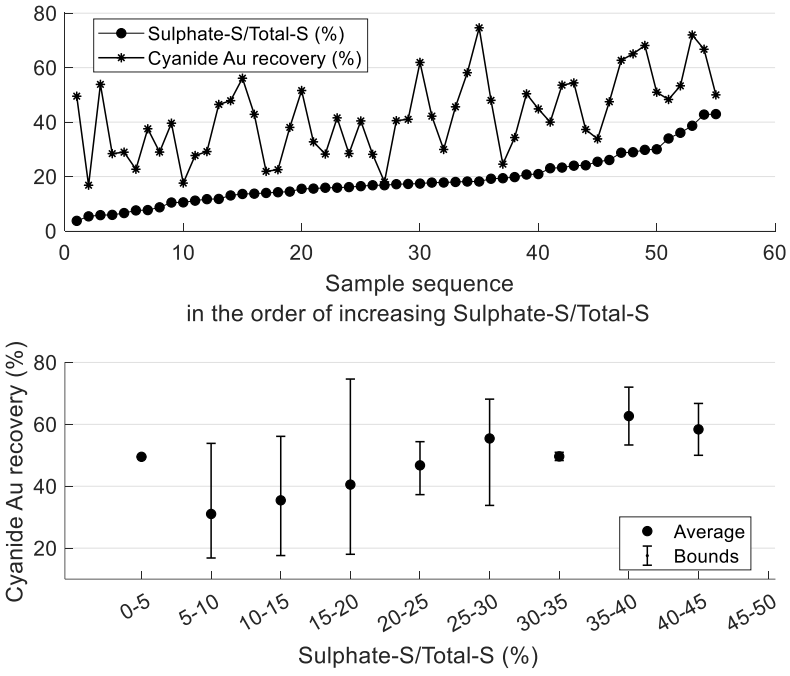

Fig. 4-5: The pyrite oxidation level and gold recovery by direct cyanide leaching for samples taken from the Kapit Flat stockpile

In 2017, sonic drill holes were drilled in the Kapit Flat stockpile and 55 samples were taken. These samples were then analysed in the laboratory, where the sulphur content in sulphate and sulphide forms were measured as well as the gold recovery by direct cyanide leaching.

Fig. 4-5 shows the gold recovery after direct cyanide leaching and the oxidation level calculated as the ratio of sulphate sulphur to total sulphur. These test results are used to calibrate the numerical model.

4.3 Results and discussion

4.3.1 Estimation of oxidation level

Pyrite oxidation over the Kapit Flat stockpile was simulated for the period of twenty years after it was first constructed. The cross-sections in Fig. 4-6 and Fig. 4-7 show the simulated results for the variables including the final oxidation level, oxygen concentration, temperature and air velocity field at Year 20.

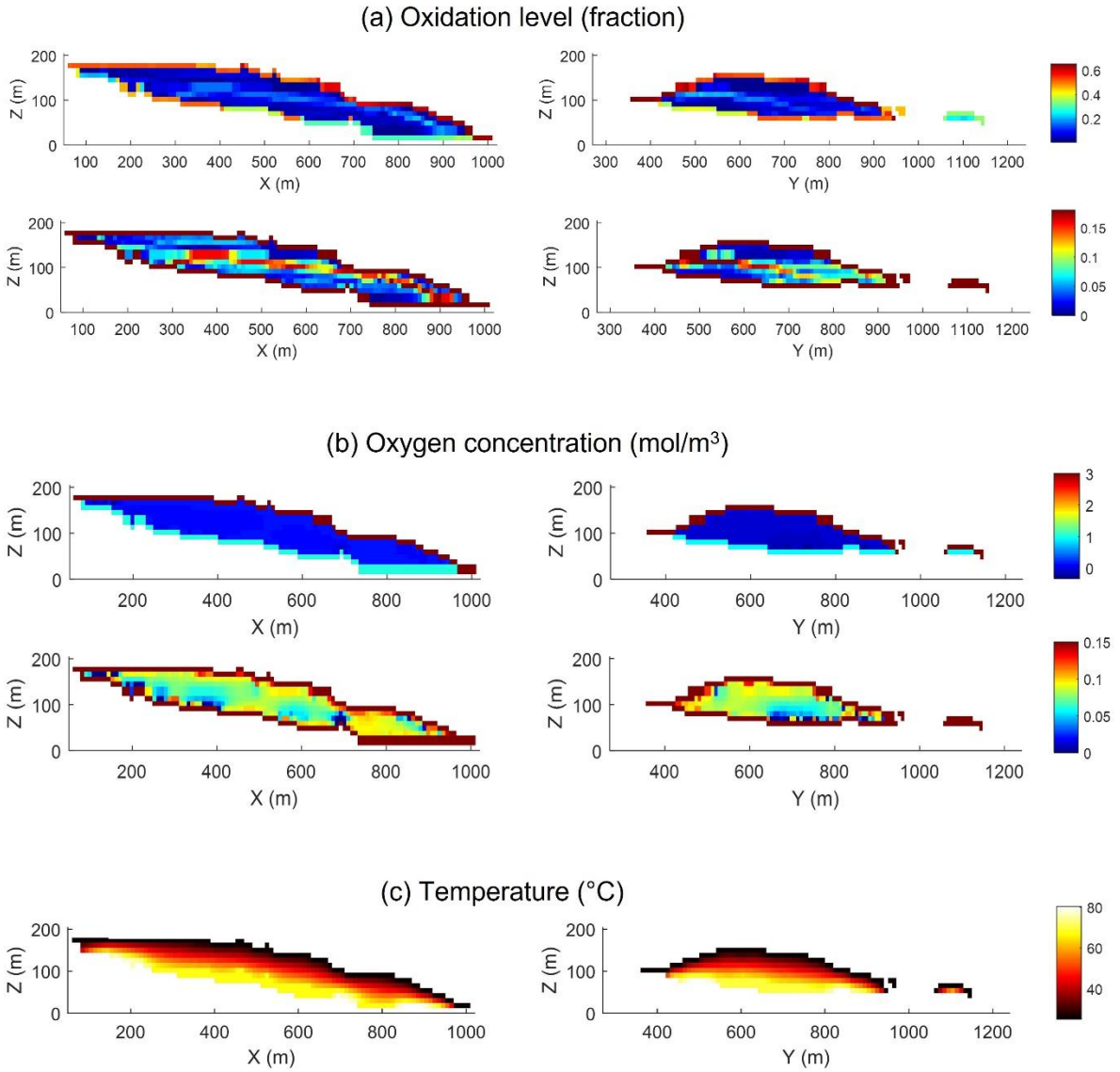

Fig. 4-6: Simulated results for the Kapit Flat stockpile at the 20th year: (a) Oxidation level; (b) Oxygen concentration; (c) Temperature; left: cross sections at Y = 610 m; right: cross sections at X = 540 m

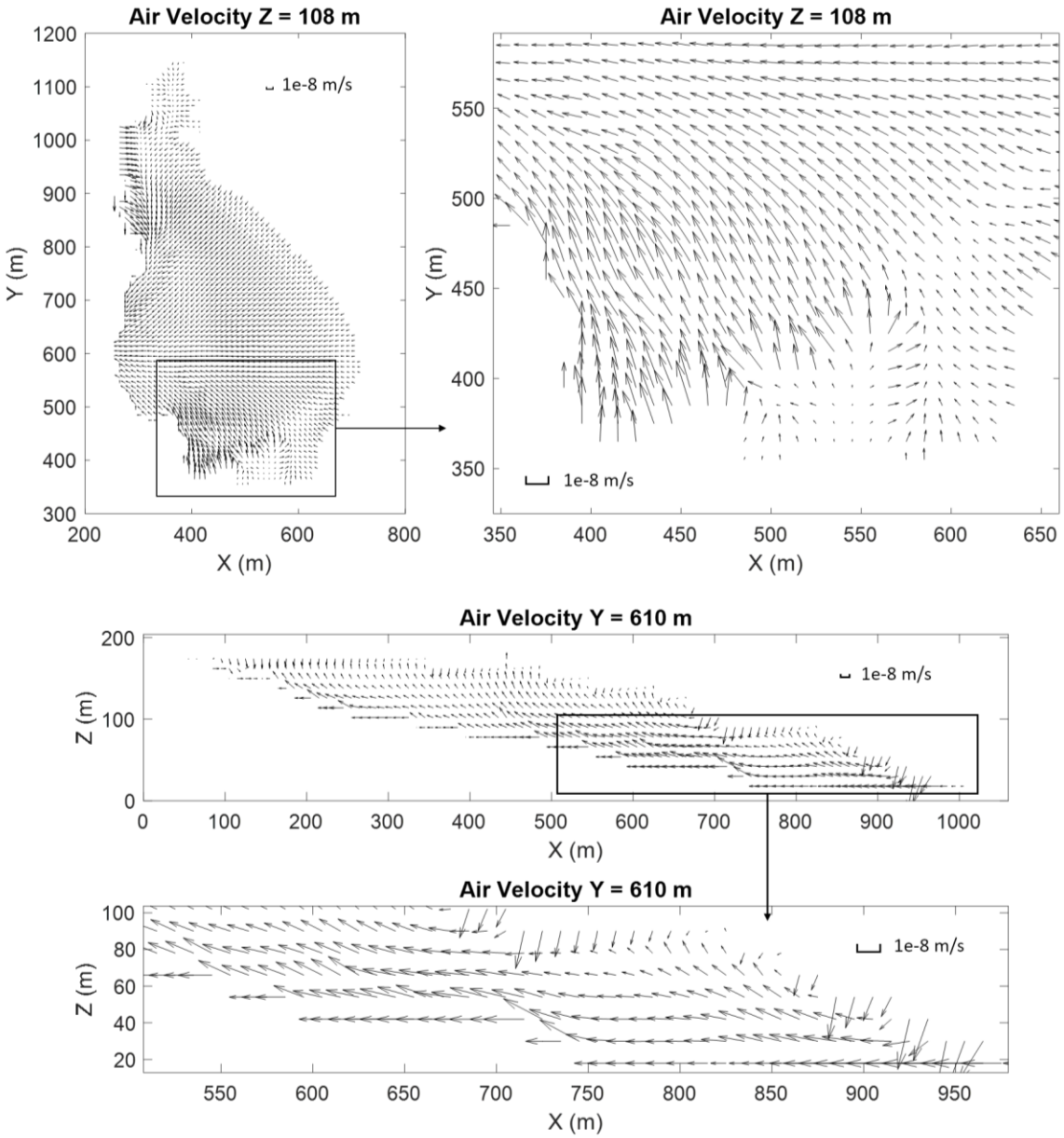

Fig. 4-7: Simulated air velocity field over the Kapit Flat stockpile at the 20th year

As can be seen in Fig. 4-6a, the simulated oxidation level over the Kapit Flat stockpile varies from less than 0.1 to as high as 0.7. It is much higher at the boundaries including both the bottom and the surface, while the oxidation level is mostly less than 0.2 within the stockpile away from boundaries. This can also be seen in Fig. 4-8 where the histograms of the oxidation level for blocks at the surface-boundary, bottom-boundary and non-boundary locations are plotted. The significant differences among the three categories are apparently caused by the differences in oxygen concentrations, which can be seen in Fig. 4-6b. Constant values of 1 $mol \cdot m^{-3}$ and 3 $mol \cdot m^{-3}$ of oxygen concentrations were used as the first-type boundary conditions for the blocks at the bottom and the surface of the stockpile respectively. These conditions provide enough oxygen for pyrite oxidation at the boundary locations, resulting in high oxidation levels. Inside the stockpile, while the simulated oxygen concentration varies across the stockpile, it is rarely above 0.15 $mol \cdot m^{-3}$ at non-boundary locations as a result of

fast consumption of oxygen relative to the resupply rate. Consequently, among the blocks at the non-boundary locations, the oxidation level ranges from almost no oxidation to 20%, with a few blocks reaching higher levels of up to 40%. The major cause of this small variation is not due to material properties such as reactivity or pyrite content. Instead, it is a result of the varying sizes and shapes of the stockpile during the 12 years of intermittent stockpiling. As oxygen is always limited at locations other than the boundaries, the time of exposure to the atmosphere during the stockpile construction is the key influencing factor for the oxidation level for non-boundary blocks. Overall, for a stockpile of this size, the accessibility to oxygen is the most dominant decisive factor that determines the level of pyrite oxidation.

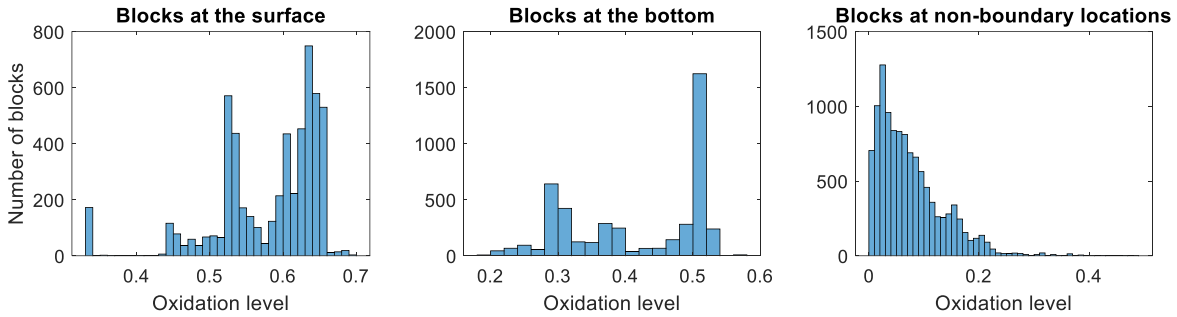

Fig. 4-8: The distribution of oxidation levels for blocks at different locations

Fig. 4-6c shows the temperature profile which mainly follows the topography of the stockpile, gradually increasing from the surface to the deeper locations. As heat has been generated from pyrite oxidation, at some locations in the stockpile the temperature can be higher than the geothermal-boundary temperature (set at 70°C). The temperature has reached a maximum of 89°C at a depth of 60 m. Fig. 4-7 shows the heat-induced air velocity field over the stockpile. As can be seen, air can be recharged into the stockpile. However, the magnitude of the air velocity is only up to 8 mm/day, which is insignificant for oxygen resupply compared with diffusion as discussed in Wang et al. (2021). In this case, although the increased temperature can enhance the oxidation rate in general, it is a less important factor compared with the accessibility to oxygen.

Fig. 4-9 shows a comparison between the simulated oxidation levels and those obtained from the sample tests. The samples were taken at different depths of the sonic drill holes drilled in 2017 and were then tested in the laboratory for sulphide and sulphate content. The oxidation level is calculated as the ratio of sulphate sulphur to total sulphur. The comparison shows that the current model underestimates the oxidation level by nearly 20% at most sample locations. It also significantly overestimates the oxidation level at some locations near the bottom and surface boundaries. As discussed above, oxygen concentration is the most decisive factor among all the influencing variables. The mismatch between the simulated results and the test results indicates that the simulated oxygen concentrations and the boundary values may deviate from the actual values. The boundary values set at the bottom or surface boundaries for oxygen concentration seem to be too high although considering oxygen consumption, they were set to be much smaller than the atmospheric concentration (8 mol·m^{-3}). At non-boundary locations, the simulated oxygen concentrations appear to be too small to yield oxidation levels comparable to the tested samples. This further indicates that, in addition to

the modelled diffusion and heat-induced convection, there must be other sources and/or mechanisms for oxygen resupply inside the stockpile, such as natural air flow, barometric pressure fluctuation and rainwater infiltration. In this case in particular, rainwater infiltration has possibly played a significant role for oxygen resupply. Although the low solubility of oxygen in water limits the amount of dissolved oxygen entering the stockpile in each rainfall event, the abundant rainfall on Lihir Island guarantees the frequency of rainwater infiltration events, which, over a long term, may have provided significant amounts of oxygen. In addition, frequent rainwater infiltration may cause internal flow channels inside the stockpile which may facilitate air exchange and oxygen resupply. However, these mechanisms for additional oxygen resupply were not included in the current version of the model due to a lack of data records and limited model capacity. A quick and simple way to consider the enhanced oxygen resupply by these mechanisms is to set a low background oxygen concentration inside the stockpile. Considering all these issues, another simulation was run with a set background value of 0.5 mol·m^{-3} imposed for oxygen concentration and with boundary values changed to 0.5 and 2 mol·m^{-3} respectively for the bottom and surface of the stockpile.

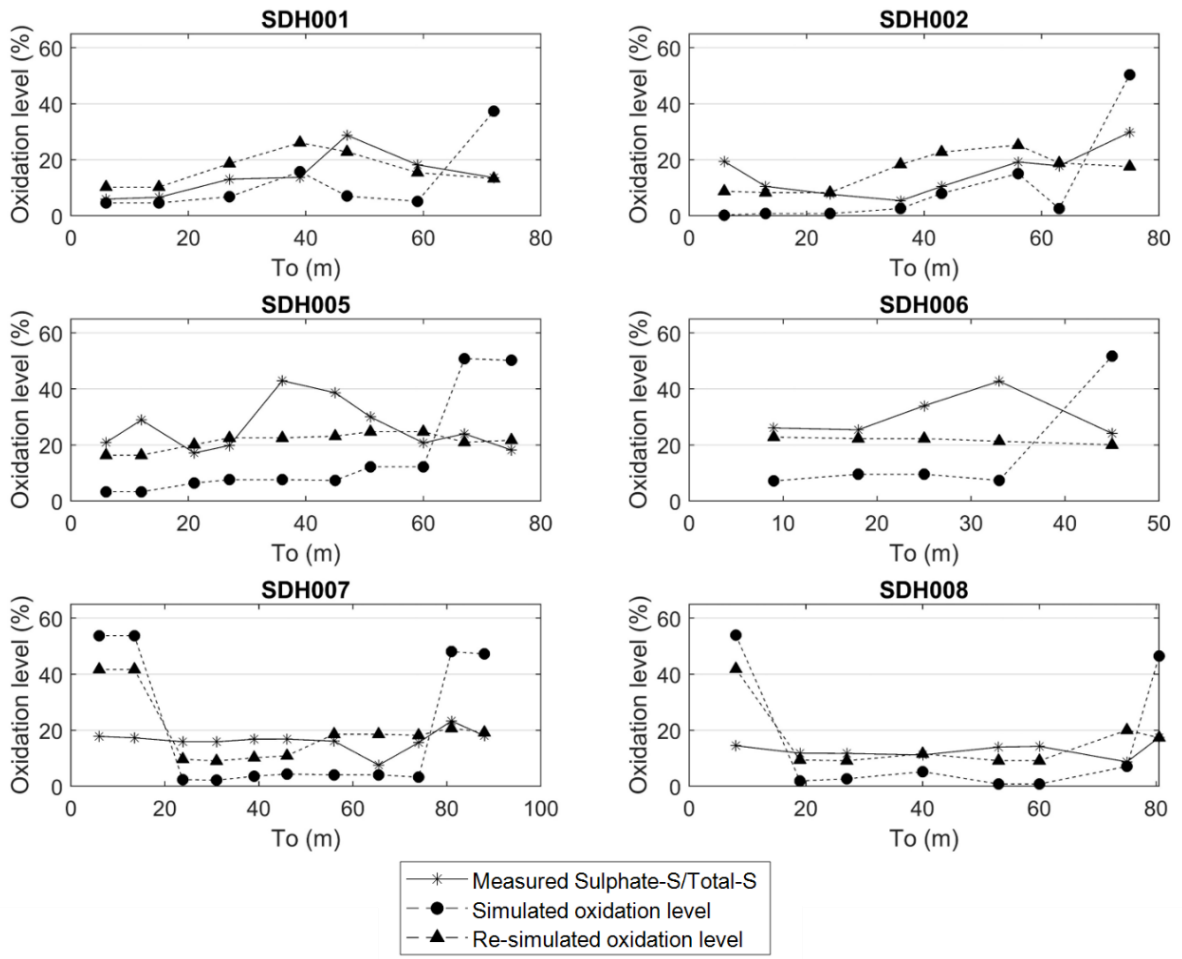

Fig. 4-9: Comparison of the simulated oxidation level and the measured ratio of Sulphate-S/Total-S at the sample locations

The re-simulated oxidation levels at sample locations are also plotted in Fig. 4-9 and show that, after adjusting the oxygen concentration, the simulation results are, on average, closer to the test results. Two further observations can be made. Firstly, the model input does not, and cannot, completely represent all the in-situ conditions. Secondly, the ratio of the sample sulphate-S to the total-S does not necessarily represent the true oxidation level as some sulphate content may have been present prior to the material being mined. From the mineralogical analysis of fresh material, it is known that there are sulphates present within the in-situ deposit, predominantly anhydrite within porphyry material, but they can also be present in small amounts in both epithermal and argillic materials. Given these two considerations, the re-simulated result can be accepted as a reasonable estimation of the stockpile oxidation. In the following discussions, the simulation results refer to those from the model with oxygen concentration adjustments.

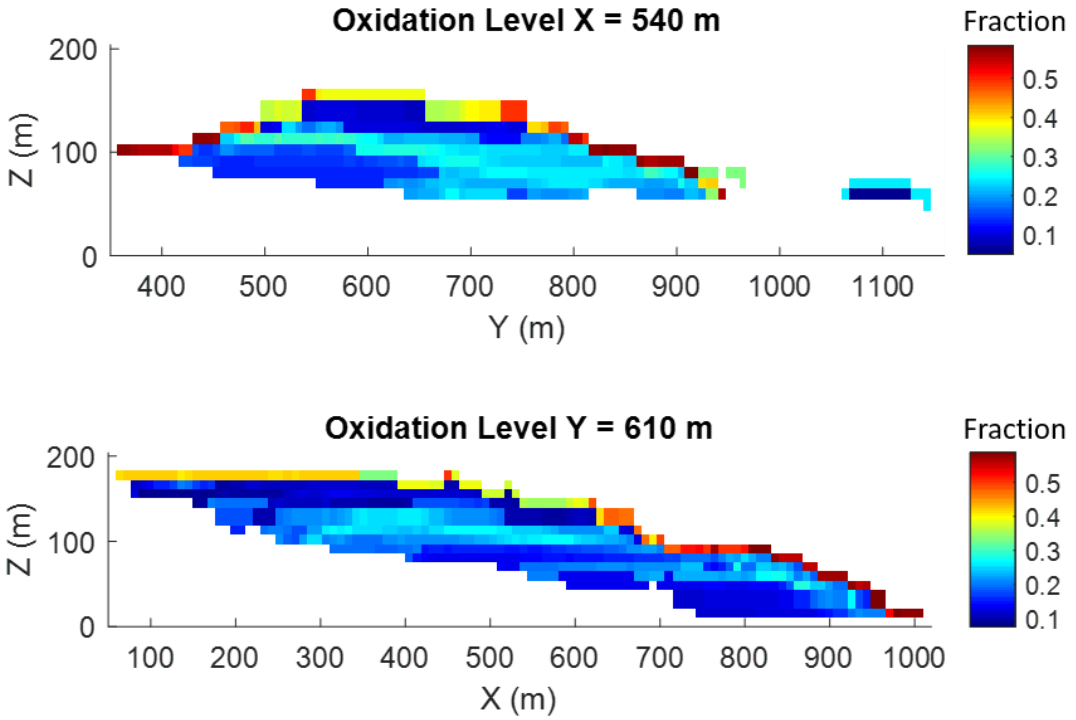

Fig. 4-10: Simulated oxidation levels for the Kapit Flat stockpile with adjusted oxygen concentrations

Fig. 4-10 shows the updated cross-sections of the oxidation level after adjusting the oxygen concentration. The average oxidation level of the stockpile is 25.4% and the highest value is 64%. Fig. 4-11 shows the histograms of the oxidation level for blocks of different types of materials. The average oxidation level for epithermal blocks is the highest of the three (29%) followed by porphyry blocks (22%) and argillic blocks (21%). This order appears to be consistent with the pyrite reactivities of the three materials listed in Table 4-3. Overall, for this case study, the oxidation level of a block is affected mostly by the accessibility to oxygen followed by the material properties.

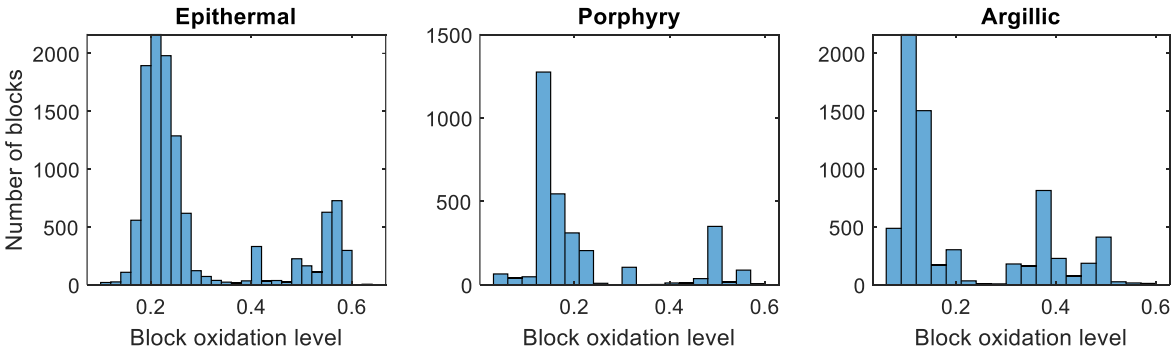

Fig. 4-11: Histograms of the oxidation levels for different types of materials

4.3.2 Estimation of gold recovery via direct cyanide leaching

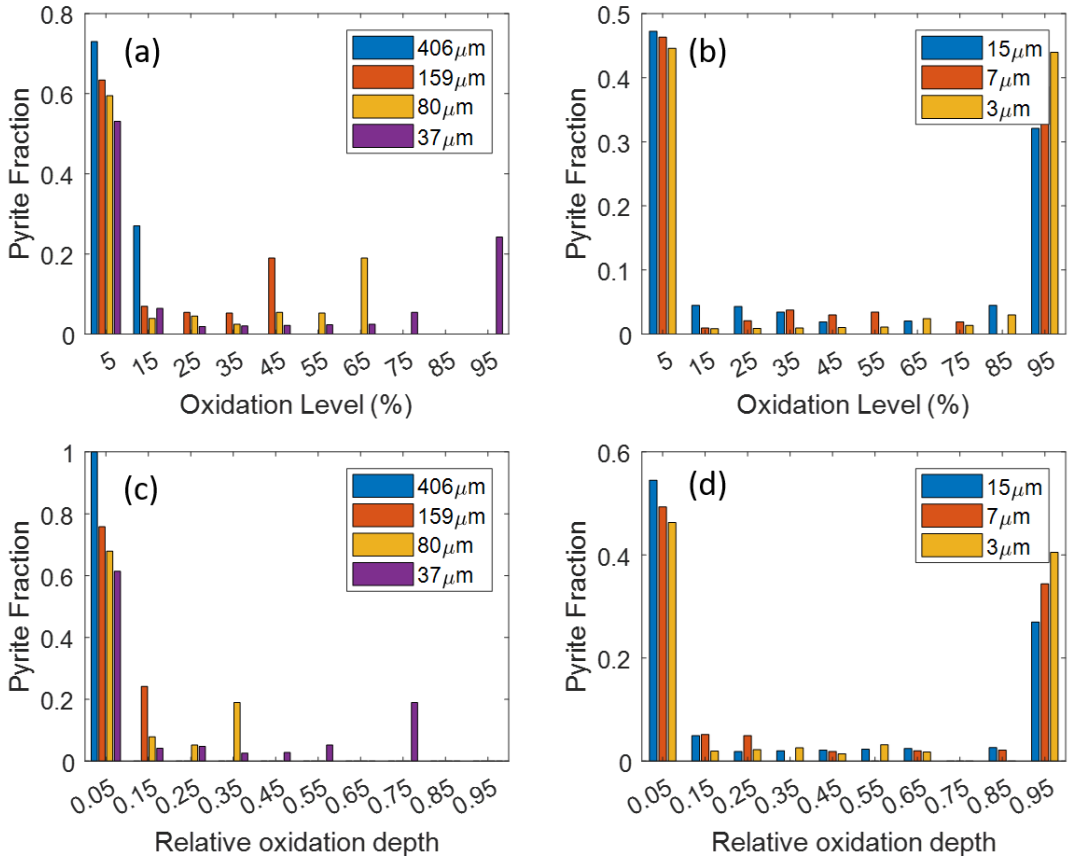

Fig. 4-12: Distributions of oxidation level and relative oxidation depth for pyrite grains of different sizes in a block; the overall oxidation level of this block is 21%

For the estimation of gold recovery via direct cyanide leaching, the relative oxidation depth of pyrite grains of different sizes is calculated from the simulated results ($r_c(i)$ in Eqs. (3-7) and (3-8)). As an example, Fig. 4-12 shows the oxidation profiles of the pyrite grains in a block where the oxidation level is 21%. More than half of the pyrite grains of size greater than 37 µm are no more than 5% oxidised (Fig. 4-12a), which corresponds to a very thin oxidised layer (thickness less than 5% of the particle radius) on the grain surface (Fig. 4-12c). As the pyrite

grain size becomes smaller, more pyrite grains are oxidised at a higher level (Fig. 4-12b). About half of the pyrite grains of size 3 µm are almost completely oxidised and most of the remaining pyrite grains are less than 5% oxidised, with the remainder having oxidation levels between these two extremes. Similarly, other small grain sizes (7 and 15 µm) are either almost completely oxidised or have little or no oxidation and only a very small fraction have oxidation levels between the two extremes.

The oxidation profiles of pyrite grains vary across the stockpile. The profiles vary with the block oxidation level as well as the material type because properties such as rock porosity, rock particle size distribution and pyrite grain size distribution differ for different types of material. As a result, each block has a unique oxidation profile. With this information over the stockpile together with the distribution of gold in pyrite grains, it is possible to evaluate the readily recoverable gold by direct cyanide leaching.

Mineralogical analysis of the Lihir orebody found that a significant proportion of pyrite grains contain less than 1 ppm of gold. This type of pyrite is classified as “no value” pyrite. The average proportion of “no value” pyrite differs for different types of materials, which on average is 24% for porphyry pyrite, 32% for epithermal pyrite and 60% for argillic pyrite. Analyses of samples from the Lihir orebody using LA-ICP-MS (Laser Ablation Inductively Coupled Plasma Mass Spectrometry) also showed different patterns of gold distribution in pyrite grains for different materials. One is an aggregation pattern where gold particles occur in several patches distributed either at the edge, or in the core, of the pyrite grain. Another is a uniform pattern where gold particles are evenly distributed within pyrite grains. The third and fourth types are those where gold particles are mainly distributed in the rims at or near the edge of pyrite grains surrounding barren or variable grade cores. The fifth type is bladed where high-grade gold content occurs on only one side of a pyrite grain. These gold distributions in pyrite grains indicate that a complete oxidation of pyrite may not be necessary for full recovery of the contained refractory gold. In other words, a high gold recovery may be achieved with only partial oxidation of pyrite. This can be seen in the sample test results for gold recovery via direct cyanide leaching shown in Fig. 4-5, which indicates that, in general, gold extraction via direct cyanidation increases as the pyrite oxidation level increases and the gold extraction percentage is always higher than the pyrite oxidation level.

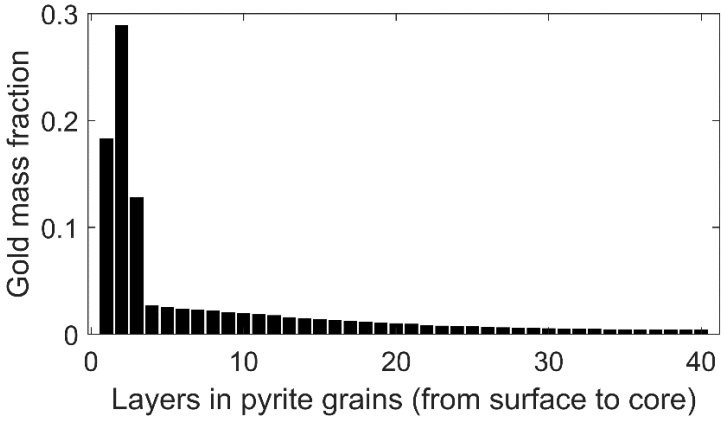

Fig. 4-13: Modelled gold distribution (by mass) in pyrite grains

Considering a mixture of all five gold distribution patterns mentioned above with slightly more rim patterns (the third and fourth types) than the others, an average gold distribution in pyrite grains can be estimated and the result is shown in Fig. 4-13. This indicates that, for a pyrite grain of any size, the gold content is most abundant in the first three outer layers of the discretised 40 layers and it decreases towards the inner part of the pyrite grain.

With the estimated gold distribution in pyrite grains, the cyanide-available gold recovery can then be estimated from the simulated oxidation profile for each block. Here it is assumed that the proportions of the gold content (mass fraction) contained in pyrites of different sizes are 0.05, 0.05, 0.1, 0.2, 0.2, 0.2, 0.2 respectively (in order of decreasing pyrite grain size). The estimated cyanide-available gold recovery for blocks at the same oxidation level as the samples is shown in Fig. 4-14 together with the measured cyanide gold recoveries for the samples tested. Fig. 4-15 shows the statistics of the estimated cyanide-available gold recovery for all blocks in the stockpile together with the sample test results for comparison. These comparisons show that the mean of the estimated gold recovery via direct cyanide leaching is very close to the mean of the measured cyanide gold recovery at comparable oxidation levels. However, the measured cyanide gold recovery for samples at similar oxidation levels has a much wider range of variability than that of the estimated values, especially for oxidation levels less than 30%. This indicates that the gold distribution in pyrite grains may vary much more significantly than that used in the model. When gold is more abundant at the edges of pyrite grains, a higher gold recovery can be achieved via direct cyanide leaching at a relatively low oxidation level. When gold is more abundant in the inner part of the pyrite grains, a lower cyanide-available gold recovery can be expected. In Fig. 4-15, the estimated cyanide gold recovery for oxidation levels from 50% to 70% continues to increase but there is a lack of test data for comparison. In addition, since the highest oxidation level from the simulation result is 71%, there are no estimated values for gold recovery at higher oxidation levels.

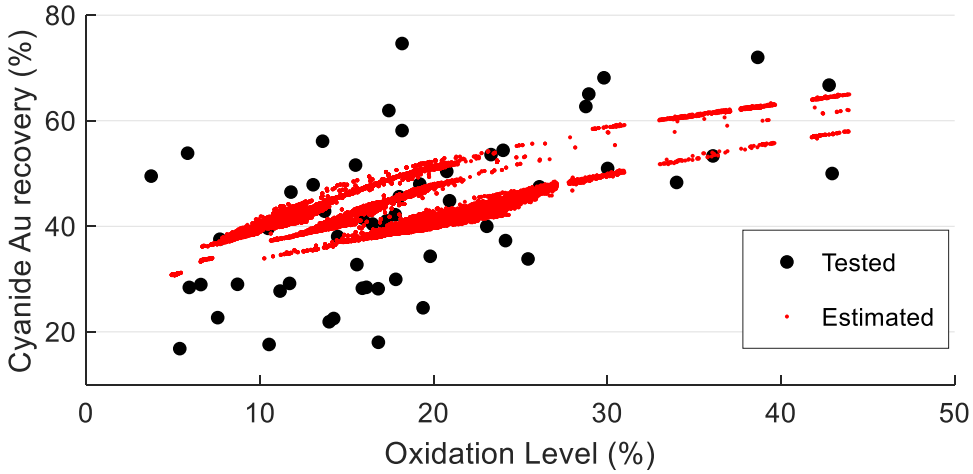

Fig. 4-14: Comparison of the cyanide-available gold recovery measured from test samples and that estimated from the model for blocks at oxidation levels comparable to the samples

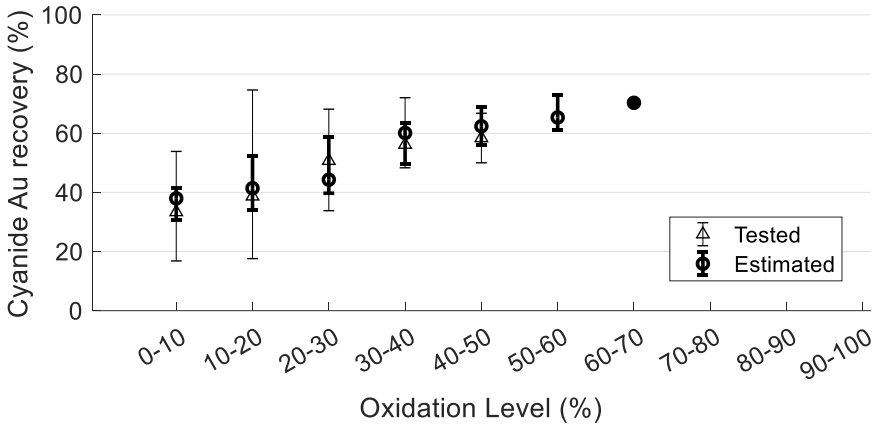

Fig. 4-15: The mean value and the range of variability in cyanide-available gold recovery for all blocks in the stockpile for different ranges of oxidation levels compared with those from the sample test results

Overall, the relationship between gold recovery via direct cyanide leaching and the pyrite oxidation level can be estimated from the oxidation profile, the gold fraction in pyrites of different grain sizes and the gold distribution patterns in the pyrite grains. While the oxidation profile can be simulated from the pyrite oxidation model presented in this paper, a reliable understanding of the other two variables can only be achieved through extensive laboratory analyses of samples, which are both expensive and time-consuming. An alternative approach is to use assumed values initially and derive acceptable estimates by calibrating the model for estimating gold recovery via direct cyanide leaching using the measured gold recovery values obtained from test samples, as has been done in this paper.

4.4 Conclusions

This paper presents a case study on modelling the natural oxidation of pyrite in a refractory gold ore stockpile at the Lihir mine in Papua New Guinea for the purpose of estimating the potential gold recovery via direct cyanide leaching without pre-treatment. The pyrite oxidation model simulates natural processes including the oxidation of pyrite in rock particles, heat transfer, heat-induced air convection and oxygen transport over the refractory gold ore stockpile. The site characteristics incorporated in the Kapit Flat stockpile model include geothermal heat, the degree of water saturation and the properties of three types of material: rock porosity, rock particle size distribution, pyrite grain size distribution, pyrite reactivity enhanced by arsenic content and the acid neutralisation capacity. The simulation results show that for a large stockpile of this size, the key factor that mostly affects the oxidation level is the accessibility to oxygen. Hence, the time that the material is exposed to the atmosphere during the construction of the stockpile is an important input to the model. A comparison of the simulation and test results shows that the oxidation level in the stockpile is underestimated by assuming diffusion and/or heat-induced air convection as the dominant mechanism(s) for oxygen transport in the model. This suggests that there are other mechanisms, such as air convection induced by wind, fluctuations in barometric pressure and rainwater infiltration, that play important roles in oxygen resupply in the stockpile. To accommodate this additional oxygen resupply, a background oxygen concentration is added

to the model as a simple approach. The updated oxidation level after this adjustment is comparable with the test results at the sample locations. This indicates that if there are multiple mechanisms for oxygen resupply that can provide sufficient oxygen for continuous pyrite oxidation, then an adjusted oxygen concentration calibrated by the test results may be a simple and practical alternative approach when the model capability is limited in simulating various mechanisms of oxygen transport over the stockpile.

In the case study, in addition to the oxidation level, the oxidation profile of each block is also simulated, which yields the fractions of pyrite grains that are oxidised to different relative oxidation depths. Gold recovery via direct cyanide leaching can then be estimated for each block using the simulated oxidation profile, together with the gold distribution patterns in pyrite grains and the gold fractions in pyrite of different sizes. If data are not available for the latter two variables, they can be back-estimated by trial-and-error calibration between the estimated and measured cyanide gold recovery at comparable oxidation levels.

This case study demonstrates a modelling approach to estimating the natural oxidation of pyrite in refractory gold ore stockpiles from which the potential gold recovery through direct cyanide leaching can be estimated. During the modelling process, assumptions were made for model inputs that were difficult to quantify or fully understand, which leads to uncertainties in the model. To reduce the model uncertainty, calibration with experimental results is necessary in order to better estimate and predict the pyrite oxidation level and the associated gold recovery from direct cyanide leaching for the stockpiled material.

Acknowledgement

This research was financially supported by Newcrest Mining Limited.

References

'Annual Mineral Resources and Ore Reserves Statement - as at 31 December 2019' 2020, Newcrest Mining Limited, viewed 27 October 2020,<https://www.newcrest.com/sites/default/files/2020-02/200213_Newcrest%20Resources%20and%20Reserves%20Statement.pdf>.

da Silva, JC, do Amaral Vargas, E & Sracek, O 2009, 'Modeling Multiphase Reactive Transport in a Waste Rock Pile with Convective Oxygen Supply', *Vadose Zone Journal*, vol. 8, no. 4, pp. 1038-1050.

Davis, GB & Ritchie, AIM 1986, 'A model of oxidation in pyritic mine wastes: part 1 equations and approximate solution', *Applied Mathematical Modelling*, vol. 10, no. 5, pp. 314-322.

Doyle, J, Wightman, E & Wood, M 2003, *QEM-SEM Mineralogy of Predictive ARD Column Material*, Rio Tinto Technical Services.

Elberling, B, Nicholson, RV & Scharer, JM 1994, 'A combined kinetic and diffusion model for pyrite oxidation in tailings: a change in controls with time', *Journal of Hydrology*, vol. 157, no. 1–4, pp. 47-60.

Gardner, K 2018a, 'Block model file of Kapit Flat stockpile ', Personal Communication, File Transfer, in H Wang (ed.).

Gardner, K 2018b, 'Oxidation model input for Kapit Flat stockpile', Personal Communication, File Transfer, in H Wang (ed.).

Gleeson, K, Butt, S, O'Callaghan, J & Jones, C 2020, *Lihir Operations Aniolam Island Papua New Guinea NI 43-101 Technical Report*, Newcrest Mining Limited.

Ketcham, VJ, O'Reilly, JF & Vardill, WD 1993, 'The lihir gold project; Process plant design', *Minerals Engineering*, vol. 6, pp. 1037-1065.

Lefebvre, R, Hockley, D, Smolensky, J & Gélinas, P 2001, 'Multiphase transfer processes in waste rock piles producing acid mine drainage: 1: Conceptual model and system characterization', *Journal of Contaminant Hydrology*, vol. 52, no. 1–4, 11//, pp. 137-164.

Lehner, S & Savage, K 2008, 'The effect of As, Co, and Ni impurities on pyrite oxidation kinetics: Batch and flow-through reactor experiments with synthetic pyrite', *Geochimica et Cosmochimica Acta*, vol. 72, no. 7, pp. 1788-1800.

Lehner, S, Savage, K, Ciobanu, M & Cliffel, DE 2007, 'The effect of As, Co, and Ni impurities on pyrite oxidation kinetics: An electrochemical study of synthetic pyrite', *Geochimica et Cosmochimica Acta*, vol. 71, no. 10, 5/15/, pp. 2491-2509.

León, EA, Rate, A, Hinz, C & Campbell, G 2004, 'Weathering of sulphide minerals at circum-neutral-pH in semi-arid/arid environments: Influence of water content', in *Proc., SuperSoil 2004: 3rd Australian New Zealand Soils Conf*.

Mayer, KU, Frind, EO & Blowes, DW 2002, 'Multicomponent reactive transport modeling in variably saturated porous media using a generalized formulation for kinetically controlled reactions', *Water Resources Research*, vol. 38, no. 9, pp. 13-11-13-21.

McKibben, MA & Barnes, HL 1986, 'Oxidation of pyrite in low temperature acidic solutions: Rate laws and surface textures', *Geochimica et Cosmochimica Acta*, vol. 50, no. 7, pp. 1509-1520.

Molson, JW, Fala, O, Aubertin, M & Bussière, B 2005, 'Numerical simulations of pyrite oxidation and acid mine drainage in unsaturated waste rock piles', *Journal of Contaminant Hydrology*, vol. 78, no. 4, pp. 343-371.

Nicholson, RV, Gillham, RW & Reardon, EJ 1988, 'Pyrite oxidation in carbonate-buffered solution: 1. Experimental kinetics', *Geochimica et Cosmochimica Acta*, vol. 52, no. 5, 1988/05/01, pp. 1077-1085.

Pabst, T, Molson, J, Aubertin, M & Bussière, B 2017, 'Reactive transport modelling of the hydro-geochemical behaviour of partially oxidized acid-generating mine tailings with a monolayer cover', *Applied Geochemistry*, vol. 78, 2017/03/01/, pp. 219-233.

Peng, S, Hu, Q & Hamamoto, S 2012, 'Diffusivity of rocks: Gas diffusion measurements and correlation to porosity and pore size distribution', *Water Resources Research*, vol. 48, no. 2, pp. n/a-n/a.

Walter, A, Frind, E, Blowes, D, Ptacek, C & Molson, J 1994, 'Modeling of multicomponent reactive transport in groundwater: 1. model development and evaluation', *Water Resources Research*, vol. 30, no. 11, pp. 3137-3148.

Wang, H, Dowd, PA & Xu, C 2019, 'A reaction rate model for pyrite oxidation considering the influence of water content and temperature', *Minerals Engineering*, vol. 134, 2019/04/01/, pp. 345-355.

Wang, H, Xu, C & Dowd, PA 2021, 'Modelling the pyrite oxidation level in a refractory gold-bearing stockpile to assess its potential for gold recovery by direct cyanide leaching ', Manuscript submitted for publication, School of Civil, Environmental and Mining Engineering, The University of Adelaide

Williamson, MA & Rimstidt, JD 1994, 'The kinetics and electrochemical rate-determining step of aqueous pyrite oxidation', *Geochimica et Cosmochimica Acta*, vol. 58, no. 24, pp. 5443-5454.

Wunderly, M, Blowes, D, Frind, E & Ptacek, C 1996, 'Sulfide mineral oxidation and subsequent reactive transport of oxidation products in mine tailings impoundments: A numerical model', *Water Resources Research*, vol. 32, no. 10, pp. 3173-3187.

Chapter 5

Thesis summary

5.1 Conclusions

This work addresses the research problem of evaluating pyrite oxidation in refractory gold-bearing stockpiles for the purpose of estimating the potential gold recovery without pre-treatment. To solve this problem, two models were developed in this work to describe pyrite oxidation at the small grain scale and at the bulk stockpile scale respectively. A real refractory gold ore stockpile was used as a case study.

The small scale model, a reaction rate model, describes the reaction rate of prolonged oxidation of pure pyrite grains for cases where diffusion barriers such as an oxidised layer and/or a thin solution film develops on fresh pyrite surfaces, a situation corresponding to pyrite oxidation in unsaturated water conditions and/or a circum-neutral to alkaline pH environment. This model considers both the surface reaction kinetics and the micro-scale transport of oxygen, and incorporates the effects of oxygen concentration, temperature and degree of water saturation on the oxidation rate of pyrite grains. The model parameters, including the diffusion coefficient, the surface reaction rate constant and the activation energy, were determined from the reaction rate data published in the literature.

The large scale model, a multi-component numerical modelling framework, can simulate the oxidation of pyrite in stockpiles together with related processes including oxygen transport and heat transfer that are interdependent with pyrite oxidation. This model incorporates the developed reaction rate model (in combination with the other reaction rate model for intro-aqueous, low pH conditions) as one of its components to simulate pyrite oxidation under different stockpile conditions. The simulation outputs from the multi-component model include oxygen concentration, temperature, oxidation level and the oxidation profile of pyrite grains over the stockpile, which are used subsequently to estimate the potential gold recovery through direct cyanide leaching. A synthetic stockpile was used to demonstrate the application of the proposed numerical modelling method and a comparison among different simulation scenarios was conducted to investigate the effects of stockpile properties such as porosity, diffusion coefficient and geothermal heat on the simulated oxidation level. It was found that the availability of oxygen is the most important limiting factor for pyrite oxidation and hence the properties that affect oxygen transport, such as porosity and diffusion coefficient, significantly influence the pyrite oxidation level.

Finally, the developed numerical modelling framework was applied to a real case study - the Kapit Flat stockpile on Lihir Island in Papua New Guinea. The oxidation level and oxidation profile of the pyrite grains over the Kapit Flat stockpile were simulated using the actual stockpile characteristics. It was found that for rocks at different locations in the stockpile, the histories of the exposure of the rocks to the atmosphere dominantly determine the oxidation level based on the influencing factors considered. The numerical model was calibrated with the measured oxidation level for samples taken from the stockpile. The comparison between the model outputs and the measurements revealed that there was oxygen resupply in addition to the modelled diffusion and heat-induced convection, which was most likely the result of frequent rainwater infiltration. A background oxygen level was added to the numerical model based on the calibration results to account for the effects of this additional

oxygen resupply. The simulated oxidation level based on the calibrated model is in general agreement with the measured results for the Kapit Flat stockpile. For the case study, an example was also given to illustrate the estimation of potential gold recovery through direct cyanide leaching from the estimated oxidation profile of pyrite grains at different locations in the stockpile.

5.2 Limitations

The model developed in this work describes the pyrite oxidation process in stockpiles/rock piles. There are three main limitations on the proposed approach. The first is related to confining the influencing factors for pyrite oxidation to an abiotic environment in this model. Although microbial activities are believed not to have significant effects on the long-term oxidation rate when oxygen is limited, omitting microbial activities restricts the use of the model to simulating pyrite oxidation with bacteria catalysis when sufficient oxygen is supplied. The second limitation is that, because of the simplification used to simulate the pH variations, the simulation of fluid flow and intro-aqueous equilibriums are not currently incorporated in the model. This may have some impact on the pyrite oxidation simulation results as the pH value determines whether a model, with or without the coating, should be used. In addition, the lack of capability for fluid flow simulation also limits the incorporation of the possible mechanism for oxygen resupply through rainwater infiltration, which might be an important process for the prediction of the level of pyrite oxidation, as shown in the Kapit Flat stockpile case study. Although the effect of this process can be included by using a simplified approach, as demonstrated, by adding a calibrated background oxygen level, the missing capability still limits the applicability of the model to cases where the rainwater infiltration is highly heterogeneous.

For the simulation of the pyrite oxidation in the Kapit Flat stockpile, although this work endeavours to incorporate as many of the stockpile characteristics as possible, not all relevant information was available for this research. Consequently, some input parameters were estimated instead of measured, and assumptions for these estimations were made. This leads to uncertainties in the modelling outcomes.

5.3 Future work

This work provides a numerical modelling framework for the evaluation of pyrite oxidation in refractory gold-bearing stockpiles. The model incorporates the effects of oxygen concentration, temperature, degree of water saturation and pH values on the oxidation rate of pyrite grains. Rock properties including porosity, diffusion coefficient and rock particle size distributions are considered. Other stockpile properties including geothermal heat, bulk porosity, diffusion coefficient, degree of water saturation and material stockpiling sequence are also incorporated into the model. This model can be further improved by incorporating the influence of microbial activity to include the ability to simulate bacteria-catalysed pyrite oxidation with sufficient oxygen supply. The simulation of pH variations can also be improved and oxygen resupply through rainwater infiltration can be incorporated by adding model components to enable the simulation of fluid flow and intro-aqueous equilibriums. This

increased capability would allow more relevant conditions, especially for possible oxygen resupply through rainwater infiltration, to be considered for pyrite oxidation and hence would improve the reliability and accuracy of the simulation results. For the Kapit Flat stockpile case study, further work, such as monitoring of oxygen concentrations at different locations inside the stockpile, would add valuable information for the validation of the developed model.

The estimation of the level of pyrite oxidation is the first step in estimating the potential gold recovery of the stockpile by direct cyanide leaching. In addition to the modelled oxidation profiles of pyrite grains, the estimation of gold recovery by direct cyanide leaching requires additional information, including the gold distribution in pyrite grains and the fraction of gold contained in pyrite of different sizes. Currently only simplified distributions are assumed in the model and future work to quantify gold distributions in pyrite grains would be beneficial.